Horn, Michael R.; Singh, Amandeep; Alomari, Suaad; [et al.]. «Polyoxometalates (POMs) : from electroactive clusters to energy materials». Energy & environmental science, Vol. 14, issue 4 (April 2021), p. 1652-1700. DOI 10.1039/d0ee03407j

Polyoxometalates (POMs): from Electroactive Clusters to Energy Materials

View Article Online
DOI: 10.1039/D0EE03407J

Michael Horn[1], *Amandeep Singh*[1], *Suaad Alomari*[1], *Sara Goberna-Ferrón*[2], *Raúl Benages-Vilau*[2], *Nilesh Chodankar*[3], *Nunzio Motta*[1, 4], *Ken (Kostya) Ostrikov*[1, 4], *Jennifer MacLeod*[1, 4], *Prashant Sonar*[1, 4], *Pedro Gomez-Romero*[2]*, *Deepak Dubal*[1,4]*

[1]School of Chemistry and Physics, Queensland University of Technology (QUT), 2 George Street, Brisbane, 4000 Queensland, Australia.

[2]Catalan Institute of Nanoscience and Nanotechnology, ICN2 (CSIC-BIST) Campus UAB, E-08193 Bellaterra (Barcelona), Spain

[3]School of Chemical Engineering, Chonnam National University, Gwangju 500–757, South Korea

[4]Centre for Materials Science, Queensland University of Technology (QUT), 2 George Street, Brisbane, 4000 Queensland, Australia.

Abstract

View Article Online
DOI: 10.1039/D0EE03407J

Polyoxometalates (POMs) represent a class of nanomaterials, which hold enormous promise for a range of energy-related applications. Their promise is owing to their “special” structure that gives POMs a truly unique ability to control redox reactions in energy conversion and storage. One such amazing capability is their large number of redox active sites that arises from the complex three-dimensional cluster of metal-oxide ions linked together by oxygen atoms. Here, a critical review on how POMs emerged from being molecular clusters for fundamental studies, to next-generation materials for energy applications is provided. We highlight how exploiting the versatility and activity of these molecules can lead to improved performance in energy devices such as supercapacitors and batteries, and in energy catalyst applications. The potential of POMs across numerous fields is systematically outlined by investigating structure-property-performance relationships and the determinant factors for energy systems. Finally, the challenges and opportunities for this class of materials with respect to addressing our pressing energy-related concerns are identified.

View Article Online
DOI: 10.1039/D0EE03407J

Broader context

Unprecedented global energy demand and climate change have spawned broad based efforts to develop new sustainable clean energy conversion and storage technologies. A range of electrochemical energy systems have the potential to address critical energy demands, however, their performance is far from the expectations. To this end, particular emphasis has been given to the design and engineering of new functional materials. Polyoxometalates (POMs), a class of metal oxide cluster anions with the ability to reversibly transfer multi-electrons have recently broken through as functional materials. POMs exhibit unique chemical properties unlike those of general metal complexes with various ligands. The open frameworks with independent structural units and rich-redox chemistry makes them ideal materials for cutting-edge energy-related technologies. Here, we provide critical analysis of the current knowledge on the impact of structure and properties of POMs for improved performance in energy devices. We believe that this review will not only provide the fundamental knowledge in the field of POMs-for-Energy but will also help to address the current challenges in electrification to decarbonize industry and society.

1. Introduction

View Article Online
DOI: 10.1039/D0EE03407J

Many countries around the world have set targets to limit anthropogenic climate change and with this comes an effort to reduce emissions that are the product of fossil fuel combustion.[1] This is driving a shift towards electrified transport systems, with urgent demand for improved energy storage; but these systems are only as clean as the source of the electricity they consume. Therefore, the transition towards energy *production* via renewable sources *as well as* efficient *storage*, are two inseparable parts of the net equation. Another trend seen in recent years is the rapid increase in portable electronics and electric devices for uses including communications, computing, sensing, entertainment, construction, and general maintenance.[1-4] A link between this trend climate change mitigation, is a very high demand for research and development of innovative electrical energy conversion and storage.

A wide range of energy conversion and storage technologies are being researched intensely. Various battery chemistries include lithium and sodium, and redox-flow.[2-4] Other modes of conversion and storage include supercapacitors, hybrid battery-supercapacitors, fuel cells, hydrogen-based systems and a wide range of photovoltaics.[5-10] The development of the next generation of all these modes requires materials that can be understood and controlled at the nanoscale, but also applied on the scale of industrial manufacturing processes.

Polyoxometalates (POMs) are an exceptional group of inorganic redox active materials that consist of multiple metal-oxide ions linked together by oxygen atoms to form nanoclusters within an ordered three-dimensional framework. Their size allows them to be viewed as a type of oxide quantum dots,[11,12] possessing a very high surface to bulk ratio. Their rapid and highly reversible redox activity endows them with excellent electrochemical properties. This underpins the motivation for an increasing amount of research into POMs for energy materials and other related applications.

POMs have a history dating back to the late 1700s when heteropoly acids were first discovered. From the early 1800s their complex structure was the subject of theorizing.[13] It was not until 1934 when J. F. Keggin used x-ray diffraction to interpret the structure of 12-phosphotungstic

View Article Online
DOI: 10.1039/D0EE03407J

acid,[13] that some level of agreement about structure started to be reached. The general chemical form of the class of POMs to which 12-phosphotungstic acid belongs can be written $XM_{12}O_{40}$, where X denotes a heteroatom and M a transition metal addenda atom. This form is named after its discoverer and is referred to as the Keggin structure. It remains one of the most widely investigated and understood structural forms of POMs.

Part of the attraction to these metal oxide clusters relates to their broad range of possible redox states and valences, while the molecular cluster itself may experience very little change in its physical structure. For example, stable crystal forms of ionic POM compounds can be synthesized that possess the same stoichiometry in the POM anion, but the anion may carry a different charge. The salt $K_6[Co^{II}W_{12}O_{40}].nH_2O$ forms green prismatic crystals. The Keggin POM anion in the compound carries a molecular charge of -6e (that is $[Co^{II}W_{12}O_{40}]^{-6}$). Under careful synthesis conditions, Casañ-Pastor et al. produced a novel potassium salt of the POM anion $[Co^{II}W_{12}O_{40}]^{-8}$.[14] A solid crystalline product of the salt possessed a deep blue color. The authors describe how the extra two “blue electrons” hop between the (tungsten) metal atoms at the center of each tetrahedra that make up the cluster (see Figure 1 for a visualization of the tetrahedra forming a POM cluster). However, they also emphasize that molecular orbitals involving oxygen atoms play an important role in electron delocalization. Yet, despite the changes in valency, the bond lengths between the addenda atoms and other metal-oxygen bonds in the POM cluster change only on the order of a few percent of an Angstrom, and the cluster maintains a specific α type of Keggin structure (see Figure 1), that actually becomes more rigid. These features hint at the capability of POMs to act as stable and versatile molecular reservoirs for charge carriers.

The Keggin structure was the first stable complex form of POM to be characterized, but many other framework forms have been discovered since.[5] The structural motifs can be broadly classified into two types, isopolyoxometalates (isopolyanions) and heteropolyoxometalates (heteropolyanions). The former case possesses all the metal atoms are of the same element, where the addenda metal atoms are accompanied by heteroatoms, which may be either metal or non-metal. Common

View Article Online
DOI: 10.1039/D0EE03407J

heteroatoms include W, Mo, V, C or Si, P, and As, whereas common addenda metals include Mo and W.[15] The general formation reaction of POMs can be written as

$$xMO_4^{2-} + 2yH^+ \Delta\Leftrightarrow M_xO_{4x-y}^{(2x-m)-} + yH_2O$$

where MO_4^{2-} is an oxyanion, and $M_xO_{4x-y}^{(2x-m)-}$ is an isopolyanion. In contrast to the formation of isopolyanions, if the condensation reaction of several (x) oxyanions occurs around (s) central heteroatoms the reaction leads to the formation of heteropolyanions with the general formula $X_s M_x O_y^{z-}$. Various kinetically driven structures can be formed with the number of metal atoms and heteroatoms having different X/M ratios. Knowledge of isopolyoxometalates is mostly derived from the Lindqvist ($[Mo_6O_{19}]^{2-}$), heptamolybdate ($[Mo_7O_{24}]^{6-}$) and decamolybdate anions.[15] A much greater number of heteropolyoxometalates have been characterized. Based on their X/M ratio two fundamental types of hetero-POM structures are the Keggin (X/M $=\frac{1}{12}$) and Dawson (X/M $=\frac{2}{18}$) structures,[1][16] as shown in Figure 1. However many more have been identified such as the Dexter-Silverton structure ($[XM_{12}O_{42}]^{n-}$),[17] and the much larger Keplerate cluster (Mo_{132}-based).[18] Furthermore, isomeric variations to the basic structures exist; for example, the Keggin structure has five recognized isomeric variations (denoted α through to ε – see Figure 1). The wide range of structural forms, with various properties and tunability has prompted researchers to present libraries of known POMs as building blocks for nanomaterials.[19,20] In addition to the synthesis and structural studies of larger and more intricate forms of these interesting nanoparticles (NPs), facile synthesis methods are sought which avoid the need for separation and purification of intermediate products.[18] Thus, extensive work has gone into the optimization of POM synthesis routes, to improve the yield of specific moieties as well as minimizing time and cost.[21] For a comprehensive and recent review of POM structures and synthesis, the reader is referred to the work of Gumerova et al.[15]

Herein, we have presented a brief history and discussion around the classification and properties of POM materials with primary focus on the energy-related applications (Figure 2). Specifically, we focus on the properties of heteropolyoxometalates and recent progress towards their

View Article Online
DOI: 10.1039/D0EE03407J

applications in supercapacitors (SCs), batteries and various catalytic applications. Firstly, the review highlights (section 2), the key advances in the enhancements of electrochemical supercapacitive properties by introducing POMs as redox active moieties that offers large numbers of electrons during the oxidation/reduction processes. The challenges of anchoring POMs to other hybridizing materials are presented with other interesting properties and theoretical insights to be used in energy-devices. Section 3 carries this subject matter forward into battery applications where POMs have been much more widely explored. Several battery chemistries such as lithium ion, sodium ion and redox flow systems are briefly discussed. The lithium ion chemistry is given greatest attention based on its popularity for research and the resulting depth of literature. This allows the article to present the major breakthroughs in stable attachment of POMs to conductive or chemically active electrode components, the use of POMs as precursors to other high surface area active materials, and POM hybrid materials for batteries. The following section goes into discussion of the science and engineering of POMs for catalysis applications (section 4). Research on POM-based catalysts has greatly increased in the last few years. Among the research fields, chemical oxygen reactions, such as for oxygen evolution (in electrolyzers) and for oxygen reduction (in fuel cells) represent a bottleneck for the development of energy conversion technologies. The section also includes a discussion on the progress of POM-based materials in different catalytic reactions such as carbon dioxide (CO_2) reduction, nitrogen (N_2) reduction and biomass conversion. Each section presents perspectives on the different roles for POMs in energy, including those which are expected to stimulate new research directions. The final section summarizes key points and conclusions as well as a short commentary on future challenges and the outlook for POMs.

2. POM-based Materials for Supercapacitors

Traditional supercapacitors (SCs) store charge via the electric double layer effect (EDL). In these devices, high surface area materials are exploited to store charge via the electrophysical separation over very small distances at an electrode-electrolyte interface. Relative to current battery

View Article Online
DOI: 10.1039/D0EE03407J

chemistries, these devices are able to deliver very high power densities but they suffer from low energy density.[22] Over the last decade, a widely investigated challenge has been to increase the amount of energy that can be stored in supercapacitors, while not trading off too heavily against their high power capability and exceptionally long cycle life. The theoretical capacitance of graphene sets somewhat of a benchmark for this work, at 550 $F.g^{-1}$. The basis for this as a benchmark is rationalized by virtue of it representing a 100% exploited atomically thin surface, for the formation of an EDL.

In practice, research on purely EDL capacitive materials has achieved around as high as 200-300 $F.g^{-1}$.[23] However, aside from pursuing of the goal of maximal surface usage, a popular means of improving energy density is via pseudocapacitance (Note that the term pseudocapacitance represents the extrinsic pseudocapacitive behavior), where chemically active species undergo fast reversible redox reactions close to the surface of electrode materials.[24] POMs are great contender materials for such purpose, given their high surface-to-bulk ratio, and the numerous available redox states of the addenda metal species, which enable multi-electron charge transfer per molecule. However, there are major issues that remain to be addressed and comparison can be difficult given the wide variable space and range of metrics available for expressing results. Two of the greatest challenges for POMs are securely anchoring POMs to a host material and achieving the very long-term cycling stability. This section will discuss some advances that have been made towards all the above challenges, in applying POMs in SCs.

The idea of exploiting the multiple redox states of POMs for enhancing the energy density of SCs with near-surface confined redox reactions has been known for more than two decades. As far back as 1997, POMs were being combined with conducting polymers such as polypyrrole (PPY),[25] polyaniline (PANI) [26,27] and poly(3,4-ethylenedioxythiophene) (PEDOT).[28] These materials were presented as organic-inorganic “hybrids”, and the focus was on their use in SCs. This work has continued in recent years, suggesting that there is much that remains to be explored and to be better understood.[29] In 2012, Gomez-Romero’s group conducted one of the earlier reported studies where a PMo_{12}-type POM was anchored to a simple activated carbon (AC) to create a hybrid material. The

View Article Online
DOI: 10.1039/D0EE03407J

hybrid exhibited significantly enhanced performance over bare AC as large current under the CV curves can be seen in Figure 3 (a).[28] Phosphomolybdic acid ($H_3PMo_{12}O_{40}$) was used to decorate the AC, increasing its mass by 54%. The *cell capacitance* of the hybrid was improved by an average 27% over a range of current densities up to 3 $A.g^{-1}$ and it displayed strong cycling stability with 91% retention over 8,000 cycles. Although the cell was symmetric, with the same materials and mass loading for each electrode, the capacitance for positive and negative were different (160 $F.g^{-1}$ and 183 $F.g^{-1}$, respectively), suggesting that even greater performance can be achievable by refined cell construction and balancing (see Figure 3b). The authors compare their achievements to other work on POM-carbon nanotube-based hybrids,[30-32] citing improvements in every respect. Since then more work has reinforced that the energy density of microporous carbons can be improved by the hybridization with POM. The later work has added new knowledge about the connection to microporosity [33] and the ability of POM-based hybrids to enable high-voltage aqueous systems.[34]

Straightforward approaches to applying POMs have been shown to yield good results. Vanadate POMs have been used as a positive electrode with AC as the negative electrode in the construction of an asymmetric device.[35] They reported 354 $F.g^{-1}$ with 73 $Wh.kg^{-1}$ at 0.1 $A.g^{-1}$ and associated power of 312 $W.kg^{-1}$. As can be seen from the Ragone plot in Figure 3 (c), power could be increased to 6238 $W.kg^{-1}$ but this resulted in a reduction of energy density to 22 $Wh.kg^{-1}$. The capacitance retention was 70% after 1000 cycles. In this above report, the POM based electrode was formed by simple mechanical hand mixing of the materials with a binder and carbon black. In battery research, mechanical methods of mixing POMs, such as this hand mixing, or ball milling and other techniques, are frequently reported, and described in section 3. More commonly in SCs, various solution-based chemistry approaches are applied to anchor the POMs on conducting scaffold to use as an electrode.

Exotic emerging materials have also been used for anchoring POMs. For example, metallacalixarenes that are ordered crystalline materials similar to 2D metal organic frameworks (MOFs) with repeating nano-sized cup-shaped pockets in their surface (see Figure 3d).[36]

View Article Online
DOI: 10.1039/D0EE03407J

Silicomolybdate-based POMs have been used to form (POM)/metallacalixarene/graphene-based electrode materials. Two compounds were tested in a recent study, $[Ag_5(C_2H_2N_3)_6][H_5 \subset SiMo_{12}O_{40}]$ – compound 1, and $[Ag_5(C_2H_2N_3)_6][H_5SiW_{12}O_{40}]$ – compound 2, where ($C_2H_2N_3$ = 1*H*-1,2,4-triazole). Compound 1 performed best, with a reported capacitance of 230 $F.g^{-1}$ at 0.5 $A.g^{-1}$. The materials both retained around 78.5% of their capacitance after 1000 cycles at 10 $A.g^{-1}$. While it is difficult to account for all the variables, in a very casual comparison between the last two cited reports,[35,36] the metallacalixarene provided some benefit towards holding onto the POMs for longer cycle life of the as-formed electrode.

The above comparison highlights the most critical challenge faced in work where POMs are applied to SCs. That is, long term stability is highly linked to the ability to anchor POMs to a conductive framework that will exploit their redox capacity but maintain cyclability.[25] Progress is being made, as the metallacalixarene examples demonstrate by comparison to the AC-POM hybrid. However, when compared to commercial (AC based) supercapacitor products, where it is reasonable to see cycle ratings of over 1 million cycles with the same or greater than 75% capacitive retention and no power fade,[22] it can be seen that there is still significant improvement required. The following section discusses materials that are suitable for SC electrodes, which have been synthesized with POMs, to form POM-functionalized hybrids.

2.1 POM-Functionalized Hybrids

The key opportunity that POMs offer to enhance energy storage devices lies with their ultra-dispersed nature (all or most active centers are surface atoms) and with their ability to reversibly exchange large numbers of electrons. Up to +/- 24 e per molecule has been claimed in some cases.[37] However, such a degree of reduction is debated and is in conflict with other knowledge on POMs, which sets a more conservative limit for the number of electrons that can be exchanged reversibly.[38] As a pure material, POMs are generally electrically insulating. Therefore, exploiting the desirable qualities of POM complexes requires them to be supported on conductive pathways. In the context of SC electrodes, it is of particular importance to maintain a high surface area for double layer

View Article Online
DOI: 10.1039/D0EE03407J

capacitance and high power handling, as well as chemical stability for long cycle life.[39] The aim of combining high surface area, electrical conductivity and chemical stability has stimulated the creation of a wide range of hybrid materials. The definition of a hybrid material herein means a POM-based material that through a given synthesis procedure has been combined at a molecular level with some other material/s to achieve synergistic properties. This section describes the hybridization of POMs with conducting polymers and various forms of nanocarbons.

The motivation for this type of best-of-both-worlds chemical hybridization is enhancing EDL performance with the redox contribution of POMs. This contribution can be quite significant. For example, the use of a polymerized imidazolium linker (PIL) cation to secure $GeMo_{12}$ and $SiMo_{12}$ POMs to multi-walled carbon nanotubes (MWCNTs) has been shown to achieve an increase of more than nine times the capacitive performance relative to bare MWCNTs – 191 $F.cm^{-3}$.[40] In this study, a layer-by-layer (LbL) method of constructing the conducting polymer-carbon-POM composite was used and was compared to using a more conventional linker, poly(dimethyl diallyl ammonium chloride) (PDDA). The performance of the PIL is significant, because PDDA as a linking polymer has itself been shown to offer reasonable performance at high charge-discharge current densities, which is synonymous with high CV scan rates. For example, PDDA-functionalized reduced graphene oxide (PDDA–rGO) was used as the conductive matrix to support $PMo_{12-x}W_xO_{40}^{3-}$ (PMoW),[41] and a capacitance of 140 $F.g^{-1}$ at 10 $A.g^{-1}$ was reported.

Polypyrrole nanopipes (Ppy-NPipes) are another type of purely polymeric conductive framework that have been enhanced for pseudocapacitance by doping with Keggin PW_{12} and PMo_{12} type POMs.[42] The two types of POM doped nanopipes showed elevated capacitive performance of almost 1.5 times that of the bare Ppy-NPipes with 294.1 $F.g^{-1}$ and 341 $F.g^{-1}$ for the molybdenum and tungsten POMs, respectively. By comparison, the bare Ppy-NPipe exhibited 204.5 $F.g^{-1}$. Symmetric devices using each type of POM-hybrid material exhibited high performance metrics; 6.3 and 6.8 F/cm^3 and 1.5 and 2.2 mWh/cm^3 for the molybdenum and tungsten variants, respectively.

View Article Online
DOI: 10.1039/D0EE03407J

Wide ranges of synthesis methods have been explored to produce POM hybrid electrode materials, and variations to the methods can produce interesting results. Polyaniline (PANI), one of the first discovered conducting polymers, has been combined with phosphorous, tungsten, and silicon based Keggin POMs to form molecular hybrids for supercapacitor applications.[26,27] In one of these studies, PMo_{12} was combined with PANI and directly deposited onto current collecting foils using electrochemical deposition techniques.[27] The materials were deposited by two methods. An electrochemical-only method of applying a potential sweep in H_2SO_4 electrolyte (ECh) was compared to a chemical-electrochemical method (Ch-ECh). In the latter, larger amounts of precursor phosphomolybdic acid and aniline were added to the H_2SO_4 solution before the same electrochemical cycling as the former. When tested using a solid-state H_3PO_4 based electrolyte membrane in a two-cell configuration, the results showed that the ECh method outperformed the Ch-ECh approach. SEM further supported this, where, surprisingly, a much higher density of POM-PANI clusters is visible on the ECh produced electrode.

In addition to affecting the yield of materials, variation to the reaction of precursors in POM production is known to result in different stoichiometries.[21] The Wells-Dawson 18-molybdo-2-phosphate POM, $K_6P_2Mo_{18}O_{62}\cdot{}_{12}H_2O$ (P_2Mo_{18}), has been combined with $Ru(bpy)_3C_{l2}.6H_2O$ ($Ru(bpy)_3$) to form a molecular hybrid.[43] The synthesis was performed both with and without the presence of potassium iodide (KI), and this resulted in different stoichiometry for the products. The different ratio of $Ru(bpy)_3$ to the linked P_2Mo_{18} molecules in turn affected the capacitance for the materials when studied for their use in neutral bio-compatible electrolyte systems. For the product formed in the presence of KI, 125 F g^{-1} was reported, versus 68 F g^{-1} for the hybrid formed without KI present. The excess of $Ru(bpy)_3$ in the KI-derived material suggests that the interesting electronic properties of this ligand play an important role in the transport of charges associated with the reduction and oxidation of the POMs.[44]

While the use of polymeric linkers and other ligands typically requires synthesis via carefully measured chemical reactions, simple mixing and solvo-thermal methods are facile, and therefore can

View Article Online
DOI: 10.1039/D0EE03407J

be easily adopted for other hybrid types. For example, POMs have been immobilized in Cu-based MOFs by multiple research groups, to create polyoxometalate/metal organic frameworks (POMOFs).[45,46] *See section 3.1.1.4 for more on POMOFs in lithium batteries*. Simple one-pot mixing is also a widely applied route to synthesizing POM-nanocarbon based hybrids. Dong et al. used a Mo_{132}-based Kepplerate POM combined with reduced graphene oxide (rGO) and tested its performance in an asymmetric cell using modified AC as the opposite electrode.[47] However, for carbon-based materials, the interaction with POMs is relatively weak.[48] Therefore, mixing methods commonly still seek some sort functionalization of either the POM or the carbon scaffold to improve the interaction strength, albeit in reactions less sensitive to the stoichiometry. In other recent work on Keplerate POMs, Pakulski et al.[48] synthesized hybrid supercapacitor electrode material by mixing electrochemically exfoliated graphene (EEG) nanosheets with Mo_{132} POM functionalized with dodecyltrimethylammonium bromide (DTAB), resulting in the formation of porous 3D superstructures. Performance in H_2SO_4 electrolyte revealed 65 F g^{-1}, 93 $mFcm^{-2}$ and 93 Fcm^{-3} respectively for the Mo_{132}-DTAB-EEG hybrid.

Cuentas-Gallegos et al.[31] fabricated novel hybrid materials using Keggin type POMs and functionalized CNTs. The importance of functionalizing the CNTs is described in some detail. It enables the POMs to more securely anchor to the carbon framework during the synthesis procedure of the electrodes. The report emphasizes again the importance of ensuring strong POM-to-scaffold interactions or linking for ensuring long-term cycle stability in such hybrid materials. In another work by the same author, $-NH_2$ and -OH functional groups were grafted onto vulcan carbon (VC) then the material was hybridized with phosphomolybdic acid ($H_3PMo_{12}O_{40}.{}_{12}H_2O$) to investigate its effects on capacitive performance. Functionalization and hybridization resulted in successive losses of the VC surface area. The authors propose that this is due to micropore blocking. However the -OH functionalized VC was found to improve the POM retention onto the carbon material and therefore showed better performance than other combinations studied.[49]

View Article Online
DOI: 10.1039/D0EE03407J

The graphene-based material rGO is an appealing nanocarbon for hybrid electrode materials.[50] The appeal stems from its hydrophilic nature and well-established commercial-scale production methods for its precursor, graphene oxide.[51,52] As well, intrinsic defects in the material after reduction offer functional sites for the attachment of polar molecules. While the functional groups of rGO have been well-exploited for attaching metal-oxides for enhanced pseudocapacitance,[53,54] research suggests that their ability to anchor POMs is less certain. In a comparative study exploring this point, phosphomolybdic acid ($H_3PMo_{12}O_{40}$) was coupled with rGO and compared with another hybrid where the grafting of $H_3PMo_{12}O_{40}$ onto rGO sheets is aided by poly(1-vinyl-3-ethylimidazolium bromide) ([VEIM][Br]).[55] TEM of the polymer ionic liquid (IL) aided hybrid (POM/PIL/rGO) reveals individually-anchored POMs with no clumping. A maximum capacitance value of 408 F g^{-1} was recorded for the POM/PIL/rGO material, at a constant current density of 0.5 A.g^{-1} in H_2SO_4 electrolyte. This was more than two-fold higher than that of the POM/rGO material with no polymeric linker, which displayed only 162 F.g^{-1}. The POM/PIL/rGO retained 92% of its initial capacitance while the current density was increased up to 10 A.g^{-1}. In contrast, the capacitance of the POM/rGO decreased more significantly as the constant current density was increased up to the same limit, down to a value of 110 F g^{-1}. In addition, the POM/PIL/rGO material retained 98% of its capacity after 2000 cycles at 10 A g^{-1}. In other recent and notable work utilizing POM-rGO hybrids with polymeric linking, Ensafi et al. made a sponge formulated as $[(n\text{-}C_4H_9)4N]5[PW_{11}CoO_{39}]$@IL-rGO. It was tested in seawater and in H_2SO_4 electrolyte. They report an impressive 834.3 F g^{-1} at a current density of 0.9 A.g^{-1} in seawater.[56] This result is promising with respect to both energy storage applications as well as capacitive deionization for water desalination.

As seen in a number of the above reports, the use of H_2SO_4 aqueous electrolyte is a popular choice for research level testing of materials and devices. In a comparative study centered on its use, $PW_{12}O_{40}$ was used to functionalize rGO, and the resulting phosphotungstate product was applied in symmetric devices. The devices were tested using 1M H_2SO_4 electrolyte and examined against the same 1M H_2SO_4 but with hydroquinone added for additional redox activity. The devices containing

View Article Online
DOI: 10.1039/D0EE03407J

the doped electrolyte exhibited an energy density of 2.38 Wh cm^{-3} as compared to the bare sulfuric acid system which achieved 1.05 Wh cm^{-3}.[57] This work and other similar works demonstrate the ability to boost the energy density by hybridizing the electrolyte system as well as the electrode materials.[39,57,58] The same authors as [57] use PW_{12} and PMo_{12} again to dope rGO.[59] The materials are tested individually in symmetric cells, and then in an asymmetric device where the rGO-PW_{12} hybrid is applied as the positive electrode and the rGO-MoW_{12} is used for the negative electrode. Careful study of the redox potentials for each hybrid via CV method in two–electrode configuration prior to the assembly of the asymmetric device enabled the use of 1M H_2SO_4 electrolyte in a potential window of 1.6 V, an extension of 0.3 V over the typical limit of aqueous systems.

Voltage windows have been extended even further using poly-vinyl-alcohol (PVA)/H_2SO_4-based gel electrolyte. A cobalt-containing Anderson-type POM was decorated on the surface of a reduced rGO aerogel via one-pot hydrothermal synthesis.[60] An asymmetric solid-state supercapacitor denoted (Co-POM/rGO//H_2SO_4/PVA//rGO) was constructed using the gel electrolyte. The device exhibited an energy density of 37.6 Wh kg^{-1} at a power density of 500 W.kg^{-1}, with strong cycling stability, retaining 95.2% capacity after 5000 charge/discharge cycles, at a current density of 2 A g^{-1} in a 2 V window.[60] Given that the energy density of SC devices is proportional to the square of the voltage window, demonstrating good retention of capacity after thousands of cycles at 2 V represents significant advancement for devices using aqueous electrolytes.

2.2 POMs as Precursor/Template for Metal Oxides and Nitrides

Several metal oxides and metal nitrides are known as electroactive materials offering fast reversible redox activity for enhancement of electrochemical performance of electrode materials. Generally speaking, metal-oxides are limited in their conductivity,[61] while metal-nitrides have limited stable voltage windows.[62] POMs offer unique avenues to address these concerns. For instance, Dubal et al. used tungsten nitride NPs derived from PW_{12}-POM to create electrodes for asymmetric SC devices.[62] The W_2N NPs produced from the POM precursor are used to decorate a carbon fabric (CF) that is further enhanced by phosphorous doping, where the phosphorous source is also the PW_{12} POM

View Article Online
DOI: 10.1039/D0EE03407J

precursor. An added benefit was that the negative potential window of the W_2N@P-CF is larger than that of tungsten nitrides previously applied to SCs (1.2 V compared to ~0.8 V).[63,64] When the W_2N@P-CF negative electrode was combined with PPy@CF for a positive electrode, the resulting devices were able to operate within a 1.6 V window. The process of producing the W_2N@P-CF electrode material is represented schematically in Figure 4 (c). Firstly, the Keggin-type PW_{12} was anchored to the CF and subsequently carbonized in NH_3 gas to form W_2N NPs. During this process, the CF is simultaneously doped with phosphorous. The extended voltage window compared to other tungsten nitrides is also proposed to be a result of the unique synthesis. The authors state it as being due to either, or both, the effect of phosphorous doping and the ultra-small W_2N particles that are produced when using the PW_{12} POM as a precursor reagent.

The same author[65] uses PMo_{12} to generate molybdenum nitride nanocrystals while simultaneously doping a CF substrate with phosphorous to generate material denoted MoN@P-CF.[65] Hexagonal molybdenum nitride MXenes, a class of 2D inorganic layered materials, anchored to boron and nitrogen co-doped CNTs have also been produced using molybdenum POMs, but in this case a Lindqvist type (Mo_7O_{24}) precursor was employed.[66] These last three reports [62,65,66] all use high temperature thermal treatment in ammonia atmosphere to achieve the nitridation of the POM-based Mo source, showing that this is an effective route to producing nanoparticle metal nitrides.

A number of Keggin-type POMs have been utilized in the synthesis of metal oxides for asymmetric SCs.[61] In a single-step procedure, $KMnO_4$ was combined with PMo_{12} and treated hydrothermally to produce α-MnO_2 “nanoflower” type product, which can be seen in Figure 5 (a-c). The hydrothermal treatment was carried out at various temperatures and for various times. PW_{12} and SiW_{12} POMs were also explored and resulted in the effective production of MnO_2 that possessed nanoparticle properties. This is an important contrast to typical metal-oxide powders that may be used for pseudocapacitive enhancement, where much larger particle sizes may be expected. In a three-electrode configuration, the PMo_{12} based MnO_2 produced at 200 °C over 24 h outperformed the other preparations, posting 235 F g^{-1} at a current density of 0.5 A g^{-1}. When the same material was tested

View Article Online
DOI: 10.1039/D0EE03407J

in an asymmetric cell using an AC counter-electrode and neutral $NaSO_4$ electrolyte the cell was able to be operated in a 2 V window and retained 91% of its 45 F g^{-1} initial (device) capacity after 5000 cycles at 3 A g^{-1}.

The above results demonstrate that nano-sized POM particles can serve as excellent precursors to nitrides and oxides for energy storage because their high surface-to-bulk ratio enables facile and complete reactive pathways towards relevant products, and because the product materials are able to retain this property. Retaining the high surface-to-bulk means that metal oxides and nitrides produced via such routes can overcome some of the perceived limitations of conductivity and electrochemical stability, since these limitations are generally associated with the bulk properties of such materials. For example, smaller particles allow intimate contact with conductive scaffold materials. It is also proposed that smaller particles promote higher voltage windows. Therefore, producing high surface-to-bulk oxides and nitrides from POMs can effectively side-step the limitations of powdered versions of such compounds to enable end-products with desirable properties.

2.3 Roadmap to POM-based Electrolytes

The use of POMs as a component of conventional liquid electrolyte in SCs are have been demonstrated but not widely explored. Skunik-Nuckowska et al.[58] used a phosphotungstate-based POM together with hydroquinone in aqueous solution as an electrolyte in a SC device where the electrodes consisted of a high performance carbon material. POMs have also been applied to other applications such as proton conducting membranes for fuel cells.[67-69] These grossly different contexts for application as electrolytes show how this class of materials may have a wide range of prospects owing to its interesting physical properties.

Wu et al.[70] synthesized a phosphotungsten vanandate-based POM and investigated its properties with the view towards application as an electrolyte. The IL studied consisted of 1-(3-sulfonic group)propyl-3-methyl imidazolium cations (MIMPS) with $4PW_{11}VO_{40}$ Keggin-based anions; $[MIMPS]_4PW_{11}VO_{40}$. Their product was a quasi-solid-state IL possessing a solid layered structure below 80 °C while transitioning to a liquid above this temperature. The electrical conductivity of the material was measured, and the authors found a significant increase in this property above the liquid transition temperature. They report values of about 10×10^{-3} S.cm^{-1} at room temperature, and 8.60×10^{-2} S.cm^{-1} at 83 °C. It was concluded that this result was due to the improved diffusion of the ions above the liquid transition temperature.[70] In a later study by Tong et al.[71] results are found for two other structurally similar POM-derived ILs, $[MIMPS]_4PMo_{11}VO_{40}$ and $[MIMPS]_3PW_{11}MoO_{40}$. The same-layered structure is confirmed by XRD results, and the authors show a transition from a solid to a liquid state above around 90 °C. The conductivity of these liquids was higher than that reported by Wu et al.[70] where they measured it to be 0.1 S.cm^{-1} for both $[MIMPS]_4PMo_{11}VO_{40}$ and $[MIMPS]_3PW_{11}MoO_{40}$, with electrochemical stability windows of 2 V and 4 V, respectively.

The above cases demonstrate the interesting characteristics of these novel types of electrolytes. However, the temperature ranges in which high ionic conductivity occurs make them more appropriate for application such as fuel cells etc. Charge storage devices like SCs generally require peak performance of the materials to fall in a window a few tens of degrees either side of ambient temperatures, making these gel-liquids unsuitable. Wu et al.[72] investigated two types of IL electrolytes consisting of POM polyanions combined with tetraalkylphosphonium (TBTP) cations. They conclude that the Dawson-type POM ($P_2W_{16}V_2O_{62}$) possesses better thermal and charge conductivity properties than the Keggin-type ($PW_{10}V_2O_{40}$) to which it was compared. These conclusions are based upon the calculated energies associated with the lattice potential and the ionic migration potential, where in both cases the Dawson-type structure shows a lower energy requirement. The $[TBTP]_8$ $P_2W_{16}V_2O_{62}$ IL shows a phase transition from solid-gel to liquid at around 50 °C which is greatly reduced against that seen in previous studies as well as against the $[TBTP]_5$ $PW_{10}V_2O_{40}$ Keggin-based IL against which it is compared (61°C), and almost reaching the ranges required for application in typical energy storage devices. Even though the above results lay just outside the range of practical use for energy storage, it is worth noting that the authors show a strong link between the improved properties of the Dawson type structure and its larger POM anion size.

View Article Online
DOI: 10.1039/D0EE03407J

This offers predictive insight for the rational design and selection of POM based electrolyte systems, which justifies further research into these ionic gel-liquid systems.

2.4 Theoretical Studies to Underpin Charge-storage in POM-Hybrids

The importance of anchoring of POMs onto a supporting scaffold has been established in previous sections. Theoretical simulations provide a powerful tool to provide insight to the binding between POMs and an associated substrate or scaffold material.

The mechanisms of bonding between carbon and POMs are not fully understood, and so to explore this further Muniz et al.[73] performed density functional theory (DFT) investigations into the electronic structure of a range of Keggin POMs ($PdMo_{12}$, $RuNb_{12}$, $SiMo_{12}$, PMo_{12} and SiW_{12}) adsorbed onto a carbon surface. These five Keggin structures were investigated for their binding lengths and electron sharing under various orientations on a carbon substrate, and neutralizing counter-ions (cations) were included to balance the charge of the Keggin anions. For $PdMo_{12}$ and $RuNb_{12}$ the calculation was fully predictive, as these systems have not, to date, been synthesized. For the SiW_{12} and $RuNb_{12}$ systems, the results indicate that functionalization of the carbon surface may not be required for sufficient anchoring and feasible use as hybrid (electrode) materials.

In 2019, Dubal et al.[65] simulated the adsorption of a number of combinations of the materials used in their study of molybdenum nitride nanocrystals. Again, the simulations were performed using DFT, in this case in the Vienna Ab-initio Simulation Package (VASP). As described in detail in section 2.1, the experimental approach in this work used CF coated with PMo_{12} as a substrate. The material was then converted to MoN@P-CF, where MoN nanocrystals were formed and the CF became phosphorous doped. Simulations reveal that the phosphorous doping of the CF enhances the energy of adsorption for protons (simulated as hydronium) over the bare carbon surface. However, the MoN@P-CF material has an adsorption energy over eight times greater than that of the phosphorous-doped CF. This theoretical element of the work strongly supports the experimental findings. Likewise, Yang and co-workers[45] employed DFT calculations to explain the origin of the enhanced redox reactions in POM/PIL/RGO nanohybrids. The van der Waals density functional

View Article Online
DOI: 10.1039/D0EE03407J

(vdW-DF) for the non-local correlation part was employed in the DFT calculations. Figure 5 (d) shows the most stable POM/PIL/graphene structure, where two POMs and one IL dimer (i.e., $2[H_2PMo_{12}O_{40}][C_{14}H_{24}N_4]$) are included in a periodic unit cell. The role of PIL and the neighbouring POM in the proton transfer process was examined by calculating adsorptions energies of a single H atom on eight different O_b and O_c sites of POM (Figure 5e). These DFT results suggest that the H adsorption energetics on a POM in the POM/PIL nanohybrids is significantly affected by adjacent PILs and POMs. From an electrostatic standpoint, the PIL cations and the POM anions suppress and facilitate the proton adsorption reaction, respectively, on the adjacent POM.

Gullen et al.[74] performed in-silico simulations of the CNT functionalization that was experimentally explored by Gallegos et al.[31] Specifically, they used DFT to investigate the bond formation between Keggin-type SiW_{12} and organic functional groups attached to a CNT. The functional groups are denoted φ-X, where φ denotes a phenyl group and X is one of $-NH_2$, -OH, -COH, or -COOH. The bond lengths are similar for the different functional pairs, however SiW_{12}@φ – COOH/CNT shows enhanced attraction over the others. Whereas the first three systems explored ($-NH_2$, -OH, -COH) exhibit van der Waals type interactions, the -COOH system exhibits a covalent-like binding energy, making its combinations with SiW_{12} a strong potential candidate for a stable hybrid system (Figure 5 f, g).[74]

The significance of the previous study is emphasized in closing this chapter – it is well known that stabilizing POMs on a graphene surface remains challenging.[75] Therefore, predicting functional groups that are more likely to result in the successful anchoring of materials like POMs, but also other classes as well, is of great importance to rationally guide research efforts. The covalent type anchoring of POMs via carboxylate groups represents a great example of how simulation can guide novel syntheses. Therefore, combining the efforts of both theoretical work and applied materials research is an effective approach to improving devices.

DOI: 10.1039/D0EE03407J

3. Development of POMs for Battery Applications

The development of high-performance rechargeable batteries, including lithium-ion batteries (LIBs) and sodium ion batteries (SIBs), is one of the most important challenges in energy storage, and arguably stands to contribute as much as any other field toward solving increasing environmental and energy issues. The charge storage in rechargeable batteries results from reversible redox reactions in the electrode active materials.[76] The stored energy in batteries can be improved by either increasing the capacity of the electrode materials or exploring new cathode materials with higher voltages.[77] The following sections explore how POMs have been able to contribute to this development.

3.1 Lithium-ion Batteries

LIBs are the preferred energy storage system for many applications due to their high voltage of more than 3.5 V per cell, high energy density of up to 200 $Wh.kg^{-1}$ and relatively long cycle life. The most common cathode materials used in LIBs are lithium transition metal oxides including layered structures such as $LiCoO_2$, spinel structures such as $LiMn_2O_4$, or olivine structures such as $LiFePO_4$. However, the changes in crystal structure of these materials during the intercalation (and de-intercalation) of lithium ions result in capacity loss during cycling. Therefore, their specific capacity is usually less than 200 $mAh.g^{-1}$.[76,78-80] For anodes, graphite is the most commonly used material in commercial LIBs. However, the theoretical capacity of graphite is low (372 $mAh.g^{-1}$), which limits its applications in large-scale systems.[77,80] Therefore, great efforts have been dedicated to developing new materials for LIBs. Recently, POMs have received much interest as electrode materials in LIBs (Table 1). The characteristic capacity and cycling stability of POMs are independent of the material's crystalline stability because the POM molecular clusters show multi-electron redox as an individual molecule. Although POMs have low electrical conductivity, using nanosized POMs and/or mixing with conductive additives can improve their electrochemical properties.[81-86] Their application to LIB research can be categorized by the POM type being used, such as by the addenda atom type, or by specific groupings of hybridized materials, such as the nanocarbon or MOF hybrids described in the following sections.

3.1.1 Molybdenum-based POMs

View Article Online
DOI: 10.1039/D0EE03407J

Phosphomolybdic acid is perhaps the most widely explored precursor to develop the electrode materials for energy storage applications. This work was pioneered in the late 90s by the group of Gomez-Romero who showed the potential of POMs in LIBs.[25] The group was able to demonstrate anchoring of POMs to the conducting polymer polyaniline, which allowed insertion and de-insertion of Li cations *without* simultaneously removing the POM anion.[87] This work was followed by the demonstration of the hybrid material as an electrode in LIBs.[88]

Much more recently, Sonoyama and coworkers [82,89] examined the electrochemical properties of a potassium-based variant of the Keggin-type polyoxomolybdate, $K_3[PMo_{12}O_{40}]$ (KPM), applying it as a cathode material for LIBs. The KPM showed a high initial discharge capacity over 200 mAh.g^{-1} in the potential range of 1.5 V - 4.2 V. Although a high capacity was achieved, KPM showed poor cycle stability, as only 37.5% of its initial capacity was maintained after 50 cycles, which resulted from the structural instability of the reduced $[PMO_{12}O_{40}]^{3-}$ cluster ion in the organic solvent. Furthermore, the calculated energy density of KPM was only 480 mW.h.g^{-1}, which is not far from that of conventional_cathode materials ($LiCoO_2$~500 mWh.g^{-1}, $LiMn_2O_4$~400 mW.h.g^{-1}). This is a consequence of the lower discharge voltage of KPM (2.5 - 1.5 V) compared to the usual LIB cathode materials. Another Keggin-type POM, namely $TBA_3[PMo_{12}O_{40}]$ (TBA; $[N(CH_2CH_2CH_2CH_3)_4]^+$) was studied by Wang et al.[90] as a cathode for LIBs. The charge storage mechanism in super-reduced $[PMO_{12}O_{40}]^{27-}$ was studied by X-ray absorption near-edge structure analysis (XANES) (Figure 6 (a)). The reversible redox reaction of the 24-electrons in $[PMO_{12}O_{40}]^{3-}$ during charging/discharging process resulted in a high capacity of approximately 260 mAh.g^{-1} at 1 mA in a voltage range of 1.5-4.2 V. Moreover, *in operando* extended X-ray absorption fine structure (EXAFS) measurements indicated that POMs behave like an electron sponge as the molecular structure size of $[PMO_{12}O_{40}]^{27-}$ shrinks when compared to the original $[PMO_{12}O_{40}]^{3-}$ (Figure 6 (b)).

The same group investigated Anderson-type polyoxomolybdate, $Na_3[AlMo_6O_{24}H_6]$ (NAM),) as LIB-cathode.[91] In order to improve the low conductivity of the POMs, NAM was mixed with two

View Article Online
DOI: 10.1039/D0EE03407J

types of conductive additives, namely ketjen black (KB) and acetylene black (AB) using two different methods such as hand grinding and ball milling. Both methods and conductive additives affect the capacity and cycling stability of NAM. The maximum discharge capacity of 437 mAh.g^{-1} was achieved, which was maintained to 399 mAh.g^{-1} after 50 cycles for ball-milled NAM/KB sample. The above results can, at least in part be explained by: (1) the improved electric conductivity, resulting from the high electrical conductivity of the KB and producing larger contact surface area between KB and NAM through ball milling, (2) the stable structure of $[AlMo_6O_{24}H_6]^{3-}$ during redox reaction (Figure 6c). However, the amount of NAM in the cathode was low (32 wt %), which can restrict the energy density of the cell. To further increase the discharge capacity and cycling stability, the nanosized POMs were used along with conductive additives.[84] The POM $(NH_4)_6[NiMo_9O_{32}]$ (ANM) was investigated using either KB or AB. In this work, four different samples were tested as LIB cathode materials; ANM microparticles hand-ground with AB (m/AB), ANM NPs hand-ground with AB (n/AB), ANM NPs hand-ground with KB (n/KB), and ANM *in situ* crystallized in KB (nanocomposite ANM/KB). Better discharge capacities and cycling performance were obtained with the n/KB and nanocomposite ANM/KB. The n/KB cathode exhibited a high initial discharge capacity of 490 mAh.g^{-1} and a very stable cycling performance, with capacity retention of 87.6% after 50 cycles. Although the nanocomposite ANM/KB cathode showed high initial capacity at low current density, it showed a poor cycling stability as compared to n/KB (61.6% after 50 cycles). This might be due to the increase in the catalytic activity of the nanocomposite ANM/KB, which leads to the formation of surface film and eventually increases its interfacial impedance. However, at high current densities (from 83 to 500 mA.g^{-1}), the nanocomposite ANM/KB showed relatively higher discharge capacity and rate-capability than that of n/KB. *Ex situ* XRD analysis indicated that the crystal structure of ANM remains amorphous during insertion and extraction of Li ions (charge/discharge processes), which enables high reversible capacity with deep discharge-charge cycles.

View Article Online
DOI: 10.1039/D0EE03407J

3.1.2 Vanadium-based POMs

Vanadium-based POMs have proven to be practical cathode materials due to their low molecular weights leading to high specific capacities and fast charging/discharging kinetics, which resulted from their stable ionic cluster.[92] The electrochemical properties of V-based POMs; bi-capped Keggin-type $(KH)_9[PV_{14}O_{42}]$ (KPV),[89] $K_7[NiV_{13}O_{38}]$ (KNiV),[81] and $K_7[MnV_{13}O_{38}]$ (KMV)[83], have been recently reported as LIB-cathode materials. These V-POMs displayed comparable discharge capacities to those of Mo-based POMs, but with much higher cycling performance. This indicates that the electrochemical stability of V-POM is not dependent on the stability of crystal structure, but rather on the stability of their cluster ions; $[PV_{14}O_{42}]^{9-}$, $[NiV_{13}O_{38}]^{7-}$ and $[MnV_{13}O_{38}]^{7-}$. KPV exhibited a high initial discharge capacity of 370 $mAh.g^{-1}$ with cycle stability of 95% over 50 cycles, which is very high compared to that reported from KPM (~37.5%). KNiV NPs were prepared by a re-crystallization method to improve the capacity and cycle performance of V-based materials. Re-crystalized KNiV delivered discharge capacities of 218.2 and 121.3 $mAh.g^{-1}$ at current densities of 17 and 167 $mA.g^{-1}$, respectively. It also showed good cycling stability with a reversible capacity of about 200 $mAh.g^{-1}$ after 24 cycles at 17 $mA.g^{-1}$. The observed high capacity and rate capability most likely result from the use of nanosized KNiV, which offers improved specific surface area and reduced diffusion lengths. Concerning KMV, micro-sized KMV (m-KMV) showed a discharge capacity of 187 $mAh.g^{-1}$ at 17 $mA.g^{-1}$. When the particle size was decreased to nanoscale, discharge capacities were increased to 308 $mAh.g^{-1}$, for the same respective current density. However, at voltages higher than 3.8 V, nanosized KMV (n-KMV) showed overcharge capacities of 37 and 15 $mAh.g^{-1}$, respectively. This may result in electrolyte decomposition, which in turn leads to the formation of a thick passivating layer on the cathode. The passivation layer decreases the ionic and electronic conduction at the cathode/electrolyte interface. This is why the authors proposed to use the mixture of nano and micro-sized KMV particles (n/m-KMV; 1:1 weight ratio) (n/m-KMV). Unsurprisingly, the n/m KMV showed improved cycle performance where a high capacity retention of ~ 97% after 50 cycles at both high and low rates was achieved.

View Article Online
DOI: 10.1039/D0EE03407J

In other work, Li et al. [93] replaced the counter cations K^+ in $K_7[MnV_{13}O_{38}]$ (KMV) (which has large equivalent mass) by NH_4^+ with a smaller equivalent mass to fabricate $(NH_4)_7[MnV_{13}O_{38}]$ (AMV). The modified AMV nanoparticles showed a reversible capacity of 234 mAh.g^{-1} at 0.5 C, which was retained at 234 mAh.g^{-1} after 100 cycles. Moreover, AMV displayed rate capability of 53% when the C-rate was increased from 1 to 5 C. An energy density of 553 mWh.g^{-1} was estimated over 100 cycles, which was two-fold higher than that of the layered Li-transition metal oxide cathodes. To prevent the electrolyte decomposition and increase the electron transport in POMs, authors [94] coated the surface of polyoxovanadate, $K_9[PV_{14}O_{32}]$ (KPV) NPs with a conducting polymer, polypyrrole (PP) (5 nm thick). In this hybrid, a thin conducting layer provides high conductivity and avoids the irreversible reactions. The capacities of 410, 415 and 300 mAh.g^{-1} were recorded for PP-KPV at current densities of 167, 500 and 1000 mA.g^{-1}, respectively. Interestingly, PP-KPV showed a cycling stability of 90% (370 mAh.g^{-1}) and 93% (280 mAh.g^{-1}) over 50 cycles at 167 and 1000 mA.g^{-1}, respectively. This confirmed that coating PP on KPV NPs suppresses electrolyte decomposition, improves rate capability and cycling stability.

Along this line, Dong and coworkers developed a symmetrical LIBs by employing $Li_7[V_{15}O_{36}(CO_3)]$ as both cathode and anode material as shown in Figure 7 (a).[95] The reason to apply $Li_7[V_{15}O_{36}(CO_3)]$ materials as both the cathode and anode might be that the vanadium centers (V^{IV} and V^{V}) in the $Li_7[V_{15}O_{36}(CO_3)]$ polyanion exhibits different redox potentials (Figure 7 (b)). The symmetric cell showed a high discharge capacity of 120 mAh.g^{-1} at 100 mA.g^{-1} and long cycle life with a capacity retention of 95% after 500 cycles at 1 A.g^{-1} (Figure 7c). High energy and power densities of 125 Wh.kg^{-1} and 51.5 kW.kg^{-1}, respectively, were obtained.

Similarly, several POM-based materials were also employed as anode materials in LIBs. For instance, $Na_7H_2[PV_{14}O_{42}]$ (NPV) is an example of the V-based POM, which was illustrated by Huang et al.[96] *In operando* characterizations confirmed the continuous reduction and oxidation of vanadium during discharging/charging process, and the electron/ion sponge behavior of $[PV_{14}O_{42}]^{9-}$ where at least 30 electrons can be reversibly stored by one NPV molecule (Figure 7d). Furthermore, it was

View Article Online
DOI: 10.1039/D0EE03407J

found that NPV is an insertion-type anode rather than conversion-type anode, indicating the independence of the capacity and cycling stability from the stability and recoverability of the NPV crystal structure. As a result, a high reversible capacity of 687 mAh.g^{-1} at 100 mA.g^{-1} was achieved with 80% cycling stability after 150 cycles. These results confirm the ability of V-based POMs to provide better capacity and cycle stability compared to other materials, however, further studies are required to achieve practical realization.

3.1.3 POM/Carbon hybrid for LIBs

As discussed earlier, the direct utilization of pristine POMs as electrode materials in energy storage devices is limited by their poor electrical conductivity and high solubility in water and many organic solvents. Thus, it is useful to consider the use of highly conductive organic materials as substrates such as conducting polymers or carbon materials for the fabrication of POM energy storage electrodes.[97] The hybridization between POMs and nanocarbons, including carbon nanotubes (CNTs) and graphene, has been proven to increase the energy storage capability of LIBs due to the combination of the redox reaction of POMs and capacitive effect of the nanocarbons.[86,98-101]

Different approaches have been developed to connect the POMs onto nanocarbon materials including covalent functionalization, in which POMs are covalently grafted onto organic moieties, and non-covalent functionalization using intermolecular interactions such as electrostatic interactions and the π- π interaction between POMs and organic materials.[102] For instance, Kawasaki et al.[85] developed a nanohybrid POMs/SWNT system as a cathode material. They expected that the nanohybridization between the POM and SWNTs would increase the lithium ion diffusion and electron transfer through the SWNTs (Figure 8 (a)). In their study, a Keggin-type POM, $TBA_3[PMo_{12}O_{40}]$ was deposited onto the surfaces of the SWNTs by electrostatic interactions. The nano-hybrid POM/SWNT delivered a capacity of 320 mAh.g^{-1} with a good cycle performance. The high capacity of the POM/SWNT system can be ascribed to the high surface area and conducting super-highway of CNTs.

View Article Online
DOI: 10.1039/D0EE03407J

Several POM/CNT composites have been developed through covalent and noncovalent bonding to improve the affinity of POMs to CNTs. For example, Song et al., [98] developed non-covalent functionalization of SWNTs with a covalently functionalized pyrene-POM hybrid (Py-SiW_{11}) and served as LIB anode. The pyrene moieties were covalently linked to the SiW_{11} clusters to form Py-SiW_{11} hybrids, which were then attached to SWNTs through both π-π stacking and electrostatic interactions. The SWNTs/Py-SiW_{11} nanocomposite exhibited a capacity of 1569.8 $mAh.g^{-1}$ at 0.5 $mA.cm^{-2}$ and capacity retention of 37 % after 100 cycles. This work was extended by covalently grafting SiW_{11}-NH_2 onto CNTs by amide bonds to prepare CNTs/SiW_{11} nanocomposites.[86] The covalent bonding introduces a stable link between the POMs and the CNTs and creates more sidewall defects in the CNTs, which results in more Li ion diffusion pathways. As an anode, CNTs/SiW_{11} nanocomposite showed a capacity of 1189 $mAh.g^{-1}$ and capacity retention of 54.6% (650 $mAh.g^{-1}$) after 100 cycles. They also prepared a ternary PMO_{12}/PANI/MWNTs nanocomposite through noncovalent functionalization to further improve the connection between POMs and CNTs.[99] This was achieved by using conductive polymers, which have strong π-π interaction with CNTs and strong electrostatic interaction with POMs. The electrochemical investigation of the PMO_{12}/PANI/MWNTs nanocomposite as a LIB anode resulted in a capacity of 1572 $mAh.g^{-1}$, which was retained at 1000 $mA.h.g^{-1}$ (63.6%) after 100 cycles at 0.5 $mA.cm^{-2}$.

The capacitive effect of POM/nanocarbon composites can be further improved by using graphene, which has higher available specific surface area than CNTs. Hence, several studies regarding POM/graphene nanocomposites have been reported for capacitive-type devices.[39,50,57] These types of composites are also appealing for battery applications, for example, Wang et al.[100] reported a Keggin-type SiW_{12}/rGO nanocomposite as a cathode material for LIBs. A capacity of 275 $mAh.g^{-1}$ was achieved at a current density of 50 $mA.g^{-1}$, which was ~1.7 times higher than that of the pure SiW_{12} (160 $mAh.g^{-1}$). Kume et al.[103] developed $TBA_3[PMo_{12}O_{40}]$/rGO hybrid as LIB cathode material by grafting POM molecules onto the surface of rGO (Figure 8 b, c), demonstrating a capacity of ~140 $mAh.g^{-1}$ with a stable capacity over 10 cycles. Likewise, Xie et al.[101] prepared

View Article Online
DOI: 10.1039/D0EE03407J

ethylenediamine-functionalized rGO (EDAG)/Anderson-type $Na_3[AlMo_6O_{24}H_6]$ (NAM) composite and tested as anode in LIBs. The material showed a discharge capacity of 1835 $mAh.g^{-1}$ at 100 $mA.g^{-1}$. Further work to improve the capacity and cycling stability of POM/graphene nanocomposites was performed by Ni et al.[104] A 3D graphene/polyaniline/POM hybrid (rGO@PANI/PW_{12}) was developed as LIB-cathode, which showed a specific capacity of 285 $mAh.g^{-1}$ at 50 $mA.g^{-1}$ with good rate capability (140 $mAh.g^{-1}$ at 2 $A.g^{-1}$) and excellent cycling stability (only 0.028% loss per cycle capacity) over 1,000 cycles. The high capacity and good cycle stability of the reported (rGO@PANI/PW_{12}) cathode can be attributed to the fast electron transfer from reduced PANI polycation to PW_{12} polyanion, as well as the high redox properties of the PW_{12}. Nevertheless, deeper insight and understanding into the nature of the charge transfer between the POMs and the conducting supports is required in order to realize their practical application in LIBs.

3.1.4 POMs/Metal-Organic Frameworks (POMOFs)

Metal-Organic Frameworks (MOFs) is a new class of porous materials, which has attracted tremendous attention due to their unique surface and structural properties. Recently, MOFs are also investigated as host to immobilize POMs to prevent their solubility in organic electrolytes.[105-111] The combination of POM and MOFs is hereafter referred as POMOFs. The unique combination of features of both POMs and MOFs such as open porous structures and redox-rich chemistry makes them potential materials for LIBs. Recently, Yue et al.[110] designed a POMOF, which consists of (Ni_6PW_6) structural building units and rigid carboxylate linkers. When applied as anode in LIBs, this POMOF showed a discharge capacity of 1421 $mAh.g^{-1}$ at 1.25 C with a reversible capacity of about 350 $mAh.g^{-1}$ after 500 cycles. At low C-rate of 0.25 C, a high discharge capacity of 1525 $mAh.g^{-1}$ was measured, which was retained to 540 $mAh.g^{-1}$ after 360 cycles. Huang et al.[105] synthesized crystalline POMOF with an ultra-stable structure by connecting Zn-ε-keggin, [ε-$PMo_8{}^{v}Mo_4{}^{VI}O_{37}(OH)_3Zn_4$] with TPT ligands, (TPT=tris-(4-pyridyl)triazine) to fabricate $[PMo_8{}^{v}Mo_4{}^{VI}O_{37}(OH)_3Zn_4][TPT]_5\cdot 2TPT\cdot 2H_2O$ (NNU-11) with π-π stacking interactions. The material was further tested as anode material in LIB, which showed a capacity of 1322.3 $mAh.g^{-1}$

View Article Online
DOI: 10.1039/D0EE03407J

with a stable reversible capacity of 750 mAh.g^{-1} over 200 cycles. The authors also synthesized two thermally-stable POMOFs with diamond topology, $(TBA)_3[PMo_8{}^{V}Mo_4{}^{VI}\ O_{38}(OH)_2Zn_4(IN)_2]$ (NENU-506) and $(TBA)_3[PMo_8{}^{V}Mo_4{}^{VI}\ O_{38}(OH)_2Zn_4(PBA)_2]\cdot H_2O$ (NENU-507) (where IN = isonicotinic acid, TBA = tetrabutylammonium ion, H PBA = 4-(pyridin-4-yl) benzoic acid).[107] When these two POMOFs were used as anode materials, the better cycling stability was obtained for NENU-507, which delivered a reversible capacity of 640 mAh.g^{-1} at 100 mA.g^{-1}.

Several studies have been conducted by Lan's group in order to improve the electronic conductivity of POMOFs. For instance, they reported on POMOF-based $PMo_{10}V_2$/rGO nanocomposites as LIB-anode. The composite exhibited a reversible capacity of 1075 mAh.g^{-1} at 50 mA.g^{-1} and cycling stability of nearly 100% at both 2000 and 3000 mA.g^{-1} current densities after 400 cycles.[108] They also used ILs to increase the conductivity of POMOFs by encapsulating ILs into POMOFs and fabricate a series of POMs-ILs@MOFs crystals.[111] Among those, $PMo_{10}\ V_2$-ILs@MIL-100 crystals showed an excellent cycling stability with a high capacity of 1248 mAh.g^{-1} at 0.1 A.g^{-1} after 100 cycles as LIB-anode material. Likewise, Li et al.[106] reported POMOF (CuPW)/SWNTs composites, (CuPW=($[Cu_{18}(trz)_{12}\ Cl_3(H_2O)_2][PW_{12}O_{40}]$) as anode materials where SWNTs were utilized as a conductive scaffold. The material showed a reversible capacity of 885 mAh.g^{-1} after 170 cycles at 100 mA.g^{-1}. The high capacity and reasonable rate performance can be ascribed to the high specific surface area and the improved electric conductivity due to SWNTs.

From the above results, it is apparent that the POMOF/conductive composites have great potential to achieve high capacity and good cycle stability for LIBs applications. However, the complicated synthesis methods and the difficulty of anchoring the charge-balanced POMOFs on the negatively charged carbon supports limit their practical applications. Therefore, finding new simple synthesis methods to improve the conductivity of POMFs is highly demanded.

3.2 Sodium-ion Batteries

Sodium-ion batteries (SIBs) are a promising technology for large-scale energy storage applications due to the large abundance of sodium in the Earth-crust (23×10^3 ppm) and it also permits the use of low-cost aluminum as a current collector for both anode and cathode materials. The latter is possible because sodium does not alloy with aluminum, unlike lithium.[112-114] However, their energy density is low compared to LIBs because of the large radius of the Na^+ ions (Na^+: 1.02 Å vs Li+: 0.67 Å), large atomic weight (Na: 23 vs Li: 7) and low operating potential (Na: 2.71 V vs Li: 3.04 V).[114] Therefore, many studies have aimed to overcome these disadvantages by exploring and developing new cathode materials. Although POMs have been widely used in both cathodes and anodes in LIBs with good capacity and cycling stability, few studies have been conducted on POM-based SIBs. For instance, Liu et al.[113] reported on $Na_2H_8[MnV_{13}O_{38}]$ (NMV) as a SIB cathode material by coating NMV nanoplates on graphene sheets to fabricate a robust NMV/G composite. *Ex-situ* X-ray photoelectron spectroscopy (XPS) and Fourier-transform infrared (FT-IR) spectroscopy analyses showed that the NMV cathode acts as an electron/Na^+ ion sponge, in which $[MnV_{13}O_{38}]^{9-}$ is reduced to $[MnV_{13}O_{38}]^{20-}$ by storing 11 electrons with an expansion in size of ~7.5% (Figure 9). The NMV/G composite demonstrated a high reversible capacity of ~190 $mAh.g^{-1}$ at 0.1 C with good rate capability (130 $m.h.g^{-1}$ at 1 C), and capacity retention of 81% (140 $mAh.g^{-1}$) after 100 cycles. Similarly, Chen et al.[95] used $Li_7[V_{15}\ O_{36}\ (CO_3)]$ as a high capacity cathode material for SIBs. According to electrochemical investigations and DFT, $(V_{15}\ O_{36}\ (CO_3))$ can transport and store large numbers of large cations such as Na^+. A reversible specific capacity of 240 $mAh.g^{-1}$ was obtained at a current density of 50 $mA.g^{-1}$ and a stable reversible capacity of 190 $mAh.g^{-1}$ was retained after 30 cycles at 100 $mA.g^{-1}$.

The vanadium-based POM, $Na_6[V_{10}O_{28}]\cdot16H_2O$, has been reported by Hartung et al. as an anode material for SIBs.[112] Na^+ is (de)inserted (from) into the space between the individual $[V_{10}O_{28}]^{6-}$ clusters instead of intercalating into their crystal structures, which resulted in the capacity of ~276 $mAh.g^{-1}$ at 20 $mA.g^{-1}$. Xie and coworkers[101] employed NAM-EDAG (NAM: Anderson-type $Na_3[AlMo_6O_{24}H_6]$, EDAG: ethylenediamine-functionalized rGO) as anode for SIB and found a reversible Na storage capacities of ~150 and ~50 $mAh.g^{-1}$ after 150 and 200 cycles, respectively. However, these values are much lower than those previously reported for LIBs (> 1000 $mAh.g^{-1}$ after

100 cycles). These low capacities can be related to sluggish electrode kinetics due to the formation of a Na_2O passivation layer during the first charging/discharging cycles; however, future research is needed to validate this conclusion. Another SIB anode material based on POMs, $Na_7[H_2PV_{14}O_{42}]\cdot nH_2O$ (NPV) (n=15-24), was reported by Lin et al.[115] This anode showed a high reversible capacity of 322 mAh.g^{-1} at 25 mA.g^{-1} and high cycling stability 87% after 120 cycles.

3.3 POM-based Redox Flow Batteries

Redox flow batteries (RFBs) are an emerging technology for stationary energy storage. Unlike conventional secondary batteries they utilize liquid electrodes.[116,117] RFBs use two redox-active solutions with different redox potentials, known as an anolyte and catholyte. The two solutions are stored in separate containers and are continuously pumped through battery stack compartments where reversible redox reactions can occur at the interface of each inert electrode.[118] The anolyte and catholyte solutions are separated by an ionic conducting membrane or separator, which allows the transport of charge carrying ions. A schematic diagram of a RFB is shown in Figure 10. The unique design and the working mechanism of the RFB offers several promising features. As an example, their flexible modular design allows RFBs to be sized, as required, to cover a wide range of energy and power requirements of the consumer market. The energy and power characteristics of RFBs are not as explicitly coupled with each other when compared to other classes of batteries. This is due to the electrolyte and electrode being stored in separate containers. The de-coupling of these characteristics makes them unique for commercial application.[117] In case of RFBs, the energy capacity is related to the volume of the electrolyte reservoirs, while the power capability depends upon the size of the battery stack. These highly customizable features of RFBs make them one of the most promising technologies for stationary energy storage.

In 1970, the National Aeronautics and Space Administration (NASA) proposed the concept of RFBs for the first time, using the ferric/ferrous and chromic/chromous as an electrolyte solution. However, the limited cycling stability and the excessive hydrogen generation at the negative electrode limited the use of ferric/ferrous and chromic/chromous as practical electrolyte solutions for RFBs.[119]

View Article Online
DOI: 10.1039/D0EE03407J

To enhance the energy density and achieve good cycling stability, various redox active species have been investigated.[120] On the basis of classification by active redox species, these RFBs can be divided as follows: all-vanadium, polysulphide/bromine, zinc/bromine, vanadium/cerium.[121,122] Each flow battery system has certain advantages and disadvantages. Recently, POMs have been also studied in RFBs to enhance their electrochemical parameters. Pratt et al.[123] developed RFBs by using the phosphorus-based POMs ($A\text{-}\alpha\text{-}PV_3W_9O_{40}^{6-}$, $B\text{-}\alpha\text{-}PV_3W_9O_{40}^{6-}$, and $P_2V_3W_{15}O_{62}^{9-}$). The electrochemical measurements show that the vanadium centers of these compounds could be used as the positive electrode ($PV^{IV}_3W^{VI}_9O_{40}^{9-}/PV^{V}_3W^{VI}_9O_{40}^{6-}$) and that the tungsten centers could be used as the negative electrode ($PV^{IV}_3W^{VI}_9O_{40}^{9-}/PV^{IV}_3W^{V}_3W^{VI}_6O_{40}^{12-}$). Similarly, $[SiV^{V}_3W^{VI}_9O_{40}]^{7-}/[SiV^{IV}_3W^{VI}_9O_{40}]^{10-}$ could be used at the positive electrode and $[SiV^{IV}_3W^{VI}_9O_{40}]^{10-}/[SiV^{IV}_3W^{V}_3W^{VI}_6O_{40}]^{13-}$ at the negative electrode, $[(SiFe_3W_9(OH)_3O_{34})_2(OH)_3]^{11-}/[(SiFe_3W_9(OH)_3O_{34})_2(OH)_3]^{14-}$ at the positive electrode and $[(SiFe_3W_9(OH)_3O_{34})_2(OH)_3]^{17-}/[(SiFe_3W_9(OH)_3O_{34})2(OH)_3]^{14-}$ at the negative electrode for the RFBs.[124,125] However, the low coulombic efficiency and the poor cycling stability of the POM-based anolyte and catholyte solutions are challenges that still need to be addressed to make them suitable as candidates for RFB applications. Not surprisingly, the hybridization of POMs with another conducting material has recently been proposed to enhance the electrochemical performance of POM-based RFBs.[126,127] Dubal et al. proposed the hybridization of graphene and POMs (phosphomolybdate and phosphotungstate) for flow energy storage application.[127] The distinctive feature of this work was the use of the customized hybrid electrolyte in a proprietary miniature flow reactor to study the electrochemical features. Remarkably, rGO/phosphomolybdate based flow cells showed encouraging electrochemical features including specific capacitance of 305 $F.g^{-1}$ with cycling stability (~95%) as well as aa strong Coulombic efficiency (~77–79%) after 2000 cycles. The electrochemical results obtained for these POM based RFBs are still far from the vanadium RFBs.[128] Therefore, more efforts and new approaches are necessary to utilize POMs as liquid electrodes in RFBs.

4. Engineering of POM-based Materials for Catalysis

DOI: 10.1039/D0EE03407J

The Keggin types of POM are best suited for catalysis application as they are uniquely stable amongst other structural motifs. As a result, they have already been applied in various industrial processes as a catalyst.[129] They owe their extraordinary catalytic properties to the presence of numerous active sites per molecule. Their proton binding sites promote acid-catalyzed reactions and their electron-rich oxygen sites promote base-catalyzed reactions. However, the most important active sites in POM/heteropolyacid (HPA) compounds are at metal atoms, which take part in all oxidative reactions, some acid-catalyzed reactions, and other reactions. The precise active sites of POMs depend upon the type of reaction. As a catalyst used in oxidative reactions, POM/HPA (mostly W/Mo-based) compounds are well explored. In the case of substituted W/Mo, the active sites depend upon the type of metal ion substituted. Considering the variety of the metals that can be introduced into POMs, these active sites can be engineered to tailor their properties for specific applications.

In recent years, research on materials for clean and sustainable energy sources has grown substantially. Splitting water to produce hydrogen and oxygen is one convenient way for energy conversion.[130] Due to their stability and extensive tunability, POMs are attractive as water reduction catalysts for the hydrogen evolution reaction (HER), and most expansively, water oxidation catalysts (WOCs) for the oxygen evolution reaction (OER).[131-133] Indeed, POMs have been successfully implemented in the fabrication of overall water splitting systems.[134] On the other hand, electrochemical oxygen redox reactions are considered to be the key for energy conversion and storage including fuel cells and metal–air batteries.[135] In general, fuel cells devices are based on the electrocatalytic oxidation of a fuel (e.g. hydrogen and methanol) at the anode and the oxygen reduction reaction (ORR) at the cathode. Notably, OER (section 4.1) and ORR (section 4.2) are the two fundamental reactions in fuel cells and energy storage devices. In ORR, strong double bonds have to be broken for the formation of hydroxyl or peroxide ions from oxygen molecule and vice versa is true for OER, both reactions involving four electrons. Hence, they are often described as sluggish compared to their anodic counterparts, namely hydrogen evolution and oxidation which are

View Article Online
DOI: 10.1039/D0EE03407J

two electron processes.[136] Therefore, it is necessary that the catalysts used for ORR and OER are highly active for achieving better performance parameters of the devices, which has stimulated the development of novel water oxidation and oxygen reduction catalysts over the past years. Furthermore, the fascinating properties of POMs, including tunable acidity and redox properties, have stimulated the research in a wide range of POM-catalyzed applications[137] including other catalytic reactions such as CO_2 reduction, N_2 reduction and biomass conversion (section 4.3).

4.1 Water Oxidation

Water oxidation involves the dissociation of protons and electrons from stable water molecules, as well as the formation of an O−O bond from formally separated water molecules. The overall OER process typically occurs via four elementary steps involving different reaction intermediates and the formation of an O–O bond (eventually released as O_2). This latter step has been proposed to occur through two primary pathways, the water nucleophilic attack (WNA) and the interaction of two metal-oxo entities (I2M).[138] As shown in Figure 11, both reaction paths begin with two proton electron transfer (PET) events, giving rise to a metal-oxo intermediate. The WNA mechanism involves the nucleophilic attack of a solvent water molecule together with a PET resulting in a hydroper-oxo intermediate, which finally evolves molecular oxygen via another PET. On the other hand, the O–O bond formation in the I2M mechanism involves the coupling of two separate metal-oxo moieties, leading to a peroxo species that eventually produces O_2 and regenerates the catalyst. In addition to the intrinsic thermodynamic demands of water splitting, kinetic obstacles impose significant activation energies (overpotentials) and require the development of efficient catalysts.[129] WOCs composed of all-inorganic POMs have advanced the field of water splitting over the past decade.[131] Lacunary POMs, "defect" structures made by removing M=O entities, are good inorganic multidentate ligands to stabilize multi−metal oxide clusters. Thus, the robust structure of lacunary POM ligands have been exploited for the assembly of catalytically active transition metal-oxo clusters. Herein, in the following section we discuss the progress on POM WOCs organized in terms of the transition metal providing the active sites in the catalyst. Comparison of the catalytic

View Article Online
DOI: 10.1039/D0EE03407J

activity of different systems is only possible in the case of uniform experimental conditions for all water oxidation catalytic species. However, since not all systems can perform under the same combination of conditions, comparison of different catalysts should be done with caution. As discussed by Hill et al,[133,139] there have not been any established agreements on how to compare catalyst's activity of different systems in the literature. Nevertheless, in the following section catalysts will be often compared in terms of turnover numbers (TON: ratio of product formed per catalyst molecule) and turnover frequencies (TOF: d(TON)/dt) under analogous experimental conditions.

4.1.1 Ruthenium-based POM WOCs

Ru-based catalysts are interesting because of their ability to act as a powerful oxidant in near-neutral pH conditions. In 2008, Bonchio [140] and Hill [141] groups simultaneously reported $[Ru_4O_4(OH)_2(H_2O)_4(SiW_{10}O_{36})_2]^{10-}$ (Ru_4Si_2) as a highly-active WOC using strong oxidants. The structure of Ru_4Si_2 consists of a tetra-nuclear Ru(IV) aqua-ion, $[Ru_4(O)_4(OH)_2(H_2O)_4]^{6+}$, entrapped by the assembly of two kegging-type lacunary $[SiW_{10}O_{36}]^{8-}$ POM units (Figure 12a). The active site of the compound is the $[Ru_4O_4]$ core with adjacently coordinated aqua ligands, which undergo four consecutive oxidation steps, from Ru^{IV}_4 to Ru^{V}_4, followed by nucleophilic attack and water oxidation.[142-145]

In 2009, Geletii et al. studied Ru_4Si_2 as an efficient homogeneous WOC at neutral pH for visible-light-driven water oxidation.[146] This well-established technique is based on the facile generation of the oxidant $Ru(bpy)_3^{3+}$ by photoinduced electron transfer between the photosensitizer (PS) (e.g., $Ru(bpy)_3^{2+}$) and an appropriate sacrificial electron acceptor (SA) (e.g., $S_2O_8^{2-}$). Under the experimental conditions described in Figure 12 b, the Ru_4Si_2 catalyst showed high TON of up to 180, as well as initial TOF of up to 0.08 s^{-1} and the overall quantum yield (Φ: moles of generated product/moles of absorbed photons) as high as 4.5%. Later, the congeneric POM catalyst $[Ru_4(O)_5(OH)(H_2O)_4(PW_{10}O_{36})_2]^{9-}$ Ru_4P_2 was synthesized and shown to be a WOC, although it was somewhat less efficient (lower O_2 yields under similar photochemical conditions).[147]

View Article Online
DOI: 10.1039/D0EE03407J

Hole scavenging ability is a key parameter in the electron-transfer (ET) rate between the photogenerated oxidant $Ru(bpy)_3^{3+}$ and the catalyst Ru_4Si_2, leading to O_2 evolution. The catalyst must be able to scavenge the holes in $Ru(bpy)_3^{3+}$ in competition with charge recombination. In an effort to shed light on hole scavenging, Orlandi et al. performed a nanosecond laser flash photolysis investigation on the hole transfer reaction from photogenerated oxidant $Ru(bpy)_3^{3+}$ complexes to catalyst Ru_4Si_2.[148] The oxidant species generated by oxidative quenching with a SA in homogeneous solution showed very fast hole scavenging from photogenerated Ru^{III} species to Ru_4Si_2. However, at high catalyst concentrations, the electrostatic interaction between the PS, $Ru(bpy)_3^{2+}$, and Ru_4Si_2 leads to efficient static quenching of the $Ru(bpy)_3^{2+}$ excited state.[149] This energy wasting process is detrimental to photocatalytic activity, as it competes appreciably with the primary photoreaction of the excited PS with the SA, even in high ionic strength media. In this context, keeping the catalyst concentration as low as possible can prevent quenching of excited $Ru(bpy)_3^{2+}$, however, at the cost of slowing the hole-transfer process. Another strategy to overcome this issue is the use of PSs that favor the productive, reductive quenching of the excited PS by Ru_4Si_2 rather than the unproductive oxidative quenching. This implies the use of PSs being strong electron acceptors in the excited state, such as a tetranuclear dendrimeric Ru^{II} polypyridine complex [150,151] or multi-perylene-bisimide chromophores.[152]

In the common oxidative quenching pathway in the presence of an SA, oxidized PS is irreversibly produced so that, in principle, fast hole transfer is not a strict requirement. In practice, however, the PSs, in their oxidized form, are often unstable under the reaction conditions used and fast hole scavenging is pivotal to minimize their decomposition (usually the main limiting factor in terms of turnover performance). As electron transfer from catalyst to PS is primarily diffusion controlled, PS degradation can be mitigated on a photoelectrode, where a close contact exists between the two components and transfer of electrons from the catalyst occurs rapidly after oxidation of the PS.[148] Several triadic photoanodes composed of nanoporous MO_2 (M = Ti, Zr and Sn) films sensitized with different cationic Ru PSs have been reported.[153-155] The surface-bound cation electrostatically

View Article Online
DOI: 10.1039/D0EE03407J

interacts with negatively charged Ru_4Si_2. In the presence of Ru_4Si_2, the electron transfer from the PS to MO_2 was found to be the main pathway, with ultrafast (nanosecond) electron transfer from Ru_4Si_2 to the oxidized PS. The oxidized catalyst is long-lived and thus, it energetically reacts with H_2O to produce O_2. When using 3-aminoproyltriethoxysilane (APS) in particular, amine groups can be readily displayed on photoelectrode surfaces by its hydrolytic condensation and used to immobilize Ru_4Si_2 electrostatically, the very high charge of Ru_4Si_2 (10−) render these catalyst−surface linkages very robust. Hill's group reported that Ru_4Si_2 and Ru_4P_2 can be electrostatically adsorbed on TiO_2 [156] or Fe_2O_3 [157] photoanodes after modification with APS. Under ultraviolet (UV) illumination, photoelectrochemical measurements indicated an enhanced photocurrent compared to un-functionalized photoanodes. Moreover, atomic layer deposition was successfully used to protect the attachment of POM WOCs on the surface of visible-light-absorbing hematite (Fe_2O_3) photoanodes.[157] Instead of immobilization within a host material with a well-defined porous structure, it is also possible to immobilize catalysts by *in situ* hybridization with polymeric materials on the surface of photoelectrodes. Very recently, Ru_4Si_2 was co-deposited on WO_3 photoanodes with various electropolymerized conducting polymers.[158] The photoelectrochemical performance for visible-light-driven water oxidation of WO_3 photoanodes can be remarkably improved only when co-depositing polypyrrole (PPy) and Ru_4Si_2 due to the desired energy level alignment for efficient charge transfer.

Electrochemical water oxidation has been demonstrated using Ru_4Si_2. In 2010, Toma et al. reported the effective anchoring of Ru_4Si_2 onto a conductive bed of MWCNTs as the conductive substrate to form an active water oxidation electrocatalyst (Figure 13).[159] Compared to amorphous carbon functionalized with Ru_4Si_2, the electrocatalytic activity of Ru_4Si_2 on the derivatized MWCNTs was significantly higher, presumably due to the enhanced electron transfer events in the MWCNTs. The TOF of 300 h^{-1} at an overpotential of (η) 0.60 V, exceeds the values reported previously for Co-oxide and Mn-cluster systems, which were in the range 0.7 – 20 h^{-1} at $\eta \geq 0.40$ V.[160,161] Similarly, covalent and noncovalent approaches to functionalize CNTs with cations have been explored.[162]

View Article Online
DOI: 10.1039/D0EE03407J

An improvement of the electrocatalytic performance of Ru_4Si_2 is conferred by using graphene covalently functionalized with organic hydrogen-bonding cations.[163] This hybrid material catalyzes oxygen evolution at a η as low as 0.3 V at neutral pH with negligible loss of performance after 4 h of testing, outperforming the catalytic efficiency of the isolated Ru_4Si_2 by one order of magnitude, with a two-fold enhancement compared to the nanotube analogs. Based on the observation that graphene without a modified surface can adsorb Ru_4Si_2 strongly, Ru_4Si_2 was immobilized electrostatically onto graphene electrochemically deposited on a glassy carbon or indium tin oxide (ITO) electrode.[164] The composite material showed excellent catalytic activity and high stability under neutral pH conditions with a moderate η of 0.35 V. Moreover, Ru_4Si_2 on graphene displayed higher catalytic activity compared to RuO_2 on graphene, where the amount of RuO_2 would be ~200 times more than the amount possible from complete decomposition of Ru_4Si_2.

Another surface entrapment technique to fabricate catalytic electrodes consists of the employment of a conducting polypyrrole matrix and the layer-by-layer (LbL) technique. Ru_4Si_2 was successfully immobilized onto polypyrrole-modified glassy carbon and ITO surfaces by alternate deposition of anionic Ru_4Si_2 and a Ru(II)-metallodendrimer as the cationic moiety.[165] The Ru_4Si_2-based LbL assemblies exhibited enhanced electrocatalytic abilities in pH-7, in comparison to both Ru_4Si_2 paste electrodes and LbL assemblies composed of the Ru-free parent POM moiety. Apart from Ru_4Si_2 and its analogous Ru_4P_2, other Ru-based POM WOCs have also been reported. In 2011, Murakami et al. synthesized and characterized two mononuclear complexes $[Ru^{III(}H_2O)SiW_{11}O_{39}]^{5-}$ and $[Ru^{III(}H_2O)GeW_{11}O_{39}]^{5-}$ for water oxidation with the strong oxidant $(NH_4)_2[Ce^{IV}(NO_3)_6]$.[166] Maximum TONs of up to 20 and 50 were reported, respectively. These catalysts turned to be less robust than Ru_4Si_2, despite the exposed and accessible metal center. DFT calculations indicate that the $Ru^{III}–H_2O$ center can accommodate a stepwise multi-electron redox processes at the high reduction potential condition of Ce^{IV}/Ce^{III} to achieve the active group $[Ru^V{=}O]$, and the high valent oxo-Ru^V species are responsible for the O–O bond formation event.[167] The calculated results support that the bridging O atom of the POM ligand will act as the most favorable proton acceptor in the O–

O bond formation, with an energy barrier of 28.43 kcal.mol^{-1}. Car et al. synthesized a triruthenium-substituted POM, $[(Ru_3O_3(H_2O)Cl_2)(SiW_9O_{34})]^{7-}$, that features a capping (Ru_3) unit connected to a lacunary $[SiW_9O_{34}]^{10-}$ POM shell via Ru–O.[168] The maximum TON (23) under photocatalytic conditions was reached after 120 min, with higher TOF (0.7 s^{-1}) than the previous results for Ru–POMs. The WOC activity was derived from the formation of a recyclable POM–photosensitizer complex in the initial stages of the reaction that hinders POM decomposition into RuO_x catalysts.

4.1.2 Cobalt-based POM WOCs

The current approach for the development of more sustainable catalysis is the use of metals with high crustal abundance. In this context, the discovery of the first Co-based POM WOC represented a great breakthrough in the field given its higher abundance than Ru. For example, reported in 2010 by Yin et al., $[Co_4(H_2O)_2(PW_9O_{34})_2]^{10-}$ (Co_4P_2), a tetra-cobalt complex protected by two $[PW_9O_{34}]^{9-}$ ligands, showed water oxidation activity with TONs reaching ~ 10^3 in under 3 min in the presence of the chemical oxidant $[Ru(bpy)_3]^{3+}$ at pH 8.[169] In later studies, Co_4P_2 activity was noted and studied for light-driven water oxidation using $Ru(bpy)_3^{2+}$as the PS and $S_2O_8^{2-}$ as the SA.[170] Co_4P_2 showed remarkably superior photocatalytic performance to that of the Ru_4Si_2 catalyst,[146] with a TOF of $\approx 5s^{-1}$, Φ of 30% and a TON > 220. Co_4P_2 enwrapped into ordered mesoporous carbon nitride (MCN) exhibited noticeable electrocatalytic activity in water oxidation.[171] At 1.4 V vs Ag/AgCl, the TOF reaches up to 0.3 s^{-1} at pH 7, which is nearly 6 times higher than that with Ru_4Si_2@MWCNTs (0.055 s^{-1} at 1.4 V).[159]

The activity of Co_4P_2 as a homogeneous WOC is subject to some debate. For instance, Finke's group first demonstrated that under electrocatalytic conditions, Co^{II} leaching from Co_4P_2 can deposit onto the anode as cobalt oxide (CoO_x) film that rapidly becomes the major catalyst.[172] Since then, the integrity of Co_4P_2 has been carefully examined through a plethora of studies,[173-177] leading to the conclusion that the specific conditions such as buffer, pH, and catalyst concentration matter greatly in determining the true WOC. Ultimately, Hill's group demonstrated that Co_4P_2 is indeed the main WOC under the homogeneous conditions reported originally.[178] The authors described a new protocol for the extraction of highly negatively charged POM WOCs using heptylammonium nitrate (THpANO$_3$) dissolved in toluene to identify the active species for water oxidation. In the end, Co$_4$P$_2$ has become a prime example for stability analysis of POM WOC systems and studies aiming to identify the main active species. Indeed, the atomic structures of POMs are highly amendable under different conditions of pH, applied potential and chemical environments, leading to ambiguity when interpreting the catalytic behaviours of OER studies. [179170, 169] Very recently, Folkman et al. reported phosphorous-31 nuclear magnetic resonance (NMR) and cathodic stripping analysis to determine the amount of detectable Co^{II}(aq) in solutions of a series of six exemplary Co-POMs (including Co$_4$P$_2$[180]￼). Higher pH values and phosphate buffer in general led to higher levels of Co^{II}(aq). However, under pH 5.8 the Co-POMs exhibited higher stability, where the amount of Co^{II}(aq) detected cannot account for the observed electrochemical water oxidation activity. It seems that the specific conditions are important in determining the identity of the dominant WOC. This study exemplifies a valuable methodology for distinguishing between homogeneous and heterogeneous WOCs derived from Co-POMs, even when metal-leaching is present at just micromolar levels. Furthermore, under the umbrella of WOC optimization, advanced *in situ*/operando analytical techniques (such as X-ray absorption spectroscopy, XPS, X-ray scattering techniques among others) are being developed as increasingly powerful tools to elucidate the controversial discussions about the molecular or nanoscale nature of many POM WOCs. More and more of these approaches also enable the monitoring of possible key intermediates as an essential prerequisite for proposing catalytic mechanisms. An overview of emerging *in situ*/operando approaches as new strategies for monitoring WOC transformations has been published recently.[181]

Recent advances in heterogenizing POMs on electrode surfaces provide protocols and criteria to assess the stability, rates, and molecular nature of immobilized WOCs. For example, MOFs have been used to encapsulate Co$_4$P$_2$ displaying enhanced photocatalytic and electrocatalytic water oxidation activity as well as improved stability facilitated by the electrostatic interaction with the MOF.[182] Recently, Co$_4$P$_2$ has been immobilized in the hexagonal channels of a porphyrinic MOF

(MOF-545) hybrid framework (Figure 14a),[183] with the catalyst and the PS (porphyrin linker) within the same porous solid material. As shown in Figure 14b, O_2 was formed immediately upon exposure to light and increased linearly with time, exhibiting high photocatalytic activity (TOF = 40×10^{-3} s^{-1} for the first 15 min and TON of 70), good stability and easy recyclability.

It is also possible to immobilize Co_4P_2 by *in situ* hybridization with polymeric materials on the surface of photoelectrodes. Recently, a synthetic melanin thin film incorporating Co_4P_2 was readily deposited on the surface of various n-type inorganic semiconductors (e.g., Fe_2O_3, $BiVO_4$, and TiO_2) by electropolymerization.[184] The formation of a melanin-based p–n heterojunction structure results in an increased photocurrent density and decreased onset potential for water oxidation when compared to the bare semiconductor photoanodes. In a different approach, electrostatic, non-covalent immobilization strategies have been employed for the immobilization of Co_4P_2. Photoanodes for solar water oxidation have been fabricated by depositing a thin film of diverse cationic polyelectrolytes and anionic Co_4P_2 on the surface of various photoelectrode materials using the layer-by-layer (LbL) assembly technique.[185] It was found that the performance of photoanodes was significantly improved after the deposition in terms of stability as well as photocatalytic properties, regardless of types of photoelectrodes and polyelectrolytes employed. Very recently, the Ag^+ salt of Co_4P_2 was exploited as a hole extraction layer on the surface of $BiVO_4$ semiconductor photoanode for boosting photoelectrochemical activity by promoting hole extraction and transfer.[186] The $BiVO_4/Co_4P_2$ composite exhibited a pronounced water oxidation photocurrent density of 3.06 $mA.cm^{-2}$ at 1.23 V vs. RHE under (compared to the pure $BiVO_4$ 0.93 $mA.cm^{-2}$), achieving a 3.3-fold improvement in photocurrent density. Furthermore, after the $BiVO_4/Co_4P_2$ photoanode was further treated by UV light irradiation, a photocurrent enhancement was achieved, bringing the photocurrent density to 4.03 $mA.cm^{-2}$, showing great potential for application in photo-electrocatalytic water oxidation.

For P- and Si- heteroatoms, Ru_4Si_2 displayed higher water oxidation activity than Ru_4P_2 under photochemical conditions. For that reason, Zhu et al. attempted to synthesize the Si-centered analog of Co_4P_2, but unexpectedly obtained the tetra-Co-sandwiched POM $[Co_4(OH)(H_2O)_3](Si_2W_{19}O_{70})]^{11-}$

as a 1:1 mixture of two isomers (Co_4Si_2).[187] Although the Co_4Si_2 isomers are not analogous to Co_4P_2, a comparative study under the conditions used in Co_4P_2 studies [170] showed that Co_4Si_2 is less efficient (lower maximum TON) and undergoes slow hydrolysis to more inactive forms during water oxidation. Following this work, Car et al. reported the analog compound to Co_4P_2, $[Co_4(H_2O)_2(SiW_9O_{34})_2]^{12-}{}_2$, and investigated its performance as visible-light-driven WOC at pH 5.8.[168] The Si-analog is an active WOC, although much less efficient than the original Co_4P_2. In 2014, Lv et al. synthesized a new vanadate (V)-centered POM $[Co_4(H_2O)_2(VW_9O_{34})_2]^{10-}$ (Co_4V_2), which is isostructural to Co_4P_2.[188] Under photo-induced water oxidation, Co_4V_2 performs exceptionally fast (up to $\approx 10^3$ s^{-1} TOF) with final O_2 yields of ~68%, twice as high as that of Co_4P_2. The stability of Co_4V_2 has also been subject to debate.[189,19051,52] Recent vanadium NMR solution studies on the NMR/$Co^{II}aq/CoO_x$ system describe a complex speciation behavior in solution, making the identification of the various equilibrating aqueous active catalysts in the system is a challenging task.[191] Despite several advances, the large catalytic difference between Co_4V_2 and Co_4P_2 called for examining the significance of substituting phosphorus centers in Co_4P_2 with vanadium. A thorough DFT study on the OER mechanism for Co_4P_2 suggested that the O–O bond formation takes place from a Co^{3+}-oxyl radical through the WNA attack pathway.[192] The computation of the reaction mechanism with Co_4V_2 showed a higher oxidation potential for the first proton coupled electron transfer (PCET) event and a reduction in the activation energy for the WNA pathway. The authors ascribed both effects to the decrease in the molecular orbital energies due to the orbital coupling between vanadium and cobalt atoms. In 2018, evidence for the significance of the vanadium centers to catalysis, predicted by theory, was found from soft X-ray absorption (XAS) and resonant inelastic X-ray scattering (RIXS).[193] The results revealed that Co_4V_2 possesses a smaller ligand field within the tetra-cobalt core and a cobalt-to-vanadium charge transfer band, supporting previous theoretical predictions. Interestingly, Soriano-López et al. recently reported that it is possible to dope molybdenum into the Co_4P_2 structure synthesizing a mixed Mo and W ($Co_4Mo_xW_y$) analog.[194] Doping the W framework of Co_4P_2 with Mo leads to the electrochemical oxidation of water at a low onset potential, and with no catalyst degradation while reducing the overpotential of the oxygen evolution (η_{O2}) reaction by 188 mV compared with the pure tungsten framework.

Goberna-Ferrón et al. discovered the catalytic activity of the high-nuclearity Co-based POM $[Co_9(H_2O)_6(OH)_3(HPO_4)_2(PW_9O_{34})_3]^{16-}$ (Co_9).[195] Its molecular structure (Inset of Figure 15 (a)) contains three triads of edge-sharing $Co^{II}O_6$ octahedra supported by three tri-vacant Keggin-type $[PW_9O_{34}]^{9-}$ units. The triads are interconnected through three OH^- and two $HPO4^{2-}$ bridges. Six of the Co ions complete their coordination sphere with terminal water molecules. Co_9 is as an effective WOC using NaClO as the oxidant; when the ratio of catalyst to NaClO is 1:100, the reaction rate with Co_9 is at least 8 times faster than that with Co_4P_2 at pH 8. The catalytic process can be maintained for several days without fatigue or decomposition. The homogeneous character of Co_9 during the oxygen evolution reaction has been well established from postreaction characterization. In addition, small-angle X-ray scattering experiments were carried out to investigate, in detail, the speciation under catalytic working conditions, confirming the remarkable stability of Co_9 in water oxidation conditions.[196] As an electrocatalyst in homogeneous conditions, decomposition reactions that yield a thin CoO_x film on the anode can be easily avoided by the addition of chelating agents. After the reaction cycles, Co_9 can be recovered from solution by recrystallization with additional alkali-metal cations or by slow evaporation of the reaction medium. The Cs^+ insoluble salt of Co_9 can be blended into a carbon paste electrode to yield a robust catalytic process in the pH range from 1 − 8.[197] Co_9-modified electrodes exhibited exceptional stability during bulk water electrolysis, where the current remains constant for at least 8 h. Moreover, Cs-Co_9 electrodes are more active than Co_3O_4 electrodes under the same conditions, yielding 2 orders of magnitude larger current densities for equimolar amounts of Co content (Figure 15 a). The most remarkable feature of Cs-Co_9 is its stability at a low pH values (<1.5), where CoO_x is unstable. This is important considering that acidic solutions appear to be preferred as media to carry out water electrolysis since hydrogen production is much easier at lower pH, where the proton (as reagent) concentration is higher. In this context, the Ba^+ salt of Co_9 showed a significantly better electrocatalytic performance in 1M H_2SO_4 than the Cs^+ salt, with onset

View Article Online
DOI: 10.1039/D0EE03407J

potentials as low as $\eta = 88$ mV (vs. 196 mV) and higher current densities due to better electron transfer kinetics.[198] Moreover, the Ba-Co_9 outperforms the state-of-the-art IrO_2 catalyst even at pH < 1, with an η_{O2} of 189 mV at 1 $mA.cm^{-2}$. Notably, the authors observed an enhancement of the catalytic stability in acidic medium by using a carbon-paste conducting support with a hydrocarbon binder, which provides a hydrophobic environment. Very recently, the same authors reported a complete series of catalytic studies with multiple Co-based POMs, including Co_9, following the same working electrode strategy.[199] Composition-structure-activity relationships indicated that i) only those species containing P(V) as heteroatoms appeared to be stable; ii) the Keggin-derivatives exhibit faster performance than their Dawson-Wells counterparts; and iii) among them, catalytic activity is favored by high Co nuclearity and overall total charge. Since carbon paste is limited by its poor mechanical and redox stability, the authors recently turned their interest in conducting organic polymers, incorporating the Co_9 into a polypyrrole matrix to obtain organic-inorganic hybrid anodes.[200] These electrodes sustain robust electrocatalytic water oxidation in neutral media, offering very good processability. It is remarkable that less than 6% POM content in a polypyrrole film multiplies OER currents by one order of magnitude, reducing the required overpotentials by approximately 200 mV. During these experiments, however, roughly 65% efficiency towards O_2 evolution was found, suggesting the occurrence of competing oxidations. It is also noteworthy that a Ba-Co_9/lead composite has been investigated recently as anode for OER during zinc electrowinning.[201]

The OER is the most common anode or counter reaction in the electrowinning of metals from acidic electrolytes. Zn electrowinning consumes a lot of electrical energy due to the high η_{O2}, so even a modest decrease in the η_{O2} would be beneficial for industry to save energy. The η_{O2} of the Ba-Co_9/lead composite decreased by about 137 and 40 mV compared to pure Pb foil and Pb-0.75Ag alloy (commonly used in the hydrometallurgical industry), respectively. Therefore, the Ba-Co_9/Pb composite could be a suitable substitute additive for Ag, with a strong potential industrial application. Recently, the Cs^+ salt of Co_9 was tested as heterogeneous oxygen evolution catalyst in light-induced experiments, using $Ru(bpy)_3^{2+}$as the PS and $S_2O_8^{2-}$ as the SA in neutral pH.[202] Post-catalytic assays indicated that the Cs-Co_9 is transformed into the corresponding $[Ru(bpy)_3]^{2+}$ salt upon cesium loss. Remarkably, analogous photoactivated oxygen evolution experiments starting with a $[Ru(bpy)_3]^{2+}$ salt of Co_9 demonstrated much higher efficiency and kinetics, with maximum TON and TOF of 27.3 and 19.1 h^{-1} respectively (14.2 and 10.8 h^{-1} for Cs-Co_9), affording chemical yields close to 50% (10% for Cs-Co_9). The origin of this improved performance is the closer cation-anion (PS/catalyst) interaction in the solid state. This is beneficial for the electron transfer event, and for the long-term stability of the PS. Han et al. reported a series of high-nuclearity Co-based POM WOCs, $([Co_4(OH)_3(PO_4)]_4(XW_9O_{34})_4)^{n-}$ (X = Si, Ge, P, As; n= 32, 28) ($Co_{16}X_4$).[203] These Co-POMs contain a high-nuclearity Co–Pi cluster ($Co_{16}(PO_4)_4(OH)_{12}$) encapsulated by four $[XW_9O_{34}]^{n-}$ units. The ($Co_4(PO_4)_4(OH)_{12}$) core contains a Co_4O_4 cubane structurally analogous to the $[Mn_3CaO_4]$ core of the oxygen-evolving complex (OEC) in photosystem II (PSII). The trend in photocatalytic activity was $Co_{16}Ge_4 > Co_{16}As_4 > Co_{16}Si_4 \geq Co_{16}P_4$. The values for $Co_{16}Ge_4$ were 31% O_2 yield, TON = 38.75 and initial TOF in the first 300 s of 0.105 s^{-1}. Furthermore, the structural integrity of the POMs under photocatalytic conditions was confirmed by recrystallization, laser flash photolysis, dynamic light scattering (DLS), phosphorous-31 NMR, UV−vis, POM extraction, and inductively coupled plasma mass spectrometry (ICP-MS). Recently, the photocatalytic activity towards water oxidation of $Co_{16}P_4$ has been compared to that of Co_9 and another Co-based POM, $[Co_6(H_2O)_{30}(Co_9Cl_2(OH)_3(H_2O)_9(SiW_8O_{31})_3)]^{5-}$ (Co_{15}).[204] The WOC performance followed the trend Co15 ~ Co16 > Co9, in agreement with flash photolysis results, indicating that fast multi-hole accumulation is a prelude to fast oxygen evolution under the conditions explored. The resident state of the Co-POMs after O_2 evolution displays XANES spectra that are consistent with a photo-induced oxidation of the cobalt centers while retaining the POM features, thus ruling out structural leaching of Co^{II} ions and evolution to CoO_x colloids.

Another high-nuclearity Co-based WOC that resembles the OEC in PSII is the double $Co^{II}{}_4O_3$ core POM $[(A\text{-}\alpha\text{-}SiW_9O_{34})_2Co_8(OH)_6(H_2O)_2(CO_3)_3]^{16-}$.[205] This octo-nuclear cobalt complex contains two cubical $Co^{II}{}_4O_3$ cores, with two of these Co atoms coordinated to terminal aquo ligands. The two

View Article Online
DOI: 10.1039/D0EE03407J

$Co^{II}_4O_3$ cores are located in two trivacant $[SiW_9O_{34}]^{10-}$ ligands and are connected by three CO_3^{2-} anions. This catalyst exhibited excellent photochemical water oxidation activity, reaching a TON of 1436, currently the highest amongst bioinspired catalysts with a cubical core, and a high initial TOF of 10 s^{-1}. Zhang et al. combined the well-established bpy ligand and Co metal ion with stable Keggin-type Mo-POMs to design a robust organic-inorganic hybrid molecular WOC, $([(Co^{II}bpy)_2(PMo_8^{VI}Mo_4^{V}O_{40})]_3[(Co^{II}bpy)(PMo_8^{VI}Mo_4^{V}O_{40})])^{8-}$.[206] This compound was shown to be an efficient visible light-driven catalyst for water oxidation. Its stability was demonstrated by DLS, POM extraction, UV-vis and FT-IR. Moreover, control experiments demonstrated that POM anions can enhance the WOC activity of bipyridine-substituted cobalt complexes. Chen et al. synthetized the first POM with a cobalt–arsenic core, $[(Co^{II}_7As^{III}_6O_9(OH)_6)(A\text{-}\alpha\text{-}SiW_9O_{34})_2]^{12-}$, which contains two $[SiW_9O_{34}]^{10-}$ fragments encapsulating a hepta-nuclear cobalt-arsenic $(Co^{II}_7As^{III}_6O_9(OH)_6)$ core that show a ‘‘fused’’ double-quasi-cubane-type topology.[207] The unique $Co^{II}_7O_6$ core provides another example of bio-mimetic structural model that catalyzes water oxidation. Very recently, Gong et al. reported a new sandwich tungstobismuthate WOC, $(Hdamp)_2[(Na_4(H_2O)_9Co_2(H_2O)_6WO_3)_2(BiW_8O_{30})_2]$ (dmap = N-(4-pyridyl)dimethylamine), which is an efficient catalyst for water oxidation under visible light irradiation at pH 9 (TON of 205.5 and O_2 yield of 32.88%).[208] The basic structural unit can be described as two $(BiW_8O_{30})^{9-}$ POM units sandwiched by an unusual 14-nucleus mixed-metal cluster $(Na_4(H_2O)_9Co_2(H_2O)_6WO_3)_2$. Interestingly, the sandwich units themselves are directly interconnected to form independent chains and layers, forming extended 2D layers linked to each other by H-bonds and supramolecular interactions between the 4-dimethylaminopyridine (dmap) groups and surface oxygen atoms of the POM units. The stability of this catalyst was confirmed through UV−vis, DLS, catalyst aging, and POM toluene extraction experiments.

It is important to note that high cobalt nuclearity is not a requirement for POM-WOC design. In 2012, Tanaka et al. reported two POMs containing mono- and di-Co^{III} catalyst cores, $[CoMo_6O_{24}H_6]^{3-}$ (Co-Mo) and $[Co_2Mo_{10}O_{38}H_4]^{6-}$($Co_2Mo$), as the first examples of low nuclearity Co-

View Article Online
DOI: 10.1039/D0EE03407J

based POM WOCs.[209] Photo-induced water oxidation at pH=8 revealed that both compounds possess higher activity than Co_4P_2 under the same experimental conditions, thus demonstrating that neither a critical POM size nor multi-site metal cores are mandatory for catalytic activity. The POM charges, normalized to the number of Co centers, are similar to each other (−3, −3, and −2.5 for Co-Mo, Co_2-Mo and Co_4P_2, respectively). Such an electronic factor may affect the O_2 evolving activity of cobalt centers. Moreover, the authors demonstrate that Mo-based POMs instead of W-based POMs can also serve as catalysts for O_2 evolution. Evangelisti et al. investigated sandwich-type $[(Co(H_2O)_3)_2(CoBi_2W_{19}O_{66}(OH)_4)]^{10-}$, with two identical lacunary (BiW_9O_{33}) units connected via two disordered ($WO_2|CoO_2$) internal groups and two terminal ($Co(H_2O)_3$) moieties forming a tetranuclear metal core.[210] This POM exhibited high photocatalytic activity with maximum TON of 21 and 97% oxygen yield. However, the isostructural $[Co_{2.5}(H_2O)_6(Bi_2W_{19.5}O_{66}(OH)_4)]^{8-}$, that displays the same disorder pattern on the internal sites together with a 3:1 Co:W ratio on the terminal core positions, turned out to be inactive for water oxidation. The subtle difference in the Co occupancy of the terminal positions had a decisive effect on WOC activity, suggesting that only terminal core sites are essential for WOC activity and, therefore, that high nuclearity core clusters are not essential for the catalytic activity. A mono-nuclear Co^{II}-substituted POM, the Keggin $[Co^{III}Co^{II}(H_2O)W_{11}O_{39}]^{7-}$, was investigated for visible-light driven water oxidation.[211] The authors proposed that the $Co^{III}O_4$ tetrahedra, located in the center of the Keggin polyanion, plays an important role in maintaining the integrity of the structure, while the peripheral $Co^{II}O_6$ octahedral cluster is the active site for water oxidation. Notably, this Keggin POM catalyst was later applied to efficient hydrogen evolution under visible light irradiation.[212] Another mono-nuclear Co^{II}-substituted POM, $[Co(H_2O)_2(\gamma\text{-}SiW_{10}O_{35})_2]^{10-}$, was investigated as a light-driven WOC acquiring high TON of 313, a TOF of 3.2 s^{-1}, and Φ of 27% for O_2 evolution at pH 9.0.[213] Structural analogs incorporating Ni and Mn resulted in little water oxidation activity, suggesting that the Co center is the active site. In addition, the catalytic activity was better than that of the $Co^{III}Co^{II}$ Keggin POM discussed previously and comparable to that of Co_4P_2 under the same conditions. The hydrolytic stability of this mono-nuclear Co-POM was

View Article Online
DOI: 10.1039/D0EE03407J

confirmed by UV/Vis, linear sweep voltammetry measurements of the catalyst and by cathodic adsorption stripping analysis.

4.1.3 Manganese-based POM WOCs

In natural photosynthesis, the WOC is a tetranuclear manganese cluster (Mn_3CaO_4) stabilized by amino acids, water molecules and counter ions. However, there are only a few examples of Mn-POMs reported. This lack Mn examples is not exclusive to POMs,[214] and even if one considers heterogeneous catalysts, Mn oxide is much less active than the corresponding Co or Ni analogs.[215] Still, the use of Mn is attractive because it is earth-abundant and relatively nontoxic when compared with the other more active metal-based catalysts.

Al-Oweini et al. reported the first manganese tungstate WOC, $[Mn^{III}_3Mn^{IV}O_3(CH_3COO)_3(SiW_9O_{34})]^6$, a mixed-valent ($Mn_4$) core, which is stabilized by a hybrid set of ligands, including an inorganic POM platform and carboxylate bridges.[216] The interplay of organic and inorganic residues provides a coordination environment with both stability and flexibility to assist stepwise one-electron oxidation of the catalytic core and to access high-valent Mn states that are responsible for water oxidation. Photo-induced water oxidation at pH 5 exhibited a TOF per Mn center of 0.71×10^{-3} s^{-1}, TON up to 5.2, and a Φ of 1.7%. Schwarz et al. designed a Mn-based POM, $[Mn_4V_4O_{17}(OAc)_3]^{3-}$, based on a $[Mn_4O_4]^{6+}$ cubane core stabilized by a $[V_4O_{13}]^{6-}$ ligand, that interacts with three Mn centers of the cubane, and three acetate ligands.[217] Under visible-light irradiation, the cluster shows high WOC activity (TON ˜ 1150, TOF ˜ 1.75 s^{-1}). Furthermore, the cluster stability and reactivity were checked by electrochemical, mass spectrometric and spectroscopic studies.

Recently, the photochemical and electrochemical water oxidation activity of the sandwiched dimer $[Mn_3(H_2O)_3(SbW_9O_{33})_2]^{12-}$ was reported.[218] The authors demonstrated that heteroatoms in the POM play important role for the water oxidation; compared to its $[PW_9O_{34}]^{9-}$ and $[AsW_9O_{33}]^{9-}$ analogs, the Mn_3-POM based on a Sb heteroatom has the best water oxidation activity. Multiple experiments including UV−vis, catalyst aging, POM extraction, electrochemical and capillary electrophoretic experiments confirmed that the catalyst is a homogeneous molecular catalyst. The

DOI: 10.1039/D0EE03407J

search for Mn-POMs which could exhibit WOC activity called for examining the Mn-analog of the well-studied Co_4P_2, $Mn_4(H_2O)_2(PW_9O_{34})_2]^{10-}$.[219] Electrochemical water oxidation experiments showed initial activities comparable to those of the Co counterpart, although current density decreased very rapidly to become negligible just after 30 min, with the appearance of an inactive MnO_x layer on the electrode. Another high nuclearity Mn-POM, the mixed-valent $[Mn^{III}_{10}Mn^{II}_6O_6(OH)_6(PO_4)_4(A\text{-}a\text{-}SiW_9O_{34})_4]^{28-}$ polyanion supported on graphene (Mn_{16}@graphene),[220] was tested by using rotating ring-disk voltammetry (Figure 15 b) showing comparable TOF values to the Ru_4Si_2-graphene system[164] at neutral pH. As shown in the inset of Figure 15 (b), the structure of this Mn-POM polyanion comprises a central ($Mn^{II}_4O_4$) cubane, capped by 4($Mn_3(SiW_9)$) Keggin units. The overall assembly is connected to each other in a tetrahedral fashion by four phosphate (PO_4) linkers. This Mn-POM has been deposited on an ITO-coated glass electrode and on a glass carbon electrode by a layer-by-layer assembly method for electrocatalytic water oxidation.[221] Very recently, Teillout et al. synthetized and characterized the Mn-POM $[(Mn(H_2O)_3)_2(H_2W_{12}O_{42})]^{6-}$, which is an extended 2-D network consisting of $[H_2W_{12}O_{42}]^{10-}$ moieties linked together by Mn^{2+}, K^+ and Na^+ ions.[222] This complex undergoes multiple electron-transfer processes that lead to the electro-generation of manganese high-oxidation-state species that catalyze water oxidation.

4.1.4 Nickel-based POM WOCs

The first Ni-containing POM WOC, $[Ni_5(OH)_6(OH_2)_3(SiW_9O_{33})_2]^{12-}$($Ni_5Si_2$) was reported by Zhu et al. in 2012.[223] This Ni-POM was constructed from an *open Wells–Dawson* $[Si_2W_{18}O_{66}]^{16-}$ fragment (built up from two $[SiW_9O_{34}]^{10-}$ keggin-type subunits) embedded by a large $[Ni_5(OH)_6(OH_2)_3]^{4+}$ unit in the central cavity. Ni_5Si_2 exhibited efficient chemical and photochemical water oxidation activity. Moreover, light-driven water oxidation revealed the formation of a Ni_5Si_2–PS complex which exists in the form of NPs that remain molecular and do not decompose to nickel hydroxide particles, and which are more active for water oxidation than freely diffusing Ni_5Si_2. Three polynuclear nickel clusters, $[Ni_{12}(OH)_9(CO_3)_3(PO_4)(SiW_9O_{34})_3]^{24-}$,

$[Ni_{13}(H_2O)_3(OH)_9(PO_4)_4(SiW_9O_{34})_3]^{25-}$; and $[Ni_{25}(H_2O)_2OH)_{18}(CO_3)_2(PO_4)_6(SiW_9O_{34})_6]^{50-}$ were reported as structurally stable WOCs under photochemical conditions (Figure 16).[224] All three compounds contain (Ni_3O_3) quasi-cubane or (Ni_4O_4) cubane units, which are similar to the [Mn_3CaO_4] core of the OEC in PSII. The trend in efficiency was $Ni_{12} < Ni_{13} < Ni_{25}$ (TON = 204.5), suggesting activity could be related to the Ni nuclearity.

Following this work, Yu et al. reported the photocatalytic activity towards water oxidation of a tetra-Ni-based POM, $[(SiNi_2W_{10}O_{36}(OH)_2(H_2O))_4]^{24-}$.[225] This Ni-POM can be seen as two lacunary $[SiW^{10}O^{37}]^{10-}$ Keggin units where each unit accommodates two Ni^{2+} ions linked together by two bridging -OH groups. The cluster shows higher WOC activity than the previously reported Ni-POMs, according to the O_2 yield (27.2%), high TON (335) and TOF of 1.7 s^{-1}. Singh et al. recently reported a hybrid POM-supported Ni^{II} coordination complex, $[(Ni^{II}(bpy)_2(H_2O))(HCo^{II}W^{VI}{}_{12}O40)]_2{}^{3-}$, containing the Keggin anion $(H(Co^{II}W_{12}O_{40})^{5-}$ as the inorganic unit and 2,2′-bpy as the organic unit linked together with a Ni^{II} metal ion that acts as the catalytic center.[226] This catalyst was found to be highly stable and robust under electrochemical water oxidation conditions at pH 7, exhibiting a moderate η value of 475.6 mV with a high TOF of 18.49 s^{-1}. However, the crystal structure of the compound was not investigated completely and hence more studies need to be conducted in order to tune the structure for real world applications.

4.1.5 Other POM WOCs

Several other POMs WOC have also been investigated. For instance, Cao et al. reported the first Ir-POM WOC, $[(IrCl_4)KP_2W_{20}O_{72}]^{14-}$.[227] Its water oxidation activity was determined at pH 7.2 using $[Ru(bpy)_3]^{3+}$ via electrochemical methods. Stability studies of the catalyst indicated a dissociation in aqueous solution into the $[IrCl_4(H_2O)_2]^-$ unit and the $[KP_2W_{20}O_{72}]^{13-}$ ligand (based on 2 $PW_9O_{34}]^{9-}$ linked by two $[W^{VI}O_2]^{2+}$) However, the oxidation of water proceeds two orders of magnitude faster than the hydrolytic decomposition. Further water oxidation studies of the dissociation products indicated that both $[IrCl_4(H_2O)_2]^-$ and $IrCl_3$ show similar activities, while the ligand $[KP_2W_{20}O_{72}]^{13-}$ is inactive to water oxidation, implying that the intact catalyst could well

View Article Online
DOI: 10.1039/D0EE03407J

catalyze water oxidation. However, this study was inconclusive regarding the formation of catalytically active IrO_2 NPs. Interestingly, a heteropolyoxoniobate compound, $[(Nb_2(O)_2(H_2O)_2)(SiNb_{12}O_{40})]^{10-}$, was reported as a water oxidation photocatalyst.[228] The structure is composed of Nb-Keggin clusters linked into infinite 1D chains by dinuclear $(Nb_2(O)_2(H_2O)_2)$ moieties that contain a water molecule directly coordinated to each of the two bridging Nb active sites. Initial studies also demonstrated that this Nb−POM can be combined with a hydrogen-evolving catalyst (NiO), forming a heterogeneous system for the splitting of water into oxygen and hydrogen, albeit at relatively low TON.

Three new Ru dye-sensitized Mo-POM–$[Ru(phen)_3]$ (phen = tris(1,10- phenanthroline)) hybrids were reported as active WOCs under photocatalytic conditions. $[Ru(phen)_3CH_3OH][Mo_6O_{19}]$, $[Ru(phen)_3][(C_2H_8N_2)_2(C_3H_7NO)][Mo_5S_2O_{23}]$, and $[Ru(phen)_3CH_3CN]_2[Mo_8O_{26}]$ were made of anionic Mo-POM clusters, charge-balancing $[Ru(phen)_3]^{2+}$ PS unit and solvent molecules.[229] The trend in catalytic efficiency was determined to increase with increasing Mo active sites. Impressively, the Ag^I-substituted Keggin POM $[H_3Ag^IPW_{11}O_{39}]^{3-}$ can be oxidized by $S_2O_8^{2-}$ in aqueous solutions to generate $[H_3Ag^{II}(H_2O)PW_{11}O_{39}]^{2-}$ and a small amount of $[H_3Ag^{III}OPW_{11}O_{39}]^{3-}$, simultaneously evolving O_2 with higher efficiency than simple Ag salts.[230] This work illustrated that the $[PW_{11}O_{39}]^{7-}$ ligand plays important roles in the transmission of both electrons and protons, and in the improvement of the redox performance of silver ions. In 2019, another Ag-based POM was reported by Chaojie Ciu et al.,[231] $H_{17}[Ag_9(AgH_8W_{11}O_{44})_2(bpy)_9]$, where $[AgH^8W^{11}O^{44}]^{13-}$ polyoxoanions are connected by 1D chains formed by Ag(I) cations ligated by bpy ligands to produce a 3D Ag(I)-containing POM-based MOF. This hybrid material exhibited photocatalytic O_2 production with an average rate of 964 μmol.g^{-1} in the first 10 minutes.

A POM WOC containing only vanadium atoms as metal centers, $[(V^{IV}{}_5V^{V}{}_1)O_7(OCH_3)_{12}]^-$, was reported in 2014.[232] The mixed-valence cluster is formally derived from the Lindqvist structure $[M_9O_{19}]^{n-}$ substituting the 12 μ-bridged oxo ligands by methoxo ligands. Under photoinduced

View Article Online
DOI: 10.1039/D0EE03407J

conditions, the Φ of 40% was comparable with the values obtained using one of the most studied CoIII) cubane-type species [233] in similar conditions. The first Fe-POM WOC reported, $[Fe_{11}(H_2O)_{14}(OH)_2(W_3O_{10})_2(SbW_9O_{33})_6]^{27-}$ (Fe11) [234,235] features six tri-lacunary Keggin $[SbW_9O_{33}]^{9-}$ ligands gathered together by a $(Fe_{11}(H_2O)_{14}(OH)_2(W_3O_{10})_2)^{27+}$ core. Under photochemical water oxidation, the TON reached 1815 with an initial TOF of 6.3 s^{-1}. Recently, Hu et al. implemented this catalyst into a three-component photocatalytic water oxidation system with $BiVO_4$ as light-harvesting material and $NaIO_3$ as SA. The system produced an O_2 yield of 19.1% sustaining initial TOF of 173 h^{-1} with a Φ of 25.3% in acidic medium.[236] More recently, a well-known giant $Mo_{72}Fe_{30}$ POM cluster, $Mo_{72}Fe_{30}O_{252}(CH_3COO)_{12}[Mo_2O_7(H_2O)]_2[H_2Mo_2O_8(H_2O)](H_2O)_{91}$, has been explored as an efficient and stable WOC in the presence of light at pH 9 exhibiting TON of 13.99 with TOF of 3 min^{-1}.[237] In a different strategy, Fe(III)-substituted anions, $[PW_{11}O_{39}Fe]^{4-}–O^{-}$, were reported as oxo-donor ligands for hematite (α-Fe_2O_3) cores (Figure 17 (a)), giving stable, water-soluble catalysts for water oxidation using visible light. The authors identified a new mechanism of freely diffusing fragments of solid-state metal oxide taking part in multi-electron oxidation of water.[238,239] Yu et al. reported a Cu-POM WOC, the sandwich-type $[Cu_5(OH)_4(H_2O)_2(SiW_9O_{33})_2]^{10-}$, which was able to catalyze photochemical water oxidation with an O_2 yield of 12.3% and a TON of 61.[240] Very recently, another sandwich-type Cu-POM cluster, $[Cu_3(H_2O)_3(SbW_9O_{33})_2]^{12-}$ was shown to catalyze water oxidation at a neutral pH without decomposition under homogeneous electrochemical conditions.[241] Interestingly, $[Cu_5(OH)_4(H_2O)_2(SiW_9O_{33})_2]^{10-}$ showed negligible activity under the same conditions.

The molecular nature of POMs represent a unique opportunity for the development of WOCs. Furthermore, investigations have shown that the stability of the catalysts must be taken into consideration, studying the speciation and the mechanism of catalysis with POMs is essential for garnering fundamentally useful insights into catalysis by POM-based systems.

4.2 Oxygen Reduction

View Article Online
DOI: 10.1039/D0EE03407J

The reduction of molecular oxygen occurs inside fuel cells and metal-air batteries. The ORR follows very slow kinetics and has a very high overpotential. Therefore, significant research effort is devoted to improving this reaction. The reduction of molecular oxygen can occur through two pathways. First is the four-electron pathway, leading to the formation of water and second is the two-electron pathway in which the product is hydrogen peroxide (H_2O_2). POMs are normally used as active centers for a reduction supported over a conducting substrate to transport the electrons and accelerate the reaction kinetics.

4.2.1 POMs as Catalysts for ORR

In recent years, many POM compounds incorporating transition metal clusters have been shown to serve as robust catalysts, especially in the water oxidation field (section 4.1). However, relatively few reports have been devoted to the ORR catalytic activity of transition metal-substituted POMs. In 2015, Rousseau et al. reported a nanocomposite based on the heterometallic complex $[((PW_9O_{34})Co_3(OH)(H_2O)_2[O_3PC(O)(C_9H_{13}N_2[Zn(H_2O)_3])PO_3])_2Co]^{12-}$ ($Co_7(AlePyZn)_2$) (Inset of Figure 17 (b)) and cost-effective VC XC-72 as ORR electrocatalyst.[242] This heterometallic POM complex contains a heptanuclear Co^{II} core sandwiched by two $[PW_9O_{34}]^{9-}$ units and connected to two $[O_3PC(O)(C_3H_6NHCH_2(C_5NH_4))PO_3]^{5-}$ (AlePy) ligands linked to two Zn^{II} cations. Both Zn^{II} ions complete their coordination spheres with one oxygen atom of the POM and three terminal water molecules. The Co_7(AlePyZn)/C composite showed high activity for the reduction of O_2 (Figure 17 (b)), better tolerance to methanol crossover, which is important for practical applications of direct methanol fuel cells (DMFCs), and superior durability compared to commercial Pt/C. Recently, the same group reported a series of POM-based composites as efficient cathode materials for the ORR, in neutral or basic media, via a four-electron mechanism with high durability.[243] Similarly to $Co_7(AlePyZn)_2$, the reported POM structures consist of a M_7 (M = Co or Ni) core encapsulated between two $[PW_9O_{34}]^{9-}$ units and structured by two alendronate (Ale, $(H_2O_3PC(OH)(C_3H_6NH_2)PO_3)^{2-}$) ligands. The activity of this POM systems was optimized by the

View Article Online
DOI: 10.1039/D0EE03407J

judicious choice of 3d metals incorporated in the ($(PW_9)_2M_7$) (M = Co, Ni) POM core, the POM counter ions and the support (thermalized triazine-based frameworks (TTFs), fluorine-doped TTF (TTF-F), rGO, or carbon VC XC-72). In particular, the overpotential required to drive the ORR for the composite associating the ($(PW_9)_2Ni_7$) POM, $[Cu(ethylenediamine)_2]^{2+}$ counter-cations, and the highly conductive and ORR active TTF-F carbonaceous material is very close to that of commercial Pt/C. The good ORR electrocatalytic activity can be attributed to two synergistic effects due to the binary combination of the Cu and Ni centers and the strong interaction between the POM molecules and the porous and highly conducting TTF-F framework. However, the mechanisms behind these synergies are still unclear and require further studies.

The well-known WOC $[Co_4(H_2O)_2(\alpha\text{-}PW_9O_{34})_2]^{10-}$ (Co_4P_2) was tested as an ORR electrocatalyst in 2018.[244] Co_4P_2 was immobilized onto different carbon nanomaterials (SWCNT, graphene flakes (GF), N-doped CNTs, and N-doped few layer graphene (N-FLG)). In alkaline media, all nanocomposites exhibited superior overall electrocatalytic activity when compared to the corresponding carbon materials with onset potentials (0.77−0.90 V vs RHE) comparable to commercial Pt/C (0.91 V vs RHE). In particular, Co_4P_2@N-CNT presented greater diffusion-limiting current density (1.8 times) than Pt/C. Moreover, these nanocomposites showed excellent tolerance to methanol with no significant changes in current density, in contrast to Pt/C (decrease of ≈59% after methanol addition), and good long-term electrochemical stability with current retentions between 75 and 84%. The integrity of the Co_4P_2 POM structure after the long-term stability tests was confirmed by XPS analysis.

Simple bare POM structures have also been reported as ORR electrocatalysts when combined with carbon-based materials. In 2014, a negatively charged Pressler-type POM, $[NaP_5W_{30}O_{110}]^{14-}$, GO and poly(ethyleneimine) (PEI) were constructed into $(PEI/POM{-}rGO)_n$ nanocomposite multilayer with protonated PEI via LbL self-assembly route combined with post-photoreduction method.[245] The results obtained proved that the POM played a main role in ORR electrocatalysis while rGO promoted the advance of the onset potential, E_{onset}, for ORR to ~80 mV. Nunes et al.

View Article Online
DOI: 10.1039/D0EE03407J

prepared various nanocomposites based on vanadium-substituted phosphomolybdate, $[PMo_{11}VO_{40}]^{4-}$ ($PMo_{11}V$), incorporated into different carbon-based materials.[246] All nanocomposites showed ORR electrocatalytic activity in acidic medium, with a strong dependency between the electrocatalytic ORR performance and the carbon material used as support. The E_{onset} shifted to less negative values in the order $PMo_{11}V$@carbon-black < $PMo_{11}V$@SWCNT < $PMo_{11}V$@graphene; for $PMo_{11}V$@graphene, the most promising composite, it was measured at $E_{onset} = 0.18$ V vs. RHE.

Recently, a lacunary Keggin POM, $[PW_{11}O_{39}]^{7-}$, was covalently linked with 3D ordered macroporous graphitic carbon nitride (3DOM g-C_3N_4) through an organic linker strategy.[247] This covalent combination selectively promoted the two-electron O_2 reduction due to the enhanced O_2 adsorption of 3DOM g-C_3N_4-POM compared to its counterparts. The performance of the described POM ORR catalysts is summarized in Table 2.

4.2.2 POMs as Co-catalysts for ORR

POMs have also been combined with other materials to develop POM-based composites with improved catalytic properties for ORR as result of the synergetic effects between all components. Typically, Pt-based materials are state-of-the-art catalysts for ORR despite their high cost. However, due to the scarcity and high cost of noble metals, their integration with other sustainable and available materials such as POMs is an attractive way to optimize their properties and minimize their consumption. Additionally, using M^0 nanostructures (i.e. zero-dimensional) increases the overall surface-to-volume ratio and hence reduces the metal loading. This is why great efforts have been focused on decreasing the Pt loading or replacing the electrocatalysts with non-Pt based materials.

Hsu-Yao et al. synthetized 3-4 nm sized POM-stabilized Pt^0 NPs using electrochemically reduced POM anions, $SiW_{12}O_{40}^{4-}$ and $H_2W_{12}O_{40}^{6-}$, as reductant and protecting/stabilizing ligands.[248] Compared to the commercial Pt black, both the POM-stabilized Pt^0 NPs showed higher ORR, with $Pt^0@W_{12}O_{40}$ NPs having better performance ($E_{1/2}$ showing a 30 mV positive shift while that of the $Pt^0@Si_{12}O_{40}$ being 17 mV as compared to that of the Pt black). The observed activity enhancements may be related to the generally weakened reactant–metal surface binding as implied by cyclic

View Article Online
DOI: 10.1039/D0EE03407J

voltammetry (CV) analysis. In a different strategy, Renzi et al. recently evaluated the ORR catalytic activity of Pt^0 NPs mixed with insoluble $Cs_3HPMo_{11}VO_{40}$[249,250] and $Cs_3H_2PMo_{10}V_2O_{40}$[251] POMs. The Pt amount was reduced through the use of POMs as co-catalytic supports that are able to: i) enhance catalyst dispersion and limit the aggregation during fuel cell operation, induced by the mesoporous features of POM that allow the embedding of Pt inside the micro-mesopores; and ii) enhance the kinetics of the ORR redox process, owing to the high surface acidity of POMs and consequent high proton mobility. This strategy allowed decreased Pt loading while maintaining the electrocatalytic performance towards ORR.

Xin et al. fabricated stable Au^0 NPs/POM modified glassy carbon electrodes (GCE) using LbL assembly. PPDA-stabilized Au^0 NPs were synthetized first using $NaBH_4$ as reducing agent.[252] Next, GC/(POM/Au-NP)$_n$ LbL hybrid films were prepared by the sequential deposition PDDA-stabilized Au^0 NPs and POMs on GCE via the electrostatic forces between the negatively charged POM and positively charged PDDA. The authors compared the electrocatalytic behavior in terms of half-wave potential for the ORR ($E_{1/2}$) of LbL monolayers built using W-, Ru-, and Co-substituted Keggin POMs. The trend in catalytic activity was $PCoW_{11}O_{39}^{5-} > PRuW_{11}O_{39}^{5-} > PW_{12}O_{40}^{3-}$, where POM co-catalysts containing more labile M–O bonds (e.g. Co-substituted) were better ORR co-catalysts. In the same year, Bao et al. chose a wheel-shaped V^V–V^{IV} mixed-valence tungstovanadate, $[P_8W_{48}O_{184}(V_4^V V_2^{IV}O_{12}(H_2O)_2)_2]^{32-}$ (V_{12}), that acts as both reducing (V^{IV} reduced centers in V_{12}) and capping ligand to synthetize 30 nm POM-stabilized Au^0 spherical NPs (Au^0@V_{12} NPs) in a one-pot procedure.[253] The negatively-charged surface of the Au^0@V_{12} NPs allowed the easy fabrication of multilayer films on ITO-coated electrodes based on the electrostatic attraction with the positively charged PEI using a LbL assembly method (Figure 17 (c)). CV experiments indicated the Au^0@V_{12} NPs based composite films possessed good electrocatalytic activities in ORR.

Reduced POMs (rPOM) are extremely stable in alkaline solutions and can participate in electrocatalytic cycles. In 2015, a rPOM was used as assistant catalyst substrate for Pd^0 NPs.[254] In the synthetic procedure, $(NH_4)PMo^{VI}_{12}O_{40}$ POM was reduced (*in situ*) using $NaBH_4$ at the same time as

View Article Online
DOI: 10.1039/D0EE03407J

the Pd^{2+} salt was reduced to form a rPOM@Pd^0 hybrid with the Pd^0 NPs sitting on the surface of the rPOM. The use of rPOM as a support for Pd^0 NPs not only enhances the stability of the Pd^0 NPs via powerful support interactions minimizing the agglomeration but also efficiently enhances the ORR activity of the Pd^0 NPs via electron transfer between Pd^0 and rPOM. This rPOM@Pd^0 hybrid showed better electrocatalytic performance for ORR in alkaline media than the commercial Pt/C EC: E_{onset} = 1.078 V vs. RHE (0.051 V more positive compared to Pt/C EC) and almost no declining of catalytic activity during 1500 cycles. The performance enhancement is a result of the changes in the electronic structure of Pd^0 induced by synergistic interaction with the rPOM support, which weakens the interaction between Pd^0 and non-reactive oxygenated species (e.g. H_2O_2), providing more active sites for O_2 adsorption and activation.

Taking advantage of the high surface area and electrical conductivity of nanocarbons and their ability to be hybridized with POMs, several POM and carbon-based composites have been tested as ORR electrocatalysts. For instance, Wang et al. introduced a novel Pd^0/POM-PDDA-MWCNTs composite with high electrocatalytic activity for the ORR of fuel cells (Inset of Figure 18 (a)).[255] The construction implied the immobilization of Keggin-type tungstophosphoric acid ($H_3PW_{12}O_{40}$, PW_{12}) on the outer walls of MWCNTs functionalized by PDDA via the electrostatic forces between the negatively-charged PW_{12} and positively charged PDDA, followed by reductive deposition of Pd. The highly dispersed Pd^0/PW_{12} NPs supported on PDDA-MWCNTs showed a much higher ORR activity (in terms of kinetic current density (I_k), defined as the current in the absence of mass-transfer limitations) than acid-treated MWCNT-supported Pd catalysts and comparable activity with that of commercial Pt/C catalysts as seen in Figure 18 (a). The authors suggest that PW_{12} could act as both the effective mediator and as a source of mobile protons at the electrocatalytic interface. Moreover, XPS data indicate that the composite material possesses a significantly higher amount of metallic Pd compared with Pd/acid treated-MWNTs, and it would facilitate desorption of adsorbed oxygen. This is a critical parameter to maximize electrode performance, as limited oxygen desorption and bubble formation on the electrode can significantly increase the overpotential.

View Article Online
DOI: 10.1039/D0EE03407J

More recently, a novel Pd^0/POM/rGO nanocomposite was prepared by the assistance of $H_3PMo_{12}O_{40}$ (PMo_{12}) and hydrazine hydrate as reducing agent.[256] The electrostatic repulsive interactions derived by PMo_{12} anions effectively prevented the agglomeration of Pd^0 NPs, which were uniformly distributed over the surfaces of rGO. The composite revealed enhanced catalytic activity compared to its counterparts, as indicated by the higher current density on the linear sweep voltammograms (LSVs). Moreover, when methanol is added the LSV remains the same, demonstrating that the Pd^0/PMo_{12}/rGO catalyst has an excellent tolerance to the methanol cross-over effect.

Initial steps have been taken to replace the traditional noble-metal particles for the ORR by cheaper metals. POM-stabilized Ag^0 NPs on CNTs [257] or rGO [258] were prepared by a facile one-pot synthetic procedure using *in situ* photo-reduced PW_{12} Keggin anions as reducing agent and capping ligands. These nanohybrid tri-component systems were shown to be competitive to the commercial Pt/C for ORR. Using an alternative synthetic method, 2D Ag^0 nanonets (NN)@POM–graphene nanosheets (GNSs) were reported.[259] The composite was prepared using a Mo^V/Mo^{VI} mixed-valence POM, $H_7[\beta\text{-}PMo_4{}^{V}Mo_8{}^{VI}O_{40}]$, as the reducing, encapsulating and bridging agent to deposit an Ag^0 nanostructure on graphene. The as-prepared ternary Ag^0NN@POM–GNS composites showed high electrocatalytic ORR activity, with more positive onset (E_{onset}) and cathdoic peak (E_{pc}) potentials and higher cathodic peak current density (i_{pc}) compared to the binary Ag^0NN@POM composites. The authors attribute the excellent performance to the high catalytic activity of the Ag^0NN and the excellent electron transfer properties of GNSs, and their synergistic effect reinforced by the POM presence.

Liu and co-workers reported the electrochemical-reduction-assisted assembly of ternary Ag^0NPs@PW_{12}–rGO,[260] where the POM worked as both electrocatalyst and capping ligand as displayed in Figure 18 (c). This composite showed much better electrocatalytic activities towards the ORR than binary Ag^0NPs@ PW_{12} and PW_{12}/rGO nanohybrids, with higher i_{pc} and a more positive E_{onset} and E_{pc} values. Moreover, these results proved that the hybrids were sufficiently competitive

View Article Online
DOI: 10.1039/D0EE03407J

with commercial Pt/C. More recently, a PW_{12}-modified Ag@Pt/MWCNT electrocatalyst was prepared by electrostatic interaction with positively charged chitosan-functionalized core-shell Ag@Pt NPs on MWCNTs.[261] The results showed that PW_{12} improves the electrocatalytic activity of Ag@Pt NPs; with a $E_{1/2}$ (half-wave electrode potential) for the ORR which positively shifted 44 mV from that of Ag@Pt NPs/MWCNTs, and a mass activity (I_m) and specific area activity (I_s) about 2 times higher than those of Ag@Pt NPs/MWCNTs. The enhanced activity can be explained by the protective effect of the PW_{12} layer on the catalyst surface. The negative surface potential established over the catalyst surface protects complex metal anions from being subjected to electrostatic repulsion thereby conserving the active metal species on the catalyst surface. The performance of Nano-Heterostructure POM is summarized in Table 3.

In the search for Pt-free catalysts, considerable efforts have also been devoted to investigating metalloporphyrin catalysts for ORR, particularly Fe or Co porphyrin complexes.[262] However, little attention has been given to the combination of cationic metalloporphyrins and anionic POMs. In 2012, a PW_{12}/porphyrin composite based on a mixture of cationic [5,10,15,20-tetrakis(1-methyl-4-pyridinio)porphyrin]cobalt(II) (CoPP) and anionic PW_{12} supported on carbon black was reported as an active ORR electrocatalyst.[263] The results showed that cobalt ion was vital for the formation of the active ORR species, but might be attributed to the interaction of Co with POM that significantly improved the ORR activity. Hybrid ORR electrocatalysts have been prepared by ionic self-assembly of positively charged Fe(III) *meso*-tetra(*N*-methyl-4-pyridyl) porphyrin (FeP) with negatively-charged PMo_{12} in the presence of suspended MWCNTs.[264] Figure 18 (b) shows the schematic illustration of steps involved in the synthesis of hybrid ORR catalyst. Compared with individual PMo_{12} and FeP, the hybrid FeP/PMo_{12}-MWCNT electrocatalyst demonstrated a much higher ORR activity in terms of E_{onset} and $E_{1/2}$ in acidic media due to the high proton conductivity of PMo_{12} together with the large surface area and high electrical conductivity from the MWCNTs.

Interestingly, Deng's group has developed a liquid-catalyst-mediated fuel cell (LCFC) employing only Mo–V–P POM solutions as electrocatalysts and constructed using a Nafion 115 membrane sandwiched between two 3D graphite electrodes with no metal loading.[265-267] In these cells, a Keggin-type $H_3PW_{11}MoO_{40}$ solution oxidizes the biomass under sunlight or heating (at the anode), while a modified (non-Keggin) $H_{12}P_3Mo_{18}V_7O_{85}$ aqueous solution leads to the reduction of oxygen (in the cathode). The two POM solutions have different redox potentials and, unlike noble-metal catalysts, have the advantage of being tolerant to catalyst-poisoning organic and inorganic contaminants. Therefore, raw biomasses, such as cellulose, starch, and even grass or wood powders can be used directly to produce electricity without prior purification. It is noteworthy that, contrary to conventional fuel cells, in which small molecules such as hydrogen and methanol are the best fuels, biomass fuels are more favorable for this novel LCFC with respect to their power densities. In another study, Mo–V–P POM solutions, $H_{3+x}PV_xMo_{12-x}O_{40}$ (x = 0, 2, and 3), were applied as redox mediators for the ORR in polymer electrolyte fuel cells.[268] In this electrochemical system, the POM is reduced over the carbon cathode, and then the resultant rPOM is re-oxidized by exposure to the dissolved oxygen in the regenerator. The substitution quantity of V in the POM significantly affected the onset reduction potential as well as the current density achieved; $H_6PV_3Mo_9O_{40}$ was the most suitable mediator in terms of the electrochemical reduction property. The principle of using POM solutions and carbon as the cathode ORR catalyst can provide new methods for the improvement of other fuel cell systems.

View Article Online
DOI: 10.1039/D0EE03407J

4.3 Other Catalytic applications

4.3.1 Carbon dioxide reduction reaction

The increasing concentration of atmospheric CO_2 due to the industrial era is alarming and has now crossed the threshold of 400 ppm.[269] Although massive emission of CO_2 has resulted in serious environmental problems, it still is an important non-toxic, highly abundant and cheap carbon feedstock. Photo/electrocatalytic carbon dioxide reduction reaction (CO_2RR) represents a favorable means that can reduce CO_2 to highly valued hydrocarbon fuels or chemicals by using renewable solar energy or electricity as driving force. For CO_2RR, the most important and ambitious goal is to realize the efficient, selective and durable transformation of CO_2 into specific product with a view to increasing the possibility of large-scale utilization. The major challenge is to develop efficient catalysts for CO_2RR. The desirable photocatalyst for CO_2RR should at least have following features: i) a suitable band gap structure for absorbing photons; ii) an efficient separation and transport of photo-generated electron-hole pairs; iii) large number of active adsorption and reaction sites for promoting photocatalytic reaction.[278-280]

The research in photocatalytic CO_2RR is focused on finding catalysts that can work in visible light (>380nm) and are able to sustain the multi-electron transfer process. The final products of such a process are carbon monoxide (CO), formic acid (HCOOH), formaldehyde (HCHO), methanol (CH_3OH), and methane (CH_4).[270,271] It is noteworthy that some of the end products of this reaction are useful in their own right. For example, formic acid is a very promising hydrogen carrier and an important reagent in organic synthesis processes. POMs as one kind of molecular photocatalysts that display quasi-semiconductor photochemical properties also have many advantages in performing CO_2RR, such as superior solution, thermal stability and adjustable redox potential and reversible redox activity, which have also been reflected in photocatalytic HER and OER. Their good solution stability can enable them to carry out photocatalytic CO_2RR in water or other solvents, and their own redox properties can assist the multi-electron and multi-proton transfer process required for the conversion of CO_2 to products. Of course, the research on CO_2RR based on POM-based photocatalysts is still in its infancy, some meaningful conclusions need to be obtained based on more investigations. Neumann and co-workers[283] demonstrated the first practical utilization of Ru^{III} substituted Keggin structure, $[(C_6H_{13})_4N_5][Ru^{III}\text{-}(H_2O)SiW_{11}O_{39}]$ for the photoreduction of CO_2 to CO with Et_3N as reducing agent. DFT calculations suggests that CO_2 is preferably coordinated in a side on manner to Ru^{III} in the POM through formation of a RuO bond, further stabilized by the interaction of the electrophilic C atom of CO_2 to an O atom of the POM. The interaction of the nucleophilic O atom of CO_2 to Ru atom and the formation of $O_2C\text{-}NMe_3$ zwitterion stabilize both Ru-O and C-N interactions and determine the promotional effect of an amine on the activation of CO_2 by

View Article Online
DOI: 10.1039/D0EE03407J

POM molecule. Besides, several approaches are employed to construct heterogeneous crystalline POM-based photocatalysts for CO_2RR. Recently, Lan et al.[288] prepared several efficient heterogeneous POM-based photocatalyst systems and demonstrated an effective reduction of CO_2 to CH_4 with high selectivity and activity. They first synthesized two pure inorganic POM-based frameworks constructed with strong reductive [P4Mo_6V] units, NENU-605 and NENU-606, both of which can be used as heterogeneous catalysts for photocatalytic CO_2RR. It should be noted that this is the first POM-based crystalline photocatalysts system to reduce CO_2 to CH_4 in water with a high selectivity of 85.5%. In this work, the strong reductive [P_4Mo_6V] units serving as multielectron donor played a crucial role in promoting the 8 electrons and 8 protons transfer process required for CO_2-to-CH_4 conversion. These works indicate that developing strong reducing POM into photocatalyst architecture can increase the possibility of reducing CO_2 to CH_4 or other high-value carbon-based products accompanied with multiple processes. Table 4 shows the examples of best POM based photocatalysts for CO_2RR.

Reducing CO_2 into value-added fuels (such as C_2H_4, CH_4, CO) or chemicals (such as HCOOH, CH_3OH, C_2H_5OH) is one of the promising paths to address environmental issues and affords a convenient solution for energy conversion. Compared with the photocatalytic CO_2 reduction, electrical energy-driven CO_2 reduction is also an effective technology to realize this reaction process and commonly shows higher conversion efficiency. The brief list with their standard reduction potential and chemical reaction can be found in a paper by Qiao et al.[272] Nevertheless, HER as competitive reactions in aqueous electrolytes reduces the conversion efficiency of CO_2 during the electrochemical process due to their comparable thermodynamic potential. Therefore, the search of superior electrocatalysts with excellent electrochemical activity and suppressive HER is of great importance to develop CO_2RR. An ideal electrocatalysts for CO_2RR are expected to have following characteristics: i) flexible redox ability for the multielectron transfer, ii) high Faradaic efficiency and selectivity for the CO_2RR, iii) high structural and performance stability during a long-term electrochemical process, iv) high catalytic activity with a low electrochemical overpotential, and v)

View Article Online
DOI: 10.1039/D0EE03407J

scalable synthesis from low cost raw materials. Recent focus is on the development of heterogeneous elelctrocatalysts in nanostructured form, while the contrary homogeneous elelctrocatalysts mainly involve molecular metal complexes and macrocyclic organics.

Owing to the capability of POMs to undergo reversible multi-electron redox reactions without decomposition, they can be used along with a co-catalyst that brings down the activation energy for CO_2 reduction. Moreover, POMs as weak bases could promote the formation of hydrogen-bond networks near the CO_2 coordination center to favor proton-coupled electron transfer that occurs when the proton source is close to the catalytically active center. Electrocatalytic reduction of CO_2 with POM was first reported by Kozik et al.[278]. It was observed that α-$[SiW_{11}O_{39}Co]^{6-}$ showed the electrocatalytic activities for CO_2 reduction, however, the final CO_2 reduction product was unstated. More than decade later, Proust et al. reinvestigated this reaction in more detail by using [α-$SiW_{11}O_{39}Co]^{6-}$ in the electro-assisted reduction of CO_2.[290] The [α-$SiW_{11}O_{39}Co]^{6-}$ contained a Co^{II} in place of a W^{VI}. The square-pyramidal CoO_5 with a vacant site was generated by losing a coordinated water molecule from $CoO_5(H_2O)$ octahedral when the POM was extracted from aqueous to organic media. Except CO and HCHO, neither H_2 nor other CO_2 reduction products were detected. This indicated the unique selectivity of [α-$SiW_{11}O_{39}Co]^{6-}$ POM catalyst in the electroreduction of CO_2. The turnover of CO_2 to CO reached to 3.7 with the faradic efficiency of 13%. HCHO was the other detectable product with amount varied from 2.1×10^{-7} to 2.2×10^{-6} mol with the faradic yield varying from 25% (high HCHO content with low electrolysis charge) to 0.8% (low HCHO content with high electrolysis charge). Likewise, Wang et al has investigated MOFs as co-catalysts and combined them with POMs.[273] The bonds between Zn^{2+} ions on POM and carboxylates porphyrin were formed under hydrothermal conditions using M-TCPP = tetrakis[4-carboxyphenyl]-porphyrinato-M, as ligands. Here M is for metal Co, Fe, Ni and Zn. The electrochemical performance of the reduction reaction was evaluated in an airtight three-electrode electrochemical H-type cell, where a proton exchange membrane (Nafion® 212) separated the compartments. The performance of different metal POM-MOF are summarized in the Table 5. The mechanism of CO_2 reduction in presence of POM and effect

View Article Online
DOI: 10.1039/D0EE03407J

of temperature on reduction reaction initiated by different driving forces needs to be investigated further to develop this technology for commercial application.

4.3.2 Nitrogen reduction reaction

Nitrogen (N_2) makes up 78% of the total gaseous composition of the atmosphere. However, fixing nitrogen in soil is still difficult but important reaction needed to maintain the global ecosystem. To supply the necessary nitrogen to plants, ammonia is produced using the Haber–Bosch approach, which is energy intensive and carried out under harsh conditions. Hence, finding alternative ways or catalysts for the nitrogen reduction reaction (NRR) is crucial. Recently, Li et al used a typical MOF material, zeolitic imidazolate framework-67 (ZIF-67) with network tetrahedral topologies to adsorb N_2 on its porous structure.[274] The ZIF-67 was combined with various transition-metal-substituted POMs to supply multiple electrons to efficiently carry out NRR. Their performance towards NRR was evaluated in a sealed reactor with 300 mg of photocatalyst, 80 mL of distilled water and 20 mL of ethyl alcohol. The reaction was carried out at room temperature and N_2 was introduced in the reaction vessel at 1 L/minute, for an hour. As seen from Figure 19 (a), the ZIF-67/POM composite nanomaterials showed higher catalytic performance than that of ZIF and POMs alone with highest N_2 fixation efficiency reaching 149.0 μmol/L at 1 h, yielding a solar to ammonia (STA) efficiency of 0.032 % for ZIF-67@PMo_4V_8. The energy levels and electron-transfer mechanism for ZIF-67 and POMs composite photocatalyst is shown in Figure 19b. Accordingly, the porous ZIF-67 adsorbs a large amount of N_2 while the POMs are reduced under light conditions, and the reduced POMs more easily stimulate electrons to participate in the catalytic process. After the reaction, the reduced POMs react with the oxidant (e.g., O_2) to turn into their oxidized state and forms a complete self-healing and circulatory system (Figure 19b). Another important example of POM-based catalyst for NRR is demonstrated by Wang et al.[275] They used PMo_{12}@MOF-100(Fe) POM with PVP (polyvinylpyrrolidone) as a precursor to synthesize two FeMo-based electrocatalysts, $Fe_{1.89}Mo_{4.11}O_7/FeS_2$@C and $FeMoO_4/FeS_2$@C by hydrothermal methods. The

View Article Online
DOI: 10.1039/D0EE03407J

$Fe_{1.89}Mo_{4.11}O_7/FeS_2@C$ showed outstanding catalytic performance with a high NH_3 yield rate (105.3 µg h^{-1} $mgcat.^{-1}$) and Faradaic efficiency (54.7%) in acidic electrolytes at -0.4 V vs. RHE, which is higher than $FeMoO_4/FeS_2@C$, and most reported electrocatalysts for NRR. Further electrochemical experiments in alkaline electrolytes reveal the overall NRR catalytic activity of $Fe_{1.89}Mo_{4.11}O_7/FeS_2@C$ (NH_3 yield of 86.3 µg h^{-1} $mgcat.^{-1}$, FE of 53.6% at -0.4 V vs. RHE). The NRR performances of POM based catalysts is summarized in Table 6.

4.3.3 Biomass conversion using POMs

Due to the oxygen rich characteristics of biomass, POMs are now being investigated to catalyze biomass conversion reactions for obtaining valuable oxygen-containing chemicals. Along these lines, Voß et al investigated the conversion pathway of glucose using either an oxygen or a nitrogen atmosphere.[276] The reaction was catalyzed by Lindqvist-type POM $K_5[V_3W_3O_{19}]$. The time dependent distribution of products of the above catalyzed reaction is shown in Figure 20. Further, the Keggin type POM catalyst $H_6[PV_3Mo_9O_{40}]$ and a substrate variation (glucose and glyceraldehyde) was also tested under aerobic (oxygen) and anaerobic (nitrogen) environment (see Table 7). It was found that the substrate and the reaction conditions (whether it is aerobic or anaerobic) determine the final product (folic acid (FA), or lactic acid (LA)). Hence, it is shown that a suitable catalyst can be chosen, which can be combined with a given set of parameters to convert biomass into the desired chemical/s.

Liu et al used various kinds of biomass (cellulose, lignin and even wood and grass powders) in a novel electrolytic reduction process at low temperature.[277] The process was catalyzed by a POM solution as depicted in figure below. No current was observed initially at an applied potential of 1.1V, even in the presence of glucose. However, when a PMO_{12} solution was pumped through the anode along with biomass, a sharp increase in the electrolysis current was observed together with the corresponding bubbles of H_2 gas at the cathode side as can be seen from Figure 21 (a, b). The use of POMs to produce H_2 at low electric energy consumption from biomass is very young but promising

View Article Online
DOI: 10.1039/D0EE03407J

technology that remains to be deeply explored. Various parameters such as temperature, active sites on the POM, electrolyte effect and electron transport paths need further investigation.

Anna Bukowski et al developed a concept called the Ionosolv method in which fractionation of lignocellulosic biomass (wood) was achieved using a low-cost IL.[278] Bio-derived formic acid was produced using a POM catalyst and molecular oxygen as an oxidant. The IL alkylammonium [TEA][HSO_4] was used as a solvent to break down the lignocellulosic feedstock. The best performance was achieved using vanadium substituted POM ($H_8[PV_5Mo_7O_{40}]$) with respect to folic acid yield (23%) from hardwood (beech), which corresponds to a folic acid selectivity of 54%. The Ionosolv method was also used with other types of wood such as softwood (pine) and grass biomass (Miscanthus). This method should be evaluated further for final product purity, catalyst recyclability and cost effectiveness of the whole process. This step will test the commercial viability of the concept.

4.3.4 Methanol oxidation using POMs

Direct alcohol fuel cells (DAFCs) are systems that extract energy by selective oxidation of the alcohol. Hydrogen ions produced by alcohol oxidation are transported across the proton-exchange membrane to the cathode, where they react with O_2 to form water. The overall reaction occurring in a DAFC is $2\ C_nH_{2n+1}OH + 3\ nO_2 \rightarrow 2\ nCO_2 + 2\ (n+1)H_2O$. DAFCs have been also proposed as the green energy for future vehicles due to its easy fuel storage, high energy density and low emission of pollutants.[279] The most widely studied ones utilize methanol and ethanol and are referred as a direct methanol fuel cell (DMFC) or a direct ethanol fuel cell (DEFC), respectively. Several efforts have been devoted in the past years to develop efficient catalysts and are outlined in the previous review articles. For instance, platinum[280] based or nano-metals (noble and non-noble)[281] catalysers with their potential application in portable devices[282] due to high energy density and easy handling among others. In this section, we have highlighted key features and complement the abovementioned reviews with the most important investigations that have reported POMs-based catalytic reactions.

Pt is commonly employed as the catalyst in acidic media in DMFC or DEFC devices. However, Pt on its own is not a highly efficient catalyst due to poisoning from the strongly adsorbed

View Article Online
DOI: 10.1039/D0EE03407J

species such as $CH_{(ad)}$,$CH_{3(ad)}$, and $CO_{(ad)}$ generated during oxidation. Accordingly, many efforts have been dedicated to improve the poisoning tolerance of the metal. Normally researchers encounter partial oxidation to aldehydes, ethers or carboxylic acids[283-285] therefore the system is not extracting all the power of the system. Most of the papers reviewed here are uses commercial POMs (as seen in Table 8), but as an anti CO poisoning agent of the real catalyst (which is Pd, Pt, Ru, Au or composites) and/or morphology control rather than alcohol oxidation. For example, Shi et al[279] studied the performance of Pt/Pyridine ionic liquid POM/rGO (Pt/$(epy)_3PMo_{12}O_{40}$/rGO) in acidic conditions, suggesting improvement in the reaction. The reason attributed to the fact that POM promote uniformity of Pt dispersion ((111) face) and exhibits anti-CO poisoning properties. This is one of the main conclusions extracted from the past research in the field as the POM improve the crystal size homogeneity and decrease the size. The second conclusion is that POMs improve the catalyst stability by preventing the surface poisoning with by-products that are strongly adsorbed.[286-288] However, Barczuk et al.[289] doubts the electron mediating function of the PMo_{12} in the electrooxidation of ethanol, despite the fact the chronoamperometric results evident an increase in current and stability of the metal catalyst (Pt, Pt-Ru, Rt-Sn/C etc.). They propose that PMo_{12} stabilize the oxo-groups on top of metal, which are known to induce the oxidation of the poisoning species (such as CO).

Various POMs have been proposed and tested as additives for methanol oxidation including PMo_{12}, SiW_{12}, PW_{12},[290,291] wheel-shaped VV –VIV mixed-valence tungstovanadate (V12),[253] and their composites. Of special interest, Bommineni S et al.[283] investigated the methanol oxidation with pure PMo_{12} and three derivative (pyridine, niobium and pyridine-niobium salt). The authors analyse the methanol oxidation under a gas stream (Ar, O_2 MeOH) at 533K adjusting the conversion around 10%. It was revealed that the PMo_{12} and its niobium salt give mainly dimethoxymethane while the niobium pyridine derivative gives preferentially dimethyl ether. The pyridine POM salt gives mixture of the products. Likewise, Chen et al.[292] studied the influence of WO_x and PW_{12} on the PtRu/C catalyst, suggesting an improvement in the catalytic properties due to both: 1) WO_x facilitates the nanoparticles distribution on carbon while 2) PW_{12} improve the poison resistance behaviour of the

View Article Online
DOI: 10.1039/D0EE03407J

catalyst. Similarly, the catalytic effect of a complex POM ($H_{3+x}PMo_{12x}V_xO_{40}$ (x =0,1,2,3)) and surface-supported $VO_x/H_3PMo_{12}O_{40}$ was also investigated.[293] The study was performed in isothermal fixed bed reactor with a gas stream at 250ºC. The volume composition of the gaseous reactant feed was 6% CH_3OH, 13% O_2 and balance He, with a total flow rate of 100 mL/min. The results suggests that the introduction of the VO_x sites increases the formaldehyde selectivity and decreases the dimethyl ether selectivity. The VO_x units in the primary Keggin structure were slightly more active than the surface VO_x species, and both VO_x sites were significantly more active than the MoO_x sites in the primary Keggin structure. Khadempir et al. synthetized pseudospherical palladium nanoparticles protected by PMo_{12}[290] at different pH or supported on graphene nanosheets (GNS)[294] in acid solution. According to the results, Pd/PMo_{12}/GNS demonstrates better poison tolerance as compared to the reference sample due to a superior ionic and electronic conductivity, small and highly dispersed nanoparticules. We have summarized recent works in the Table 8.

5. Conclusion and Future Challenges

Polyoxometallates (POMs) is a unique class of materials that have a broad range of potential forms and applications. Both their possible forms and their subsequent applications continue to be widely studied. In this review, we briefly described the history and progress of this class of materials with particular emphasis on energy-related applications.

The use of POMs in supercapacitors can offer significant opportunity to enhance the energy density of these devices by contributing pseudocapacitive charge storage effects in an efficient manner. This is a consequence of the high surface-to-bulk ratio of POMs, as well as their multiple redox states. POMs were shown to be suitable for improving performance in a variety of approaches to their use. These range from very simple addition of POMs to typical AC electrode pastes, to more complex methods of chemical linking to 2D materials and other emerging nanomaterials. However, because of their generally low electrical conductivity, the linking of POMs to an appropriate

View Article Online
DOI: 10.1039/D0EE03407J

conducting scaffold is particularly important and challenging, however progress is being made, for example, by using DFT simulation and prediction.

For similar structure-property reasons as with SCs, these small cluster molecules offer the opportunity to improve the performance of battery technologies, and relatively speaking, this is being more widely explored. The poor electrical conductivity of pristine POMs and their typical high solubility in battery electrolytes results in a low cycling stability and poor rate performance when used as electrode materials. POMs-based composites can overcome these issues. Therefore, developing new POM-based composites is needed to expand the use of POMs in the field of rechargeable batteries as well as SCs. Particular attention could be given to POMOFs/carbon nanostructures, in which MOFs can mitigate the dissolution issue, while carbon nanostructures can increase the conductivity of POMs. More work focused on developing simple low-cost methods for the synthesis of POMOFs with high conductivity and controllable homogeneity, would be expected to improve their electrochemical performance in energy storage devices.

The energy storage mechanism for POMs-based electrode materials for rechargeable batteries and SCs are still not fully understood. The relatively high number of electron exchanges per molecule, when compared to other redox materials used in cathodic and anodic battery storage, complicate this. Therefore, detailed analysis is necessary to understand the reactions at the electrode/electrolyte interface. Advanced *in situ/operando* characterisation (microscopic and spectroscopic) and continued theoretical studies (such as by DFT) will likely be a necessary part of gaining an in-depth understanding of the reaction mechanisms and structural changes in POM-based electrodes, in order to promote further improvement in this field.

The interesting properties of POMs for energy storage are linked to the number of active sites in POM molecules, and these are also a critical property for catalysis. The application of POMs as catalysts is discussed for both water oxidation and ORR, as well as for other catalytic applications. Regarding water oxidation, the following three principles for the design of molecular WOCs recently outlined by Craig et al provide a strong point of reference for summarizing the topic:[295] (1) Research

View Article Online
DOI: 10.1039/D0EE03407J

should focus on transition metal complexes which can undergo additional electron transfer steps by stabilizing high oxidation states, hence reducing the overpotential. (2) existing knowledge of heterogeneous catalysis, where DFT is used for material design, should be used to optimize the binding of the different reaction intermediates to the transition metal center. (3) electronic and steric effects of metal ligands should be investigated systematically. Advances in this field will allow the future implementation of ideal molecular WOCs into commercial electrolyzers with greatly enhanced selectivity, stability, and electron transport.

In the case of ORR catalysts, hybrid materials combining POMs with metal NPs, carbon-based materials and porphyrins have shown favorable performances. The synergies between POMs and the supports are crucial to improve the final composite stability and to achieve favorable ORR performances. On the other hand, pristine POMs with intrinsic catalytic activity towards ORR are scarce, and continuous efforts should be devoted to the discovery of cost-effective, efficient, and durable noble metal-free POM catalysts with good ORR performance. In general, the discussed examples demonstrate that the catalytic properties of POMs can be engineered finely to meet the requirements of different reactions. The molecular nature of POMs is enormously tunable and continues to present unique opportunities in the investigation of catalytic systems. Future research will focus on further advancements in POM design and immobilization, with special attention to the stability of the catalysts. The combination of POMs with metal NPs, carbon-based materials and other molecules has been shown to lead to favorable performance. In a synergistic fashion, these hybrid materials exhibit properties not accessible from the individual components. Furthermore, POMs have been shown to be useful for efficient production of hydrogen and for improved fuel cell performance.

In all three of the main energy-related contexts of applying POMs, one of the critical challenges that continues to be investigated is the anchoring of the materials to suitable substrates. POMs can very much be viewed as water-soluble oxyanions, just as can be found in the molecular pairing of many acid types. However, their relatively large molecular size also makes them true NP materials that present the opportunities mentioned in this review, when the particles are well dispersed

View Article Online
DOI: 10.1039/D0EE03407J

and fixed to a supporting scaffold. Amongst other methods, achieving this has been done through covalent and non-covalent approaches for carbonaceous and polymeric materials.

Despite this, there remains considerable room to improve knowledge in this area, and for it to be rationally guided, such as by DFT investigative work. Collaboration between theoretical modelers and experimental researchers will enable the discovery of new structures and new results in applications of POMs.

Together the outputs of theoretical investigations, advanced characterization work, and the synthesis and testing of novel POMs and POM composites can be expected to yield significant benefits. A deeper understanding of these materials and their structure and activity represents an accomplishment to advanced physical chemistry, given their complexity. While at the same time, their excellent activity and versatility make them exciting materials for applications such as in energy as we have discussed here. Overall, continued research into POMs for energy can be expected to make a significant contribution towards solving sustainable energy problems, at large.

Author contributions

D.P.D. and P.G.R. conceived the idea of the project. The energy storage part was written by M.H., S.A. and N.R.C. while A.S., S.G.F. and R.V.B. have contributed the energy conversion sections. All authors contributed equally to the preparation and reviewing manuscript.

Acknowledgements

D.P.D. acknowledges the Queensland University of Technology (start-up grant: 323000-0424/07) and Australian Research Council (ARC), Australia for the Future Fellowship (FT180100058). D.P.D. would also like to acknowledge the financial support from Centre for Materials Science, QUT, Australia. Sara Goberna-Ferrón has received funding from the postdoctoral fellowship programme Beatriu de Pinós, funded by the Secretary of Universities and Research (Government of Catalonia)

View Article Online
DOI: 10.1039/D0EE03407J

and by the Horizon 2020 programme of research and innovation of the European Union under the Marie Skłodowska-Curie grant agreement No 801370.

References

(1) Rogelj, J.; Forster, P. M.; Kriegler, E.; Smith, C. J.; Séférian, R. Estimating and tracking the remaining carbon budget for stringent climate targets. *Nature* **2019,** *571* (7765), 335.

(2) Delmas, C. Sodium and Sodium-Ion Batteries: 50 Years of Research. *Advanced Energy Materials* **2018,** *8* (17), 1703137.

(3) Schlemmer, W.; Nothdurft, P.; Petzold, A.; Riess, G.; Frühwirt, P.; Schmallegger, M.; Gescheidt-Demner, G.; Fischer, R.; Freunberger, S. A.; Kern, W. 2-Methoxyhydroquinone from Vanillin for Aqueous Redox-Flow Batteries. *Angewandte Chemie International Edition* **2020**.

(4) Whittingham, M. S.; ACS Publications, 2020.

(5) Jayaramulu, K.; Horn, M.; Schneemann, A.; Saini, H.; Bakandritsos, A.; Ranc, V.; Petr, M.; Stavila, V.; Narayana, C.; Scheibe, B. Covalent Graphene-MOF Hybrids for High-Performance Asymmetric Supercapacitors. *Advanced Materials* **2020**, 2004560.

(6) Khoshsirat, N.; Yunus, N. A. M.; Hamidon, M. N.; Shafie, S.; Amin, N. Analysis of absorber layer properties effect on CIGS solar cell performance using SCAPS. *Optik* **2015,** *126* (7-8), 681.

(7) Matos, B. R.; Dresch, M. A.; Santiago, E. I.; Moraes, L. P.; Carastan, D. J.; Schoenmaker, J.; Velasco-Davalos, I. A.; Ruediger, A.; Tavares, A. C.; Fonseca, F. C. Nafion membranes annealed at high temperature and controlled humidity: structure, conductivity, and fuel cell performance. *Electrochimica Acta* **2016,** *196*, 110.

(8) Pham, H. D.; Mahale, K.; Hoang, T. M. L.; Mundree, S. G.; Gomez-Romero, P.; Dubal, D. P. Dual Carbon Potassium-Ion Capacitors: Biomass-Derived Graphene-like Carbon Nanosheet Cathodes. *ACS Applied Materials & Interfaces* **2020,** *12* (43), 48518.

(9) Sultana, U. K.; He, T.; Du, A.; O'Mullane, A. P. An amorphous dual action electrocatalyst based on oxygen doped cobalt sulfide for the hydrogen and oxygen evolution reactions. *RSC advances* **2017,** *7* (87), 54995.

(10) Yadav, S. K.; Grandhi, G. K.; Dubal, D. P.; de Mello, J. C.; Otyepka, M.; Zbořil, R.; Fischer, R. A.; Jayaramulu, K. Metal Halide Perovskite@ Metal-Organic Framework Hybrids: Synthesis, Design, Properties, and Applications. *Small* **2020**, 2004891.

(11) Gómez-Romero, P.; Ayyad, O.; Suárez-Guevara, J.; Muñoz-Rojas, D. Hybrid organic–inorganic materials: from child's play to energy applications. *Journal of Solid State Electrochemistry* **2010,** *14* (11), 1939.

(12) Gomez-Romero, P.; Casan-Pastor, N. Photoredox chemistry in oxide clusters. Photochromic and redox properties of polyoxometalates in connection with analog solid state colloidal systems. *The Journal of Physical Chemistry* **1996,** *100* (30), 12448.

(13) Pope, Michael T.; Sadakane, M.; Kortz, U. Celebrating Polyoxometalate Chemistry. *European Journal of Inorganic Chemistry* **2019,** *2019* (3-4), 340.

(14) Casan-Pastor, N.; Gomez-Romero, P.; Jameson, G. B.; Baker, L. C. Crystal structures of. alpha.-[CoIIW12O40] 6-and its heteropoly blue 2e reduction product,. alpha.-[CoIIW12O40]

View Article Online
DOI: 10.1039/D0EE03407J

8-. Structural, electronic, and chemical consequences of electron delocalization in a multiatom mixed-valence system. *Journal of the American Chemical Society* **1991,** *113* (15), 5658.

(15) Gumerova, N. I.; Rompel, A. Synthesis, structures and applications of electron-rich polyoxometalates. *Nature Reviews Chemistry* **2018,** *2* (2), 1.

(16) Dawson, B. The structure of the 9 (18)-heteropoly anion in potassium 9 (18)-tungstophosphate, K6 (P2W18O62). 14H2O. *Acta Crystallographica* **1953,** *6* (2), 113.

(17) Dexter, D. D.; Silverton, J. A new structural type for heteropoly anions. The crystal structure of (NH4) 2H6 (CeMo12O42). 12H2O. *Journal of the American Chemical Society* **1968,** *90* (13), 3589.

(18) Müller, A.; Kögerler, P.; Kuhlmann, C. A variety of combinatorially linkable units as disposition:† from a giant icosahedral Keplerate to multi-functional metal–oxide based network structures. *Chemical Communications* **1999,** (15), 1347.

(19) Long, D. L.; Tsunashima, R.; Cronin, L. Polyoxometalates: building blocks for functional nanoscale systems. *Angewandte Chemie International Edition* **2010,** *49* (10), 1736.

(20) Miras, H. N.; Yan, J.; Long, D.-L.; Cronin, L. Engineering polyoxometalates with emergent properties. *Chemical Society Reviews* **2012,** *41* (22), 7403.

(21) Graham, C. R.; Finke, R. G. The Classic Wells−Dawson Polyoxometalate, K6[α-P2W18O62]·14H2O. Answering an 88 Year-Old Question: What Is Its Preferred, Optimum Synthesis? *Inorganic Chemistry* **2008,** *47* (9), 3679.

(22) Horn, M.; MacLeod, J.; Liu, M.; Webb, J.; Motta, N. Supercapacitors: A new source of power for electric cars? *Economic Analysis and Policy* **2019,** *61*, 93.

(23) Zhao, Y.; Liu, J.; Wang, N.; Li, Q.; Hu, M. Rational selection of small aromatic molecules to functionalize graphene for enhancing capacitive energy storage. *Journal of Materials Chemistry A* **2018,** *6* (17), 7566.

(24) Horn, M.; Gupta, B.; MacLeod, J.; Liu, J.; Motta, N. Graphene-based supercapacitor electrodes: Addressing challenges in mechanisms and materials. *Current Opinion in Green and Sustainable Chemistry* **2019,** *17*, 42.

(25) Gómez-Romero, P.; Lira-Cantú, M. Hybrid organic-inorganic electrodes: The molecular material formed between polypyrrole and the phosphomolybdate anion. *Advanced Materials* **1997,** *9* (2), 144.

(26) Cuentas-Gallegos, A. K.; Lira-Cantú, M.; Casañ-Pastor, N.; Gómez-Romero, P. Nanocomposite Hybrid Molecular Materials for Application in Solid-State Electrochemical Supercapacitors. *Advanced Functional Materials* **2005,** *15* (7), 1125.

(27) Gómez-Romero, P.; Chojak, M.; Cuentas-Gallegos, K.; Asensio, J. A.; Kulesza, P. J.; Casañ-Pastor, N.; Lira-Cantú, M. Hybrid organic–inorganic nanocomposite materials for application in solid state electrochemical supercapacitors. *Electrochemistry Communications* **2003,** *5* (2), 149.

(28) Ruiz, V.; Suárez-Guevara, J.; Gomez-Romero, P. Hybrid electrodes based on polyoxometalate–carbon materials for electrochemical supercapacitors. *Electrochemistry Communications* **2012,** *24*, 35.

(29) Gupta, S.; Aberg, B.; Carrizosa, S. B. Functionalized graphene–polyoxometalate nanodots assembly as “organic–inorganic” hybrid supercapacitors and insights into electrode/electrolyte interfacial processes. *C—Journal of Carbon Research* **2017,** *3* (3), 24.

(30) Akter, T.; Hu, K.; Lian, K. Investigations of multilayer polyoxometalates-modified carbon nanotubes for electrochemical capacitors. *Electrochimica Acta* **2011,** *56* (14), 4966.

(31) Cuentas-Gallegos, A. K.; Martínez-Rosales, R.; Baibarac, M.; Gómez-Romero, P.; Rincón, M. E. Electrochemical supercapacitors based on novel hybrid materials made of carbon nanotubes and polyoxometalates. *Electrochemistry Communications* **2007,** *9* (8), 2088.

(32) Cuellar, E. A.; Desmond, M. J.; Google Patents, 1986.

(33) Palomino, P.; Suarez-Guevara, J.; Olivares-Marín, M.; Ruiz, V.; Dubal, D. P.; Gómez-Romero, P.; Tonti, D.; Enciso, E. Influence of texture in hybrid carbon-phosphomolybdic acid materials on their performance as electrodes in supercapacitors. *Carbon* **2017,** *111*, 74.

(34) Suárez-Guevara, J.; Ruiz, V.; Gomez-Romero, P. Hybrid energy storage: high voltage aqueous supercapacitors based on activated carbon–phosphotungstate hybrid materials. *Journal of Materials Chemistry A* **2014,** *2* (4), 1014.

(35) Chen, H. Y.; Wee, G.; Al-Oweini, R.; Friedl, J.; Tan, K. S.; Wang, Y.; Wong, C. L.; Kortz, U.; Stimming, U.; Srinivasan, M. A polyoxovanadate as an advanced electrode material for supercapacitors. *ChemPhysChem* **2014,** *15* (10), 2162.

(36) Hou, Y.; Chai, D.; Li, B.; Pang, H.; Ma, H.; Wang, X.; Tan, L. Polyoxometalate-Incorporated Metallacalixarene@Graphene Composite Electrodes for High-Performance Supercapacitors. *ACS Applied Materials & Interfaces* **2019,** *11* (23), 20845.

(37) Li, Q.; Zhang, L.; Dai, J.; Tang, H.; Li, Q.; Xue, H.; Pang, H. Polyoxometalate-based materials for advanced electrochemical energy conversion and storage. *Chemical Engineering Journal* **2018,** *351*, 441.

(38) Borrás-Almenar, J. J.; Coronado, E.; Müller, A.; Pope, M. *Polyoxometalate molecular science*; Springer Science & Business Media, 2003.

(39) Dubal, D. P.; Suarez-Guevara, J.; Tonti, D.; Enciso, E.; Gomez-Romero, P. A high voltage solid state symmetric supercapacitor based on graphene–polyoxometalate hybrid electrodes with a hydroquinone doped hybrid gel-electrolyte. *Journal of Materials Chemistry A* **2015,** *3* (46), 23483.

(40) Genovese, M.; Lian, K. Ionic liquid-derived imidazolium cation linkers for the layer-by-layer assembly of polyoxometalate-MWCNT composite electrodes with high power capability. *ACS applied materials & interfaces* **2016,** *8* (29), 19100.

(41) Ding, Y.-H.; Peng, J.; Lu, H.-Y.; Yuan, Y.; Khan, S.-U. Tungsten addenda mixed heteropolymolybdates supported on functionalized graphene for high-performance aqueous supercapacitors. *RSC Advances* **2016,** *6* (84), 81085.

(42) Dubal, D. P.; Ballesteros, B.; Mohite, A. A.; Gómez-Romero, P. Functionalization of polypyrrole nanopipes with redox-active polyoxometalates for high energy density supercapacitors. *ChemSusChem* **2017,** *10* (4), 731.

(43) Chinnathambi, S.; Ammam, M. A molecular hybrid polyoxometalate-organometallic moieties and its relevance to supercapacitors in physiological electrolytes. *Journal of Power Sources* **2015,** *284*, 524.

(44) Thompson, D. W.; Ito, A.; Meyer, T. J. [Ru (bpy) 3] 2+* and other remarkable metal-to-ligand charge transfer (MLCT) excited states. *Pure and Applied Chemistry* **2013,** *85* (7), 1257.

(45) Chai, D.; Gómez-García, C. J.; Li, B.; Pang, H.; Ma, H.; Wang, X.; Tan, L. Polyoxometalate-based metal-organic frameworks for boosting electrochemical capacitor performance. *Chemical Engineering Journal* **2019,** *373*, 587.

(46) Tian, J.; Lin, B.; Sun, Y.; Zhang, X.; Yang, H. Porous WO3@ CuO composites derived from polyoxometalates@ metal organic frameworks for supercapacitor. *Materials Letters* **2017,** *206*, 91.

(47) Dong, Y.; Chen, L.; Chen, W.; Zheng, X.; Wang, X.; Wang, E. rGO Functionalized with a Highly Electronegative Keplerate-Type Polyoxometalate for High-Energy-Density Aqueous Asymmetric Supercapacitors. *Chemistry–An Asian Journal* **2018,** *13* (21), 3304.

(48) Pakulski, D.; Gorczyński, A.; Czepa, W.; Liu, Z.; Ortolani, L.; Morandi, V.; Patroniak, V.; Ciesielski, A.; Samorì, P. Novel Keplerate type polyoxometalate-surfactant-graphene hybrids as advanced electrode materials for supercapacitors. *Energy Storage Materials* **2019,** *17*, 186.

(49) Cuentas-Gallegos, A. K.; López-Cortina, S.; Brousse, T.; Pacheco-Catalán, D.; Fuentes-Quezada, E.; Mosqueda, H.; Orozco-Gamboa, G. Electrochemical study of H 3 PMo 12 retention on Vulcan carbon grafted with NH 2 and OH groups. *Journal of Solid State Electrochemistry* **2016,** *20* (1), 67.

(50) Suárez-Guevara, J.; Ruiz, V.; Gómez-Romero, P. Stable graphene–polyoxometalate nanomaterials for application in hybrid supercapacitors. *Physical Chemistry Chemical Physics* **2014,** *16* (38), 20411.

(51) Chen, J.; Yao, B.; Li, C.; Shi, G. An improved Hummers method for eco-friendly synthesis of graphene oxide. *Carbon* **2013,** *64*, 225.

(52) Hummers Jr, W. S.; Offeman, R. E. Preparation of graphitic oxide. *Journal of the American Chemical Society* **1958,** *80* (6), 1339.

(53) Azadmanjiri, J.; Srivastava, V. K.; Kumar, P.; Wang, J.; Yu, A. Graphene-supported 2D transition metal oxide heterostructures. *Journal of Materials Chemistry A* **2018,** *6* (28), 13509.

(54) Yin, H.; Zhao, S.; Wan, J.; Tang, H.; Chang, L.; He, L.; Zhao, H.; Gao, Y.; Tang, Z. Three-Dimensional Graphene/Metal Oxide Nanoparticle Hybrids for High-Performance Capacitive Deionization of Saline Water. *Advanced Materials* **2013,** *25* (43), 6270.

(55) Yang, M.; Choi, B. G.; Jung, S. C.; Han, Y.-K.; Huh, Y. S.; Lee, S. B. Polyoxometalate-coupled Graphene via Polymeric Ionic Liquid Linker for Supercapacitors. *Advanced Functional Materials* **2014,** *24* (46), 7301.

(56) Ensafi, A. A.; Heydari-Soureshjani, E.; Rezaei, B. Using (t-Bu) 5 [PW11CoO39] to fabricate a sponge graphene network for energy storage in seawater and acidic solutions. *Electrochimica Acta* **2018,** *289*, 13.

(57) Dubal, D. P.; Nagar, B.; Suarez-Guevara, J.; Tonti, D.; Enciso, E.; Palomino, P.; Gomez-Romero, P. Ultrahigh energy density supercapacitors through a double hybrid strategy. *Materials Today Energy* **2017,** *5*, 58.

(58) Skunik-Nuckowska, M.; Węgrzyn, K.; Dyjak, S.; Wisińska, N. H.; Kulesza, P. J. Polyoxometalate/hydroquinone dual redox electrolyte for hybrid energy storage systems. *Energy Storage Materials* **2019,** *21*, 427.

(59) Dubal, D. P.; Chodankar, N. R.; Vinu, A.; Kim, D.-H.; Gomez-Romero, P. Asymmetric Supercapacitors Based on Reduced Graphene Oxide with Different Polyoxometalates as Positive and Negative Electrodes. *ChemSusChem* **2017,** *10* (13), 2742.

(60) Lu, D.; Zhang, X.; Chen, H.; Lin, J.; Liu, Y.; Chang, B.; Qiu, F.; Han, S.; Zhang, F. A high performance solid-state asymmetric supercapacitor based on Anderson-type polyoxometalate-doped graphene aerogel. *Research on Chemical Intermediates* **2019,** *45* (5), 3237.

(61) Wang, Z.; Gu, J.; Li, S.; Zhang, G. C.; Zhong, J.; Fan, X.; Yuan, D.; Tang, S.; Xiao, D. One-step polyoxometalates-assisted synthesis of manganese dioxide for asymmetric supercapacitors with enhanced cycling lifespan. *ACS Sustainable Chemistry & Engineering* **2018,** *7* (1), 258.

(62) Dubal, D. P.; Chodankar, N. R.; Qiao, S. Tungsten Nitride Nanodots Embedded Phosphorous Modified Carbon Fabric as Flexible and Robust Electrode for Asymmetric Pseudocapacitor. *Small* **2019,** *15* (1), 1804104.

(63) Ma, X. J.; Zhang, W. B. Tungsten Nitride for Capacitive Energy Storage. *ChemistrySelect* **2017,** *2* (28), 8726.

(64) Wang, F.; Xiao, S.; Hou, Y.; Hu, C.; Liu, L.; Wu, Y. Electrode materials for aqueous asymmetric supercapacitors. *Rsc Advances* **2013,** *3* (32), 13059.

(65) Dubal, D. P.; Abdel-Azeim, S.; Chodankar, N. R.; Han, Y.-K. Molybdenum Nitride Nanocrystals Anchored on Phosphorus-Incorporated Carbon Fabric as a Negative Electrode for High-Performance Asymmetric Pseudocapacitor. *iScience* **2019,** *16*, 50.

(66) Miao, J.; Lang, Z.; Zhang, X.; Kong, W.; Peng, O.; Yang, Y.; Wang, S.; Cheng, J.; He, T.; Amini, A.et al. Polyoxometalate-Derived Hexagonal Molybdenum Nitrides (MXenes) Supported by Boron, Nitrogen Codoped Carbon Nanotubes for Efficient Electrochemical Hydrogen Evolution from Seawater. *Advanced Functional Materials* **2019,** *29* (8), 1805893.

(67) Gómez-Romero, P.; Asensio, J. A.; Borrós, S. Hybrid proton-conducting membranes for polymer electrolyte fuel cells: phosphomolybdic acid doped poly (2, 5-benzimidazole)-(ABPBI-H3PMo12O40). *Electrochimica acta* **2005,** *50* (24), 4715.

(68) Kim, Y.; Ketpang, K.; Jaritphun, S.; Park, J. S.; Shanmugam, S. A polyoxometalate coupled graphene oxide–Nafion composite membrane for fuel cells operating at low relative humidity. *Journal of Materials Chemistry A* **2015,** *3* (15), 8148.

(69) Zhai, L.; Li, H. Polyoxometalate–Polymer Hybrid Materials as Proton Exchange Membranes for Fuel Cell Applications. *Molecules* **2019,** *24* (19), 3425.

(70) Wu, X.; Tong, X.; Wu, Q.; Ding, H.; Yan, W. Reversible phase transformation-type electrolyte based on layered shape polyoxometalate. *Journal of Materials Chemistry A* **2014,** *2* (16), 5780.

(71) Tong, X.; Thangadurai, V. Hybrid Gel Electrolytes Derived from Keggin-Type Polyoxometalates and Imidazolium-Based Ionic Liquid with Enhanced Electrochemical Stability and Fast Ionic Conductivity. *The Journal of Physical Chemistry C* **2015,** *119* (14), 7621.

(72) Wu, X.; Wu, W.; Wu, Q.; Yan, W. Thermoresponsive Polyoxometalate/Ionic Liquid Supramolecular Gel Electrolytes for Supercapacitors: Fabrication, Structure, and Heteropolyanion Structure Effect. *Langmuir* **2017,** *33* (17), 4242.

(73) Muniz, J.; Celaya, C.; Mejia-Ozuna, A.; Cuentas-Gallegos, A. K.; Mejia-Mendoza, L.; Robles, M.; Valdez, M. First principles study on the electronic structure properties of Keggin polyoxometalates on Carbon substrates for solid-state devices. *Theoretical Chemistry Accounts* **2017,** *136* (2), 26.

(74) Guillén-López, A.; Espinosa-Torres, N. D.; Cuentas-Gallegos, A. K.; Robles, M.; Muñiz, J. Understanding bond formation and its impact on the capacitive properties of SiW12 polyoxometalates adsorbed on functionalized carbon nanotubes. *Carbon* **2018,** *130*, 623.

(75) Chen, S.; Xiang, Y.; Katherine Banks, M.; Xu, W.; Peng, C.; Wu, R. Polyoxometalate-coupled graphene nanohybrid via gemini surfactants and its electrocatalytic property for nitrite. *Applied Surface Science* **2019,** *466*, 110.

(76) Yoshio, M.; Brodd, R. J.; Kozawa, A. *Lithium-ion batteries*; Springer, 2009.

(77) Światowska, J.; Barboux, P. In *Lithium Process Chemistry*, 2015, DOI:10.1016/b978-0-12-801417-2.00004-9 10.1016/b978-0-12-801417-2.00004-9.

(78) Yoshino, A. In *Lithium-Ion Batteries*, 2014, DOI:10.1016/b978-0-444-59513-3.00001-7 10.1016/b978-0-444-59513-3.00001-7.

(79) Mohamed, N.; Allam, N. K. Recent advances in the design of cathode materials for Li-ion batteries. *RSC Advances* **2020,** *10* (37), 21662.

(80) Nitta, N.; Wu, F.; Lee, J. T.; Yushin, G. Li-ion battery materials: present and future. *Materials today* **2015,** *18* (5), 252.

(81) Ni, E.; Uematsu, S.; Quan, Z.; Sonoyama, N. Improved electrochemical property of nanoparticle polyoxovanadate K7NiV13O38 as cathode material for lithium battery. *Journal of Nanoparticle Research* **2013,** *15* (6).

(82) Sonoyama, N.; Suganuma, Y.; Kume, T.; Quan, Z. Lithium intercalation reaction into the Keggin type polyoxomolybdates. *Journal of Power Sources* **2011,** *196* (16), 6822.

(83) Ni, E.; Uematsu, S.; Sonoyama, N. Lithium intercalation into the polyoxovanadate K7MnV13O38 as cathode material of lithium ion batteries. *Solid State Ionics* **2014,** *268*, 222.

(84) Ni, E.; Uematsu, S.; Tsukada, T.; Sonoyama, N. Lithium intercalation into polyoxomolybdate (NH4)6[NiMo9O32] as the cathode material of lithium battery. *Solid State Ionics* **2016,** *285*, 83.

(85) Kawasaki, N.; Wang, H.; Nakanishi, R.; Hamanaka, S.; Kitaura, R.; Shinohara, H.; Yokoyama, T.; Yoshikawa, H.; Awaga, K. Nanohybridization of polyoxometalate clusters and single-wall carbon nanotubes: applications in molecular cluster batteries. *Angew Chem Int Ed Engl* **2011,** *50* (15), 3471.

(86) Chen, W.; Huang, L.; Hu, J.; Li, T.; Jia, F.; Song, Y. F. Connecting carbon nanotubes to polyoxometalate clusters for engineering high-performance anode materials. *Phys Chem Chem Phys* **2014,** *16* (36), 19668.

(87) Lira-Cantú, M.; Gómez-Romero, P. Cation vs. anion insertion in hybrid materials based on conducting organic polymers for energy storage applications. *Ionics* **1997,** *3* (3-4), 194.

(88) Lira-Cantú, M.; Gómez-Romero, P. Electrochemical and Chemical Syntheses of the Hybrid Organic− Inorganic Electroactive Material Formed by Phosphomolybdate and Polyaniline. Application as Cation-Insertion Electrodes. *Chemistry of materials* **1998,** *10* (3), 698.

(89) Uematsu, S.; Quan, Z.; Suganuma, Y.; Sonoyama, N. Reversible lithium charge–discharge property of bi-capped Keggin-type polyoxovanadates. *Journal of Power Sources* **2012,** *217*, 13.

(90) Wang, H.; Hamanaka, S.; Nishimoto, Y.; Irle, S.; Yokoyama, T.; Yoshikawa, H.; Awaga, K. In operando X-ray absorption fine structure studies of polyoxometalate molecular cluster batteries: polyoxometalates as electron sponges. *J Am Chem Soc* **2012,** *134* (10), 4918.

(91) Ni, E.; Uematsu, S.; Sonoyama, N. Anderson type polyoxomolybdate as cathode material of lithium battery and its reaction mechanism. *Journal of Power Sources* **2014,** *267*, 673.

(92) Chen, J. J.; Symes, M. D.; Fan, S. C.; Zheng, M. S.; Miras, H. N.; Dong, Q. F.; Cronin, L. High-Performance Polyoxometalate-Based Cathode Materials for Rechargeable Lithium-Ion Batteries. *Adv Mater* **2015,** *27* (31), 4649.

(93) Li, W.-l.; Ni, E.-f.; Li, X.-h.; Guo, H.-j. Polyoxovanadate (NH4) 7 [MnV13O38] as cathode material for lithium ion battery and improved electrochemical performance. *Transactions of Nonferrous Metals Society of China* **2016,** *26* (9), 2372.

(94) Ni, E.; Tsukada, T.; Wen, Q.; Sonoyama, N. Improved Performance of Nano-Sized Polyoxometalate as Lithium-Battery Cathode by Conductive Polymer Coating. *Journal of The Electrochemical Society* **2018,** *166* (3), A5226.

(95) Chen, J.-J.; Ye, J.-C.; Zhang, X.-G.; Symes, M. D.; Fan, S.-C.; Long, D.-L.; Zheng, M.-S.; Wu, D.-Y.; Cronin, L.; Dong, Q.-F. Design and Performance of Rechargeable Sodium Ion Batteries, and Symmetrical Li-Ion Batteries with Supercapacitor-Like Power Density Based upon Polyoxovanadates. *Advanced Energy Materials* **2018,** *8* (6).

(96) Huang, S.-C.; Lin, C.-C.; Hu, C.-W.; Liao, Y.-F.; Chen, T.-Y.; Chen, H.-Y. Vanadium-based polyoxometalate as electron/ion sponge for lithium-ion storage. *Journal of Power Sources* **2019,** *435*.

(97) Genovese, M.; Lian, K. Polyoxometalate modified inorganic–organic nanocomposite materials for energy storage applications: A review. *Current Opinion in Solid State and Materials Science* **2015,** *19* (2), 126.

(98) Ma, D.; Liang, L.; Chen, W.; Liu, H.; Song, Y.-F. Covalently Tethered Polyoxometalate-Pyrene Hybrids for Noncovalent Sidewall Functionalization of Single-Walled Carbon Nanotubes as High-Performance Anode Material. *Advanced Functional Materials* **2013,** *23* (48), 6100.

(99) Hu, J.; Jia, F.; Song, Y.-F. Engineering high-performance polyoxometalate/PANI/MWNTs nanocomposite anode materials for lithium ion batteries. *Chemical Engineering Journal* **2017,** *326*, 273.

(100) Wang, S.; Li, H.; Li, S.; Liu, F.; Wu, D.; Feng, X.; Wu, L. Electrochemical-reduction-assisted assembly of a polyoxometalate/graphene nanocomposite and its enhanced lithium-storage performance. *Chemistry* **2013,** *19* (33), 10895.

(101) Xie, J.; Zhang, Y.; Han, Y.; Li, C. High-Capacity Molecular Scale Conversion Anode Enabled by Hybridizing Cluster-Type Framework of High Loading with Amino-Functionalized Graphene. *ACS Nano* **2016,** *10* (5), 5304.

(102) Lin, C. G.; Hu, J.; Song, Y. F. In *Polyoxometalate Chemistry*, 2017, DOI:10.1016/bs.adioch.2016.12.004 10.1016/bs.adioch.2016.12.004.

(103) Kume, K.; Kawasaki, N.; Wang, H.; Yamada, T.; Yoshikawa, H.; Awaga, K. Enhanced capacitor effects in polyoxometalate/graphene nanohybrid materials: a synergetic approach to high performance energy storage. *J. Mater. Chem. A* **2014,** *2* (11), 3801.

(104) Ni, L.; Yang, G.; Sun, C.; Niu, G.; Wu, Z.; Chen, C.; Gong, X.; Zhou, C.; Zhao, G.; Gu, J.et al. Self-assembled three-dimensional graphene/polyaniline/polyoxometalate hybrid as cathode for improved rechargeable lithium ion batteries. *Materials Today Energy* **2017,** *6*, 53.

(105) Huang, Q.; Wei, T.; Zhang, M.; Dong, L.-Z.; Zhang, A. M.; Li, S.-L.; Liu, W.-J.; Liu, J.; Lan, Y.-Q. A highly stable polyoxometalate-based metal–organic framework with π–π stacking for enhancing lithium ion battery performance. *Journal of Materials Chemistry A* **2017,** *5* (18), 8477.

(106) Li, X.; Zhou, K. F.; Tong, Z. B.; Yang, X. Y.; Chen, C. Y.; Shang, X. H.; Sha, J. Q. Heightened Integration of POM-based Metal-Organic Frameworks with Functionalized Single-Walled Carbon Nanotubes for Superior Energy Storage. *Chem Asian J* **2019**, DOI:10.1002/asia.201901143 10.1002/asia.201901143.

(107) Wang, Y. Y.; Zhang, M.; Li, S. L.; Zhang, S. R.; Xie, W.; Qin, J. S.; Su, Z. M.; Lan, Y. Q. Diamondoid-structured polymolybdate-based metal-organic frameworks as high-capacity anodes for lithium-ion batteries. *Chem Commun (Camb)* **2017,** *53* (37), 5204.

(108) Wei, T.; Zhang, M.; Wu, P.; Tang, Y.-J.; Li, S.-L.; Shen, F.-C.; Wang, X.-L.; Zhou, X.-P.; Lan, Y.-Q. POM-based metal-organic framework/reduced graphene oxide nanocomposites with hybrid behavior of battery-supercapacitor for superior lithium storage. *Nano Energy* **2017,** *34*, 205.

(109) Xia, S.; Li, F.; Li, X.; Cheng, F.; Sun, C.; Liu, J. J.; Guo, H. An inorganic-organic hybrid supramolecular framework as a high-performance anode for lithium-ion batteries. *Dalton Trans* **2018,** *47* (15), 5166.

(110) Yue, Y.; Li, Y.; Bi, Z.; Veith, G. M.; Bridges, C. A.; Guo, B.; Chen, J.; Mullins, D. R.; Surwade, S. P.; Mahurin, S. M.et al. A POM–organic framework anode for Li-ion battery. *Journal of Materials Chemistry A* **2015,** *3* (45), 22989.

(111) Zhang, M.; Zhang, A. M.; Wang, X.-X.; Huang, Q.; Zhu, X.; Wang, X.-L.; Dong, L.-Z.; Li, S.-L.; Lan, Y.-Q. Encapsulating ionic liquids into POM-based MOFs to improve their conductivity for superior lithium storage. *Journal of Materials Chemistry A* **2018,** *6* (18), 8735.

(112) Hartung, S.; Bucher, N.; Chen, H.-Y.; Al-Oweini, R.; Sreejith, S.; Borah, P.; Yanli, Z.; Kortz, U.; Stimming, U.; Hoster, H. E.et al. Vanadium-based polyoxometalate as new material for sodium-ion battery anodes. *Journal of Power Sources* **2015,** *288*, 270.

(113) Liu, J.; Chen, Z.; Chen, S.; Zhang, B.; Wang, J.; Wang, H.; Tian, B.; Chen, M.; Fan, X.; Huang, Y.et al. "Electron/Ion Sponge"-Like V-Based Polyoxometalate: Toward High-Performance Cathode for Rechargeable Sodium Ion Batteries. *ACS Nano* **2017,** *11* (7), 6911.

(114) Lyu, Y.; Liu, Y.; Yu, Z.-E.; Su, N.; Liu, Y.; Li, W.; Li, Q.; Guo, B.; Liu, B. Recent advances in high energy-density cathode materials for sodium-ion batteries. *Sustainable Materials and Technologies* **2019,** *21.*

(115) Lin, C.-C.; Lin, W.-H.; Huang, S.-C.; Hu, C.-W.; Chen, T.-Y.; Hsu, C.-T.; Yang, H.; Haider, A.; Lin, Z.; Kortz, U.et al. Mechanism of Sodium Ion Storage in Na7
[H2
PV14
O42
] Anode for Sodium-Ion Batteries. *Advanced Materials Interfaces* **2018,** *5* (15).

(116) Ueda, T. Electrochemistry of polyoxometalates: from fundamental aspects to applications. *ChemElectroChem* **2018,** *5* (6), 823.

(117) Wang, W.; Luo, Q.; Li, B.; Wei, X.; Li, L.; Yang, Z. Recent progress in redox flow battery research and development. *Advanced Functional Materials* **2013,** *23* (8), 970.

(118) Yuan, X. Z.; Song, C.; Platt, A.; Zhao, N.; Wang, H.; Li, H.; Fatih, K.; Jang, D. A review of all-vanadium redox flow battery durability: Degradation mechanisms and mitigation strategies. *International Journal of Energy Research* **2019**.

(119) Ulaganathan, M.; Aravindan, V.; Yan, Q.; Madhavi, S.; Skyllas-Kazacos, M.; Lim, T. M. Recent advancements in all-vanadium redox flow batteries. *Advanced Materials Interfaces* **2016,** *3* (1), 1500309.

(120) Pan, F.; Wang, Q. Redox species of redox flow batteries: A review. *Molecules* **2015,** *20* (11), 20499.

(121) Skyllas-Kazacos, M.; Chakrabarti, M.; Hajimolana, S.; Mjalli, F.; Saleem, M. Progress in flow battery research and development. *Journal of The Electrochemical Society* **2011,** *158* (8), R55.

(122) Wei, X.; Pan, W.; Duan, W.; Hollas, A.; Yang, Z.; Li, B.; Nie, Z.; Liu, J.; Reed, D.; Wang, W. Materials and systems for organic redox flow batteries: status and challenges. *ACS Energy Letters* **2017,** *2* (9), 2187.

(123) Pratt III, H. D.; Anderson, T. M. Mixed addenda polyoxometalate "solutions" for stationary energy storage. *Dalton Transactions* **2013,** *42* (44), 15650.

(124) Pratt III, H. D.; Hudak, N. S.; Fang, X.; Anderson, T. M. A polyoxometalate flow battery. *Journal of Power Sources* **2013,** *236*, 259.

(125) Pratt III, H. D.; Pratt, W. R.; Fang, X.; Hudak, N. S.; Anderson, T. M. Mixed-metal, structural, and substitution effects of polyoxometalates on electrochemical behavior in a redox flow battery. *Electrochimica Acta* **2014,** *138*, 210.

(126) Dubal, D. P.; Gomez-Romero, P. Electroactive graphene nanofluids for fast energy storage. *2D Materials* **2016,** *3* (3), 031004.

(127) Dubal, D. P.; Rueda-Garcia, D.; Marchante, C.; Benages, R.; Gomez-Romero, P. Hybrid Graphene-Polyoxometalates Nanofluids as Liquid Electrodes for Dual Energy Storage in Novel Flow Cells. *The Chemical Record* **2018,** *18* (7-8), 1076.

(128) Li, L.; Kim, S.; Wang, W.; Vijayakumar, M.; Nie, Z.; Chen, B.; Zhang, J.; Xia, G.; Hu, J.; Graff, G. A stable vanadium redox-flow battery with high energy density for large-scale energy storage. *Advanced Energy Materials* **2011,** *1* (3), 394.

(129) Dau, H.; Limberg, C.; Reier, T.; Risch, M.; Roggan, S.; Strasser, P. The mechanism of water oxidation: from electrolysis via homogeneous to biological catalysis. *ChemCatChem* **2010,** *2* (7), 724.

(130) Eisenberg, R. Rethinking water splitting. *Science* **2009,** *324* (5923), 44.

(131) Lv, H.; Geletii, Y. V.; Zhao, C.; Vickers, J. W.; Zhu, G.; Luo, Z.; Song, J.; Lian, T.; Musaev, D. G.; Hill, C. L. Polyoxometalate water oxidation catalysts and the production of green fuel. *Chemical Society Reviews* **2012,** *41* (22), 7572.

(132) Guo, W.; Lv, H.; Chen, Z.; Sullivan, K. P.; Lauinger, S. M.; Chi, Y.; Sumliner, J. M.; Lian, T.; Hill, C. L. Self-assembly of polyoxometalates, Pt nanoparticles and metal–organic frameworks into a hybrid material for synergistic hydrogen evolution. *Journal of Materials Chemistry A* **2016,** *4* (16), 5952.

(133) Lauinger, S.; Yin, Q.; Geletii, Y.; Hill, C. In *Advances in Inorganic Chemistry*; Elsevier, 2017; Vol. 69.

(134) Hou, J.; Zhang, B.; Li, Z.; Cao, S.; Sun, Y.; Wu, Y.; Gao, Z.; Sun, L. Vertically aligned oxygenated-CoS2–MoS2 heteronanosheet architecture from polyoxometalate for efficient and stable overall water splitting. *ACS Catalysis* **2018,** *8* (5), 4612.

(135) Liang, Y.; Li, Y.; Wang, H.; Dai, H. Strongly coupled inorganic/nanocarbon hybrid materials for advanced electrocatalysis. *Journal of the American Chemical Society* **2013,** *135* (6), 2013.

(136) Katsounaros, I.; Cherevko, S.; Zeradjanin, A. R.; Mayrhofer, K. J. Oxygen electrochemistry as a cornerstone for sustainable energy conversion. *Angewandte Chemie International Edition* **2014,** *53* (1), 102.

(137) Wang, S.-S.; Yang, G.-Y. Recent advances in polyoxometalate-catalyzed reactions. *Chemical reviews* **2015,** *115* (11), 4893.

View Article Online
DOI: 10.1039/D0EE03407J

(138) Soriano-López, J.; Schmitt, W.; García-Melchor, M. Computational modelling of water oxidation catalysts. *Current Opinion in Electrochemistry* **2018,** *7*, 22.

(139) Geletii, Y. V.; Yin, Q.; Hou, Y.; Huang, Z.; Ma, H.; Song, J.; Besson, C.; Luo, Z.; Cao, R.; O'Halloran, K. P. Polyoxometalates in the design of effective and tunable water oxidation catalysts. *Israel Journal of Chemistry* **2011,** *51* (2), 238.

(140) Sartorel, A.; Carraro, M.; Scorrano, G.; Zorzi, R. D.; Geremia, S.; McDaniel, N. D.; Bernhard, S.; Bonchio, M. Polyoxometalate Embedding of a Tetraruthenium(IV)-oxo-core by Template-Directed Metalation of [γ-SiW10O36]8−: A Totally Inorganic Oxygen-Evolving Catalyst. *Journal of the American Chemical Society* **2008,** *130* (15), 5006.

(141) Geletii, Y. V.; Botar, B.; Kögerler, P.; Hillesheim, D. A.; Musaev, D. G.; Hill, C. L. An all-inorganic, stable, and highly active tetraruthenium homogeneous catalyst for water oxidation. *Angewandte Chemie International Edition* **2008,** *47* (21), 3896.

(142) Kuznetsov, A. E.; Geletii, Y. V.; Hill, C. L.; Morokuma, K.; Musaev, D. G. Dioxygen and water activation processes on multi-ru-substituted polyoxometalates: comparison with the "blue-dimer" water oxidation catalyst. *Journal of the American Chemical Society* **2009,** *131* (19), 6844.

(143) Geletii, Y. V.; Besson, C.; Hou, Y.; Yin, Q.; Musaev, D. G.; Quiñonero, D.; Cao, R.; Hardcastle, K. I.; Proust, A.; Kögerler, P. Structural, physicochemical, and reactivity properties of an all-inorganic, highly active tetraruthenium homogeneous catalyst for water oxidation. *Journal of the American Chemical Society* **2009,** *131* (47), 17360.

(144) Sartorel, A.; Miró, P.; Salvadori, E.; Romain, S.; Carraro, M.; Scorrano, G.; Valentin, M. D.; Llobet, A.; Bo, C.; Bonchio, M. Water oxidation at a tetraruthenate core stabilized by polyoxometalate ligands: experimental and computational evidence to trace the competent intermediates. *Journal of the American Chemical Society* **2009,** *131* (44), 16051.

(145) Piccinin, S.; Fabris, S. A first principles study of water oxidation catalyzed by a tetraruthenium-oxo core embedded in polyoxometalate ligands. *Physical Chemistry Chemical Physics* **2011,** *13* (17), 7666.

(146) Geletii, Y. V.; Huang, Z.; Hou, Y.; Musaev, D. G.; Lian, T.; Hill, C. L. Homogeneous light-driven water oxidation catalyzed by a tetraruthenium complex with all inorganic ligands. *Journal of the American Chemical Society* **2009,** *131* (22), 7522.

(147) Besson, C.; Huang, Z.; Geletii, Y. V.; Lense, S.; Hardcastle, K. I.; Musaev, D. G.; Lian, T.; Proust, A.; Hill, C. L. Cs 9 [(γ-PW 10 O 36) 2 Ru 4 O 5 (OH)(H 2 O) 4], a new all-inorganic, soluble catalyst for the efficient visible-light-driven oxidation of water. *Chemical Communications* **2010,** *46* (16), 2784.

(148) Orlandi, M.; Argazzi, R.; Sartorel, A.; Carraro, M.; Scorrano, G.; Bonchio, M.; Scandola, F. Ruthenium polyoxometalate water splitting catalyst: very fast hole scavenging from photogenerated oxidants. *Chemical Communications* **2010,** *46* (18), 3152.

(149) Natali, M.; Orlandi, M.; Berardi, S.; Campagna, S.; Bonchio, M.; Sartorel, A.; Scandola, F. Photoinduced water oxidation by a tetraruthenium polyoxometalate catalyst: ion-pairing and primary processes with Ru (bpy) 32+ photosensitizer. *Inorganic chemistry* **2012,** *51* (13), 7324.

(150) Puntoriero, F.; La Ganga, G.; Sartorel, A.; Carraro, M.; Scorrano, G.; Bonchio, M.; Campagna, S. Photo-induced water oxidation with tetra-nuclear ruthenium sensitizer and catalyst: a unique 4× 4 ruthenium interplay triggering high efficiency with low-energy visible light. *Chemical Communications* **2010,** *46* (26), 4725.

(151) Natali, M.; Puntoriero, F.; Chiorboli, C.; La Ganga, G.; Sartorel, A.; Bonchio, M.; Campagna, S.; Scandola, F. Working the other way around: Photocatalytic water oxidation triggered by reductive quenching of the photoexcited chromophore. *The Journal of Physical Chemistry C* **2015,** *119* (5), 2371.

(152) Bonchio, M.; Syrgiannis, Z.; Burian, M.; Marino, N.; Pizzolato, E.; Dirian, K.; Rigodanza, F.; Volpato, G. A.; La Ganga, G.; Demitri, N. Hierarchical organization of perylene bisimides and polyoxometalates for photo-assisted water oxidation. *Nature chemistry* **2019,** *11* (2), 146.

(153) Xiang, X.; Fielden, J.; Rodríguez-Córdoba, W.; Huang, Z.; Zhang, N.; Luo, Z.; Musaev, D. G.; Lian, T.; Hill, C. L. Electron transfer dynamics in semiconductor–chromophore–polyoxometalate catalyst photoanodes. *The Journal of Physical Chemistry C* **2013,** *117* (2), 918.

(154) Huang, Z.; Geletii, Y. V.; Wu, D.; Anfuso, C. L.; Musaev, D. G.; Hill, C. L.; Lian, T. Solar Hydrogen and Nanotechnology VI, 2011; p 810903.

(155) Fielden, J.; Sumliner, J. M.; Han, N.; Geletii, Y. V.; Xiang, X.; Musaev, D. G.; Lian, T.; Hill, C. L. Water splitting with polyoxometalate-treated photoanodes: enhancing performance through sensitizer design. *Chemical science* **2015,** *6* (10), 5531.

(156) Lauinger, S. M.; Sumliner, J. M.; Yin, Q.; Xu, Z.; Liang, G.; Glass, E. N.; Lian, T.; Hill, C. L. High stability of immobilized polyoxometalates on TiO2 nanoparticles and nanoporous films for robust, light-induced water oxidation. *Chemistry of Materials* **2015,** *27* (17), 5886.

(157) Lauinger, S. M.; Piercy, B. D.; Li, W.; Yin, Q.; Collins-Wildman, D. L.; Glass, E. N.; Losego, M. D.; Wang, D.; Geletii, Y. V.; Hill, C. L. Stabilization of polyoxometalate water oxidation catalysts on hematite by atomic layer deposition. *ACS applied materials & interfaces* **2017,** *9* (40), 35048.

(158) Jeon, D.; Kim, N.; Bae, S.; Han, Y.; Ryu, J. WO3/conducting polymer heterojunction photoanodes for efficient and stable photoelectrochemical water splitting. *ACS applied materials & interfaces* **2018,** *10* (9), 8036.

(159) Toma, F. M.; Sartorel, A.; Iurlo, M.; Carraro, M.; Parisse, P.; Maccato, C.; Rapino, S.; Gonzalez, B. R.; Amenitsch, H.; Da Ros, T. Efficient water oxidation at carbon nanotube–polyoxometalate electrocatalytic interfaces. *Nature chemistry* **2010,** *2* (10), 826.

(160) Kanan, M. W.; Nocera, D. G. In situ formation of an oxygen-evolving catalyst in neutral water containing phosphate and Co2+. *Science* **2008,** *321* (5892), 1072.

(161) Brimblecombe, R.; Swiegers, G. F.; Dismukes, G. C.; Spiccia, L. Sustained water oxidation photocatalysis by a bioinspired manganese cluster. *Angewandte Chemie International Edition* **2008,** *47* (38), 7335.

(162) Toma, F. M.; Sartorel, A.; Iurlo, M.; Carraro, M.; Rapino, S.; Hoober-Burkhardt, L.; Da Ros, T.; Marcaccio, M.; Scorrano, G.; Paolucci, F. Tailored functionalization of carbon nanotubes for electrocatalytic water splitting and sustainable energy applications. *ChemSusChem* **2011,** *4* (10), 1447.

(163) Quintana, M.; Lopez, A. M.; Rapino, S.; Toma, F. M.; Iurlo, M.; Carraro, M.; Sartorel, A.; Maccato, C.; Ke, X.; Bittencourt, C. Knitting the catalytic pattern of artificial photosynthesis to a hybrid graphene nanotexture. *ACS nano* **2013,** *7* (1), 811.

(164) Guo, S.-X.; Liu, Y.; Lee, C.-Y.; Bond, A. M.; Zhang, J.; Geletii, Y. V.; Hill, C. L. Graphene-supported [{Ru 4 O 4 (OH) 2 (H 2 O) 4}(γ-SiW 10 O 36) 2] 10− for highly efficient electrocatalytic water oxidation. *Energy & Environmental Science* **2013,** *6* (9), 2654.

(165) Anwar, N.; Sartorel, A.; Yaqub, M.; Wearen, K.; Laffir, F.; Armstrong, G.; Dickinson, C.; Bonchio, M.; McCormac, T. Surface immobilization of a tetra-ruthenium substituted polyoxometalate water oxidation catalyst through the employment of conducting polypyrrole and the layer-by-layer (LBL) technique. *ACS applied materials & interfaces* **2014,** *6* (11), 8022.

(166) Murakami, M.; Hong, D.; Suenobu, T.; Yamaguchi, S.; Ogura, T.; Fukuzumi, S. Catalytic mechanism of water oxidation with single-site ruthenium–heteropolytungstate complexes. *Journal of the American Chemical Society* **2011,** *133* (30), 11605.

(167) Lang, Z.-L.; Yang, G.-C.; Ma, N.-N.; Wen, S.-Z.; Yan, L.-K.; Guan, W.; Su, Z.-M. DFT characterization on the mechanism of water splitting catalyzed by single-Ru-substituted polyoxometalates. *Dalton Transactions* **2013,** *42* (29), 10617.

(168) Car, P.-E.; Guttentag, M.; Baldridge, K. K.; Alberto, R.; Patzke, G. R. Synthesis and characterization of open and sandwich-type polyoxometalates reveals visible-light-driven water oxidation via POM-photosensitizer complexes. *Green Chemistry* **2012,** *14* (6), 1680.

(169) Yin, Q.; Tan, J. M.; Besson, C.; Geletii, Y. V.; Musaev, D. G.; Kuznetsov, A. E.; Luo, Z.; Hardcastle, K. I.; Hill, C. L. A fast soluble carbon-free molecular water oxidation catalyst based on abundant metals. *Science* **2010,** *328* (5976), 342.

(170) Huang, Z.; Luo, Z.; Geletii, Y. V.; Vickers, J. W.; Yin, Q.; Wu, D.; Hou, Y.; Ding, Y.; Song, J.; Musaev, D. G. Efficient light-driven carbon-free cobalt-based molecular catalyst for water oxidation. *Journal of the American Chemical Society* **2011,** *133* (7), 2068.

(171) Wu, J.; Liao, L.; Yan, W.; Xue, Y.; Sun, Y.; Yan, X.; Chen, Y.; Xie, Y. Polyoxometalates immobilized in ordered mesoporous carbon nitride as highly efficient water oxidation catalysts. *ChemSusChem* **2012,** *5* (7), 1207.

(172) Stracke, J. J.; Finke, R. G. Electrocatalytic Water Oxidation Beginning with the Cobalt Polyoxometalate [Co4 (H2O) 2 (PW9O34) 2] 10–: Identification of Heterogeneous CoO x as the Dominant Catalyst. *Journal of the American Chemical Society* **2011,** *133* (38), 14872.

(173) Lieb, D.; Zahl, A.; Wilson, E. F.; Streb, C.; Nye, L. C.; Meyer, K.; Ivanović-Burmazović, I. Water exchange reactivity and stability of cobalt polyoxometalates under catalytically relevant pH conditions: insight into water oxidation catalysis. *Inorganic chemistry* **2011,** *50* (18), 9053.

(174) Natali, M.; Berardi, S.; Sartorel, A.; Bonchio, M.; Campagna, S.; Scandola, F. Is [Co 4 (H 2 O) 2 (α-PW 9 O 34) 2] 10− a genuine molecular catalyst in photochemical water oxidation? Answers from time-resolved hole scavenging experiments. *Chemical Communications* **2012,** *48* (70), 8808.

(175) Stracke, J. J.; Finke, R. G. Water oxidation catalysis beginning with 2.5 μM [Co4 (H2O) 2 (PW9O34) 2] 10–: Investigation of the true electrochemically driven catalyst at≥ 600 mV overpotential at a glassy carbon electrode. *ACS Catalysis* **2013,** *3* (6), 1209.

(176) Schiwon, R.; Klingan, K.; Dau, H.; Limberg, C. Shining light on integrity of a tetracobalt-polyoxometalate water oxidation catalyst by X-ray spectroscopy before and after catalysis. *Chemical communications* **2014,** *50* (1), 100.

(177) Stracke, J. J.; Finke, R. G. Water Oxidation Catalysis Beginning with Co4 (H2O) 2 (PW9O34) 210–When Driven by the Chemical Oxidant Ruthenium (III) tris (2, 2′-bipyridine): Stoichiometry, Kinetic, and Mechanistic Studies en Route to Identifying the True Catalyst. *ACS Catalysis* **2014,** *4* (1), 79.

(178) Vickers, J. W.; Lv, H.; Sumliner, J. M.; Zhu, G.; Luo, Z.; Musaev, D. G.; Geletii, Y. V.; Hill, C. L. Differentiating homogeneous and heterogeneous water oxidation catalysis: Confirmation that [Co4 (H2O) 2 (α-PW9O34) 2] 10–is a molecular water oxidation catalyst. *Journal of the American Chemical Society* **2013,** *135* (38), 14110.

(179) Stracke, J. J.; Finke, R. G. Distinguishing homogeneous from heterogeneous water oxidation catalysis when beginning with polyoxometalates. *ACS Catalysis* **2014,** *4* (3), 909.

(180) Folkman, S. J.; Soriano-Lopez, J.; Galán-Mascarós, J. R. n.; Finke, R. G. Electrochemically Driven Water-Oxidation Catalysis Beginning with Six Exemplary Cobalt Polyoxometalates: Is It Molecular, Homogeneous Catalysis or Electrode-Bound, Heterogeneous CoO x Catalysis? *Journal of the American Chemical Society* **2018,** *140* (38), 12040.

(181) Li, J.; Güttinger, R.; Moré, R.; Song, F.; Wan, W.; Patzke, G. R. Frontiers of water oxidation: the quest for true catalysts. *Chemical Society Reviews* **2017,** *46* (20), 6124.

(182) Han, J.; Wang, D.; Du, Y.; Xi, S.; Chen, Z.; Yin, S.; Zhou, T.; Xu, R. Polyoxometalate immobilized in MIL-101 (Cr) as an efficient catalyst for water oxidation. *Applied Catalysis A: General* **2016,** *521*, 83.

(183) Paille, G.; Gomez-Mingot, M.; Roch-Marchal, C.; Lassalle-Kaiser, B.; Mialane, P.; Fontecave, M.; Mellot-Draznieks, C.; Dolbecq, A. A fully noble metal-free photosystem

View Article Online
DOI: 10.1039/D0EE03407J

based on cobalt-polyoxometalates immobilized in a porphyrinic metal–organic framework for water oxidation. *Journal of the American Chemical Society* **2018,** *140* (10), 3613.

(184) Lee, C.; Jeon, D.; Bae, S.; Kim, H.; Han, Y.; Lee, Y. W.; Ryu, J. Semiconducting Synthetic Melanin-Based Organic/Inorganic Hybrid Photoanodes for Solar Water Oxidation. *ChemSusChem* **2018,** *11* (19), 3534.

(185) Jeon, D.; Kim, H.; Lee, C.; Han, Y.; Gu, M.; Kim, B.-S.; Ryu, J. Layer-by-layer assembly of polyoxometalates for photoelectrochemical (PEC) water splitting: toward modular PEC devices. *ACS applied materials & interfaces* **2017,** *9* (46), 40151.

(186) Fang, W.; Tao, R.; Jin, Z.; Sun, Z.; Li, F.; Xu, L. Sandwich-type cobalt-polyoxometalate as an effective hole extraction layer for enhancing BiVO4-based photoelectrochemical oxidation. *Journal of Alloys and Compounds* **2019,** *797*, 140.

(187) Zhu, G.; Geletii, Y. V.; Kögerler, P.; Schilder, H.; Song, J.; Lense, S.; Zhao, C.; Hardcastle, K. I.; Musaev, D. G.; Hill, C. L. Water oxidation catalyzed by a new tetracobalt-substituted polyoxometalate complex:[{Co4 (μ-OH)(H2O) 3}(Si2W19O70)] 11−. *Dalton transactions* **2012,** *41* (7), 2084.

(188) Lv, H.; Song, J.; Geletii, Y. V.; Vickers, J. W.; Sumliner, J. M.; Musaev, D. G.; Kögerler, P.; Zhuk, P. F.; Bacsa, J.; Zhu, G. An exceptionally fast homogeneous carbon-free cobalt-based water oxidation catalyst. *Journal of the American Chemical Society* **2014,** *136* (26), 9268.

(189) Folkman, S. J.; Kirner, J. T.; Finke, R. G. Cobalt Polyoxometalate Co4V2W18O6810–: A Critical Investigation of Its Synthesis, Purity, and Observed 51V Quadrupolar NMR. *Inorganic chemistry* **2016,** *55* (11), 5343.

(190) Folkman, S. J.; Finke, R. G. Electrochemical water oxidation catalysis beginning with Co (II) polyoxometalates: The case of the precatalyst Co4V2W18O6810–. *ACS Catalysis* **2017,** *7* (1), 7.

(191) Sullivan, K. P.; Wieliczko, M.; Kim, M.; Yin, Q.; Collins-Wildman, D. L.; Mehta, A. K.; Bacsa, J.; Lu, X.; Geletii, Y. V.; Hill, C. L. Speciation and Dynamics in the [Co4V2W18O68] 10–/Co (II) aq/CoO x Catalytic Water Oxidation System. *ACS Catalysis* **2018,** *8* (12), 11952.

(192) Soriano-López, J.; Musaev, D. G.; Hill, C. L.; Galán-Mascarós, J. R.; Carbó, J. J.; Poblet, J. M. Tetracobalt-polyoxometalate catalysts for water oxidation: key mechanistic details. *Journal of Catalysis* **2017,** *350*, 56.

(193) Liu, B.; Glass, E. N.; Wang, R.-P.; Cui, Y.-T.; Harada, Y.; Huang, D.-J.; Schuppler, S.; Hill, C. L.; de Groot, F. M. Cobalt-to-vanadium charge transfer in polyoxometalate water oxidation catalysts revealed by 2p3d resonant inelastic X-ray scattering. *Physical Chemistry Chemical Physics* **2018,** *20* (6), 4554.

(194) Martin-Sabi, M.; Soriano-López, J.; Winter, R. S.; Chen, J.-J.; Vilà-Nadal, L.; Long, D.-L.; Galán-Mascarós, J. R.; Cronin, L. Redox tuning the Weakley-type polyoxometalate archetype for the oxygen evolution reaction. *Nature catalysis* **2018,** *1* (3), 208.

(195) Goberna-Ferrón, S.; Vigara, L.; Soriano-Lopez, J.; Galán-Mascarós, J. R. n. Identification of a nonanuclear {CoII9} polyoxometalate cluster as a homogeneous catalyst for water oxidation. *Inorganic chemistry* **2012,** *51* (21), 11707.

(196) Goberna-Ferrón, S.; Soriano-López, J.; Galán-Mascarós, J. R.; Nyman, M. Solution speciation and stability of cobalt-polyoxometalate water oxidation catalysts by X-ray scattering. *European Journal of Inorganic Chemistry* **2015,** *2015* (17), 2833.

(197) Soriano-López, J.; Goberna-Ferrón, S.; Vigara, L.; Carbo, J. J.; Poblet, J. M.; Galán-Mascarós, J. R. n. Cobalt polyoxometalates as heterogeneous water oxidation catalysts. *Inorganic chemistry* **2013,** *52* (9), 4753.

(198) Blasco-Ahicart, M.; Soriano-López, J.; Carbó, J. J.; Poblet, J. M.; Galan-Mascaros, J.-R. Polyoxometalate electrocatalysts based on earth-abundant metals for efficient water oxidation in acidic media. *Nature Chemistry* **2018,** *10* (1), 24.

(199) Arens, J.; Blasco-Ahicart, M.; Azmani, K.; Soriano-López, J.; García-Eguizábal, A.; Poblet, J.; Galan-Mascaros, J. Water oxidation electrocatalysis in acidic media with Co-containing polyoxometalates. *Journal of Catalysis* **2020,** *389*, 345.

(200) Blasco-Ahicart, M.; Soriano-López, J.; Galán-Mascarós, J. R. Conducting organic polymer electrodes with embedded polyoxometalate catalysts for water splitting. *ChemElectroChem* **2017,** *4* (12), 3296.

(201) Yang, C.-j. Polyoxometalate/lead composite anode for efficient oxygen evolution in zinc electrowinning. *Journal of The Electrochemical Society* **2019,** *166* (4), E129.

(202) Soriano-López, J.; Song, F.; Patzke, G. R.; Galan-Mascaros, J. R. Photoinduced oxygen evolution catalysis promoted by polyoxometalate salts of cationic photosensitizers. *Frontiers in chemistry* **2018,** *6*, 302.

(203) Han, X.-B.; Zhang, Z.-M.; Zhang, T.; Li, Y.-G.; Lin, W.; You, W.; Su, Z.-M.; Wang, E.-B. Polyoxometalate-based cobalt–phosphate molecular catalysts for visible light-driven water oxidation. *Journal of the American Chemical Society* **2014,** *136* (14), 5359.

(204) Natali, M.; Bazzan, I.; Goberna-Ferrón, S.; Al-Oweini, R.; Ibrahim, M.; Bassil, B.; Dau, H.; Scandola, F.; Galán-Mascarós, J.; Kortz, U. Photo-assisted water oxidation by high-nuclearity cobalt-oxo cores: tracing the catalyst fate during oxygen evolution turnover. *Green Chemistry* **2017,** *19* (10), 2416.

(205) Wei, J.; Feng, Y.; Zhou, P.; Liu, Y.; Xu, J.; Xiang, R.; Ding, Y.; Zhao, C.; Fan, L.; Hu, C. A bioinspired molecular polyoxometalate catalyst with two cobalt (II) oxide cores for photocatalytic water oxidation. *ChemSusChem* **2015,** *8* (16), 2630.

(206) Zhang, C.; Lin, X.; Zhang, Z.; Long, L.-S.; Wang, C.; Lin, W. A hybrid polyoxometalate–organic molecular catalyst for visible light driven water oxidation. *Chemical Communications* **2014,** *50* (78), 11591.

(207) Chen, W.-C.; Wang, X.-L.; Qin, C.; Shao, K.-Z.; Su, Z.-M.; Wang, E.-B. A carbon-free polyoxometalate molecular catalyst with a cobalt–arsenic core for visible light-driven water oxidation. *Chemical Communications* **2016,** *52* (61), 9514.

(208) Gong, L.; Yu, L.; Yu, K.; Ding, Y.; Lv, J.; Wang, C.; Su, Z.; Zhou, B. Efficient visible light-driven water oxidation catalysts based on B-β-{BiW 8 O 30} and unique 14-nuclear hetero-metal sandwich unit. *Chemical communications* **2018,** *54* (6), 674.

(209) Tanaka, S.; Annaka, M.; Sakai, K. Visible light-induced water oxidation catalyzed by molybdenum-based polyoxometalates with mono-and dicobalt (III) cores as oxygen-evolving centers. *Chemical Communications* **2012,** *48* (11), 1653.

(210) Evangelisti, F.; Car, P.-E.; Blacque, O.; Patzke, G. R. Photocatalytic water oxidation with cobalt-containing tungstobismutates: tuning the metal core. *Catalysis Science & Technology* **2013,** *3* (12), 3117.

(211) Song, F.; Ding, Y.; Ma, B.; Wang, C.; Wang, Q.; Du, X.; Fu, S.; Song, J. K 7 [Co III Co II (H 2 O) W 11 O 39]: a molecular mixed-valence Keggin polyoxometalate catalyst of high stability and efficiency for visible light-driven water oxidation. *Energy & Environmental Science* **2013,** *6* (4), 1170.

(212) Zhao, J.; Ding, Y.; Wei, J.; Du, X.; Yu, Y.; Han, R. A molecular Keggin polyoxometalate catalyst with high efficiency for visible-light driven hydrogen evolution. *International journal of hydrogen energy* **2014,** *39* (33), 18908.

(213) Xiang, R.; Ding, Y.; Zhao, J. Visible-Light-Induced Water Oxidation Mediated by a Mononuclear-Cobalt (II)-Substituted Silicotungstate. *Chemistry–An Asian Journal* **2014,** *9* (11), 3228.

(214) Singh, A.; Spiccia, L. Water oxidation catalysts based on abundant 1st row transition metals. *Coordination Chemistry Reviews* **2013,** *257* (17-18), 2607.

(215) Zaharieva, I.; Chernev, P.; Risch, M.; Klingan, K.; Kohlhoff, M.; Fischer, A.; Dau, H. Electrosynthesis, functional, and structural characterization of a water-oxidizing manganese oxide. *Energy & Environmental Science* **2012,** *5* (5), 7081.

View Article Online
DOI: 10.1039/D0EE03407J

(216) Al-Oweini, R.; Sartorel, A.; Bassil, B. S.; Natali, M.; Berardi, S.; Scandola, F.; Kortz, U.; Bonchio, M. Photocatalytic Water Oxidation by a Mixed-Valent MnIII3MnIVO3 Manganese Oxo Core that Mimics the Natural Oxygen-Evolving Center. *Angewandte Chemie International Edition* **2014,** *53* (42), 11182.

(217) Schwarz, B.; Forster, J.; Goetz, M. K.; Yuecel, D.; Berger, C.; Jacob, T.; Streb, C. Visible-Light-Driven Water Oxidation by a Molecular Manganese Vanadium Oxide Cluster. *Angewandte Chemie International Edition* **2016,** *55* (21), 6329.

(218) Yu, L.; Ding, Y.; Zheng, M. Polyoxometalate-based manganese clusters as catalysts for efficient photocatalytic and electrochemical water oxidation. *Applied Catalysis B: Environmental* **2017,** *209*, 45.

(219) Goberna-Ferrón, S.; Soriano-López, J.; Galán-Mascarós, J. R. Activity and Stability of the Tetramanganese Polyanion [Mn4 (H2O) 2 (PW9O34) 2] 10—during Electrocatalytic Water Oxidation. *Inorganics* **2015,** *3* (3), 332.

(220) Xing, X.; Wang, M.; Liu, R.; Zhang, S.; Zhang, K.; Li, B.; Zhang, G. Highly efficient electrochemically driven water oxidation by graphene-supported mixed-valent Mn16-containing polyoxometalate. *Green Energy & Environment* **2016,** *1* (2), 138.

(221) Du, Y.; Yu, T.; Fu, Z.; Bi, L. A multilayer assembly of two mixed-valence Mn16-containing polyanions and study of their electrocatalytic activities towards water oxidation. *Dalton Transactions* **2018,** *47* (21), 7282.

(222) Teillout, A.-L.; De Oliveira, P.; Marrot, J.; Howell, R. C.; Vilà, N.; Walcarius, A.; Mbomekallé, I. M. Synthesis, Crystal Structure, Electrochemistry and Electro-Catalytic Properties of the Manganese-Containing Polyoxotungstate,[(Mn (H2O) 3) 2 (H2W12O42)] 6−. *Inorganics* **2019,** *7* (2), 15.

(223) Zhu, G.; Glass, E. N.; Zhao, C.; Lv, H.; Vickers, J. W.; Geletii, Y. V.; Musaev, D. G.; Song, J.; Hill, C. L. A nickel containing polyoxometalate water oxidation catalyst. *Dalton Transactions* **2012,** *41* (42), 13043.

(224) Han, X.-B.; Li, Y.-G.; Zhang, Z.-M.; Tan, H.-Q.; Lu, Y.; Wang, E.-B. Polyoxometalate-based nickel clusters as visible light-driven water oxidation catalysts. *Journal of the American Chemical Society* **2015,** *137* (16), 5486.

(225) Yu, L.; Ding, Y.; Zheng, M.; Chen, H.; Zhao, J. [{β-SiNi2W10O36 (OH) 2 (H2O)} 4] 24−: a new robust visible light-driven water oxidation catalyst based on nickel-containing polyoxometalate. *Chemical Communications* **2016,** *52* (100), 14494.

(226) Singh, C.; Mukhopadhyay, S.; Das, S. K. Polyoxometalate-Supported Bis (2, 2′-bipyridine) mono (aqua) nickel (II) Coordination Complex: an Efficient Electrocatalyst for Water Oxidation. *Inorganic chemistry* **2018,** *57* (11), 6479.

(227) Cao, R.; Ma, H.; Geletii, Y. V.; Hardcastle, K. I.; Hill, C. L. Structurally characterized iridium (III)-containing polytungstate and catalytic water oxidation activity. *Inorganic chemistry* **2009,** *48* (13), 5596.

(228) Zhang, Z.; Lin, Q.; Kurunthu, D.; Wu, T.; Zuo, F.; Zheng, S.-T.; Bardeen, C. J.; Bu, X.; Feng, P. Synthesis and photocatalytic properties of a new heteropolyoxoniobate compound: K10 [Nb2O2 (H2O) 2][SiNb12O40]· 12H2O. *Journal of the American Chemical Society* **2011,** *133* (18), 6934.

(229) Gao, J.; Cao, S.; Tay, Q.; Liu, Y.; Yu, L.; Ye, K.; Mun, P. C. S.; Li, Y.; Rakesh, G.; Loo, S. C. J. Molecule-based water-oxidation catalysts (WOCs): Cluster-size-dependent dye-sensitized polyoxometalates for visible-light-driven O 2 evolution. *Scientific reports* **2013,** *3*, 1853.

(230) Cui, Y.; Shi, L.; Yang, Y.; You, W.; Zhang, L.; Zhu, Z.; Liu, M.; Sun, L. Catalytic water oxidation based on Ag (I)-substituted Keggin polyoxotungstophosphate. *Dalton Transactions* **2014,** *43* (46), 17406.

(231) Cui, C.; Shi, D.; Nie, Z.; Song, L.; Ren, A.; Liu, C. A Novel Ag (I)-Containing Polyoxometalate-Based MOF for Visible-Light-Driven Water Oxidation. *Journal of Cluster Science* **2019**, 1.

(232) Santoni, M.-P.; La Ganga, G.; Mollica Nardo, V.; Natali, M.; Puntoriero, F.; Scandola, F.; Campagna, S. The use of a vanadium species as a catalyst in photoinduced water oxidation. *Journal of the American Chemical Society* **2014,** *136* (23), 8189.

(233) Berardi, S.; La Ganga, G.; Natali, M.; Bazzan, I.; Puntoriero, F.; Sartorel, A.; Scandola, F.; Campagna, S.; Bonchio, M. Photocatalytic water oxidation: tuning light-induced electron transfer by molecular Co4O4 cores. *Journal of the American Chemical Society* **2012,** *134* (27), 11104.

(234) Du, X.; Ding, Y.; Song, F.; Ma, B.; Zhao, J.; Song, J. Efficient photocatalytic water oxidation catalyzed by polyoxometalate [Fe 11 (H 2 O) 14 (OH) 2 (W 3 O 10) 2 (α-SbW 9 O 33) 6] 27− based on abundant metals. *Chemical Communications* **2015,** *51* (73), 13925.

(235) Xiaoqiang, D.; Zhoufeng, X.; Yaqiong, G.; Yong, D. Polyoxometalate-based catalysts for photocatalytic, chemical catalytic and electrocatalytic water oxidation. *International Journal of Hydrogen Energy* **2017,** *42* (38), 24169.

(236) Hu, Q.; Meng, X.; Dong, Y.; Han, Q.; Wang, Y.; Ding, Y. A stable iron-containing polyoxometalate coupled with semiconductor for efficient photocatalytic water oxidation under acidic condition. *Chemical Communications* **2019,** *55* (78), 11778.

(237) Kaushik, R.; Sakla, R.; Jose, D. A.; Ghosh, A. Giant iron polyoxometalate that works as a catalyst for water oxidation. *New Journal of Chemistry* **2020,** *44* (9), 3764.

(238) Chakraborty, B.; Gan-Or, G.; Raula, M.; Gadot, E.; Weinstock, I. A. Design of an inherently-stable water oxidation catalyst. *Nature communications* **2018,** *9* (1), 1.

(239) Chakraborty, B.; Gan-Or, G.; Duan, Y.; Raula, M.; Weinstock, I. A. Visible-Light-Driven Water Oxidation with a Polyoxometalate-Complexed Hematite Core of 275 Iron Atoms. *Angewandte Chemie International Edition* **2019,** *58* (20), 6584.

(240) Yu, L.; Du, X.; Ding, Y.; Chen, H.; Zhou, P. Efficient visible light-driven water oxidation catalyzed by an all-inorganic copper-containing polyoxometalate. *Chemical Communications* **2015,** *51* (98), 17443.

(241) Yu, L.; Lin, J.; Zheng, M.; Chen, M.; Ding, Y. Homogeneous electrocatalytic water oxidation at neutral pH by a robust trinuclear copper (II)-substituted polyoxometalate. *Chemical communications* **2018,** *54* (4), 354.

(242) Rousseau, G.; Zhang, S.; Oms, O.; Dolbecq, A.; Marrot, J.; Liu, R.; Shang, X.; Zhang, G.; Keita, B.; Mialane, P. Sequential Synthesis of 3 d–3 d, 3 d–4 d, and 3 d–5 d Hybrid Polyoxometalates and Application to the Electrocatalytic Oxygen Reduction Reactions. *Chemistry–A European Journal* **2015,** *21* (34), 12153.

(243) Zhang, S.; Oms, O.; Hao, L.; Liu, R.; Wang, M.; Zhang, Y.; He, H.-Y.; Dolbecq, A.; Marrot, J.; Keita, B. High oxygen reduction reaction performances of cathode materials combining polyoxometalates, coordination complexes, and carboneous supports. *ACS applied materials & interfaces* **2017,** *9* (44), 38486.

(244) Fernandes, D. M.; Novais, H. C.; Bacsa, R.; Serp, P.; Bachiller-Baeza, B.; Rodríguez-Ramos, I.; Guerrero-Ruiz, A.; Freire, C. Polyoxotungstate@Carbon Nanocomposites As Oxygen Reduction Reaction (ORR) Electrocatalysts. *Langmuir* **2018,** *34* (22), 6376.

(245) Jiang, M.; Zhu, D.; Cai, J.; Zhang, H.; Zhao, X. Electrocatalytic hydrogen evolution and oxygen reduction on polyoxotungstates/graphene nanocomposite multilayers. *The Journal of Physical Chemistry C* **2014,** *118* (26), 14371.

(246) Nunes, M.; Fernandes, D. M.; Rocha, I. M.; Pereira, M. F.; Mbomekalle, I. M.; de Oliveira, P.; Freire, C. Phosphomolybdate@ Carbon-Based Nanocomposites as Electrocatalysts for Oxygen Reduction Reaction. *ChemistrySelect* **2016,** *1* (19), 6257.

(247) Zhao, S.; Zhao, X.; Zhang, H.; Li, J.; Zhu, Y. Covalent combination of polyoxometalate and graphitic carbon nitride for light-driven hydrogen peroxide production. *Nano Energy* **2017,** *35*, 405.

(248) Hsu-Yao, T.; Browne, K. P.; Honesty, N.; Tong, Y. J. Polyoxometalate-stabilized Pt nanoparticles and their electrocatalytic activities. *Physical Chemistry Chemical Physics* **2011,** *13* (16), 7433.

(249) Renzi, M.; Mignini, P.; Giuli, G.; Marassi, R.; Nobili, F. Rotating disk electrode study of Pt/Cs3HPMo11VO40 composite catalysts for performing and durable PEM fuel cells. *international journal of hydrogen energy* **2016,** *41* (26), 11163.

(250) Renzi, M.; Agostini, M.; Navarra, M.; Nobili, F. An innovative membrane-electrode assembly for efficient and durable polymer electrolyte membrane fuel cell operations. *International Journal of Hydrogen Energy* **2017,** *42* (26), 16686.

(251) Renzi, M.; D'Angelo, G.; Marassi, R.; Nobili, F. Low platinum loading cathode modified with Cs3H2PMo10V2O40 for polymer electrolyte membrane fuel cells. *Journal of Power Sources* **2016,** *327*, 11.

(252) Xin, J.; Lindenmuth, T.; Shannon, C. Electrocatalytic oxygen reduction at polyoxometalate/Au-nanoparticle hybrid thin films formed by layer-by-layer deposition. *Electrochimica acta* **2011,** *56* (24), 8884.

(253) Bao, Y.-Y.; Bi, L.-H.; Wu, L.-X. One-step synthesis and stabilization of gold nanoparticles and multilayer film assembly. *Journal of Solid State Chemistry* **2011,** *184* (3), 546.

(254) Xie, X.; Nie, Y.; Chen, S.; Ding, W.; Qi, X.; Li, L.; Wei, Z. A catalyst superior to carbon-supported-platinum for promotion of the oxygen reduction reaction: reduced-polyoxometalate supported palladium. *Journal of Materials Chemistry A* **2015,** *3* (26), 13962.

(255) Wang, D.; Lu, S. Pd/HPW-PDDA-MWCNTs as effective non-Pt electrocatalysts for oxygen reduction reaction of fuel cells. *Chemical Communications* **2010,** *46* (12), 2058.

(256) Li, J.-S.; Dong, H.-Q.; Li, S.-L.; Li, R.-H.; Dai, Z.-H.; Bao, J.-C.; Lan, Y.-Q. Polyoxometalate-assisted fabrication of the Pd nanoparticle/reduced graphene oxide nanocomposite with enhanced methanol-tolerance for the oxygen reduction reaction. *New Journal of Chemistry* **2016,** *40* (2), 914.

(257) Liu, R.; Li, S.; Yu, X.; Zhang, G.; Ma, Y.; Yao, J. Facile synthesis of a Ag nanoparticle/polyoxometalate/carbon nanotube tri-component hybrid and its activity in the electrocatalysis of oxygen reduction. *Journal of Materials Chemistry* **2011,** *21* (38), 14917.

(258) Xian, Z.; Liu, R.; Li, H.; Zhang, S.; Yang, Z.; Zheng, W.; Chen, C.; Cao, H.; Zhang, G. Photocatalytic reduction synthesis of ternary Ag nanoparticles/polyoxometalate/graphene nanohybrids and its activity in the electrocatalysis of oxygen reduction. *Journal of Cluster Science* **2016,** *27* (1), 241.

(259) Liu, R.; Yu, X.; Zhang, G.; Zhang, S.; Cao, H.; Dolbecq, A.; Mialane, P.; Keita, B.; Zhi, L. Polyoxometalate-mediated green synthesis of a 2D silver nanonet/graphene nanohybrid as a synergistic catalyst for the oxygen reduction reaction. *Journal of Materials Chemistry A* **2013,** *1* (38), 11961.

(260) Liu, R.; Xian, Z.; Zhang, S.; Chen, C.; Yang, Z.; Li, H.; Zheng, W.; Zhang, G.; Cao, H. Electrochemical-reduction-assisted assembly of ternary Ag nanoparticles/polyoxometalate/graphene nanohybrids and their activity in the electrocatalysis of oxygen reduction. *Rsc Advances* **2015,** *5* (91), 74447.

(261) Yu, S.; Wang, Y.; Zhu, H.; Wang, Z.; Han, K. Synthesis and electrocatalytic performance of phosphotungstic acid-modified Ag@ Pt/MWCNTs catalysts for oxygen reduction reaction. *Journal of Applied Electrochemistry* **2016,** *46* (9), 917.

(262) Boulatov, R. In *Fuel Cell Catalysis*, 2008.

(263) Nagai, M.; Sanpei, H.; Shirakura, M. Cobalt porphyrin–tungsten polyoxometalate anion as non-noble metal cathode catalyst in a fuel cell. *Journal of Materials Chemistry* **2012,** *22* (18), 9222.

(264) Han, H.; Cao, Z.; Zhang, Y.; Qin, J.; Song, Y. Ionic self-assembly of metalloporphyrin/heteropolyacid on multi-wall carbon nanotubes with enhanced electrocatalytic activity toward oxygen reduction reaction. *Journal of Porphyrins and Phthalocyanines* **2019,** *23* (03), 235.

(265) Liu, W.; Mu, W.; Deng, Y. High-performance liquid-catalyst fuel cell for direct biomass-into-electricity conversion. *Angewandte Chemie* **2014,** *126* (49), 13776.

(266) Liu, W.; Mu, W.; Liu, M.; Zhang, X.; Cai, H.; Deng, Y. Solar-induced direct biomass-to-electricity hybrid fuel cell using polyoxometalates as photocatalyst and charge carrier. *Nature communications* **2014,** *5* (1), 1.

(267) Wu, W.; Liu, W.; Mu, W.; Deng, Y. Polyoxymetalate liquid-catalyzed polyol fuel cell and the related photoelectrochemical reaction mechanism study. *Journal of Power Sources* **2016,** *318*, 86.

(268) Matsui, T.; Morikawa, E.; Nakada, S.; Okanishi, T.; Muroyama, H.; Hirao, Y.; Takahashi, T.; Eguchi, K. Polymer electrolyte fuel cells employing heteropolyacids as redox mediators for oxygen reduction reactions: Pt-free cathode systems. *ACS applied materials & interfaces* **2016,** *8* (28), 18119.

(269) Quéré, C.; Andrew, R.; Friedlingstein, P.; Sitch, S.; Hauck, J.; Pongratz, J.; Pickers, P.; Ivar Korsbakken, J.; Peters, G.; Canadell, J. Global carbon budget 2018. *Earth System Science Data* **2018,** *10* (4), 2141.

(270) Li, K.; Peng, B.; Peng, T. Recent advances in heterogeneous photocatalytic CO2 conversion to solar fuels. *ACS Catalysis* **2016,** *6* (11), 7485.

(271) Sohn, Y.; Huang, W.; Taghipour, F. Recent progress and perspectives in the photocatalytic CO2 reduction of Ti-oxide-based nanomaterials. *Applied Surface Science* **2017,** *396*, 1696.

(272) Qiao, J.; Liu, Y.; Hong, F.; Zhang, J. A review of catalysts for the electroreduction of carbon dioxide to produce low-carbon fuels. *Chemical Society Reviews* **2014,** *43* (2), 631.

(273) Wang, Y.-R.; Huang, Q.; He, C.-T.; Chen, Y.; Liu, J.; Shen, F.-C.; Lan, Y.-Q. Oriented electron transmission in polyoxometalate-metalloporphyrin organic framework for highly selective electroreduction of CO 2. *Nature communications* **2018,** *9* (1), 1.

(274) Li, X. H.; He, P.; Wang, T.; Zhang, X. W.; Chen, W. L.; Li, Y. G. Keggin-Type Polyoxometalate-Based ZIF-67 for Enhanced Photocatalytic Nitrogen Fixation. *ChemSusChem* **2020,** *13* (10), 2769.

(275) Wang, X.; Feng, Z.; Xiao, B.; Zhao, J.; Ma, H.; Tian, Y.; Pang, H.; Tan, L. Polyoxometalate-based metal–organic framework-derived bimetallic hybrid materials for upgraded electrochemical reduction of nitrogen. *Green Chemistry* **2020**.

(276) Voß, D.; Dietrich, R.; Stuckart, M.; Albert, J. Switchable Catalytic Polyoxometalate-Based Systems for Biomass Conversion to Carboxylic Acids. *ACS omega* **2020,** *5* (30), 19082.

(277) Liu, W.; Cui, Y.; Du, X.; Zhang, Z.; Chao, Z.; Deng, Y. High efficiency hydrogen evolution from native biomass electrolysis. *Energy & Environmental Science* **2016,** *9* (2), 467.

(278) Bukowski, A.; Esau, D.; Rafat Said, A. A.; Brandt-Talbot, A.; Albert, J. Combining Cost-Efficient Cellulose and Short-Chain Carboxylic Acid Production: The Polyoxometalate (POM)-Ionosolv Concept. *ChemPlusChem* **2020,** *85* (2), 373.

(279) Shi, H.; Wang, R.; Lou, M.; Jia, D.; Guo, Y.; Wang, X.; Huang, Y.; Sun, Z.; Wang, T.; Wang, L. A novel Pt/pyridine ionic liquid polyoxometalate/rGO tri-component hybrid and its enhanced activities for methanol electrooxidation. *Electrochimica Acta* **2019,** *294*, 93.

(280) Marinkovic, N. S.; Li, M.; Adzic, R. R. Pt-based catalysts for electrochemical oxidation of ethanol. *Topics in Current Chemistry* **2019,** *377* (3), 11.

(281) Bai, J.; Liu, D.; Yang, J.; Chen, Y. Nanocatalysts for electrocatalytic oxidation of ethanol. *ChemSusChem* **2019,** *12* (10), 2117.

(282) Fadzillah, D.; Kamarudin, S.; Zainoodin, M.; Masdar, M. Critical challenges in the system development of direct alcohol fuel cells as portable power supplies: an overview. *International Journal of Hydrogen Energy* **2019,** *44* (5), 3031.

(283) Bommineni, S.; Skoglund, M. D.; Morris, A. R.; Doskocil, E. J.; Holles, J. H. Characterization of selective oxidation catalysts from polyoxometalate precursors using ammonia adsorption microcalorimetry and methanol oxidation studies. *Applied Catalysis A: General* **2013,** *467*, 202.

(284) Wilke, T.; Barteau, M. A. Dehydration and Oxidation of Alcohols by Supported Polyoxometalates: Effects of Mono-and Multivalent Cation Exchange on Catalyst Acidity and Activity. *Industrial & Engineering Chemistry Research* **2019,** *58* (32), 14752.

(285) Wilke, T. J.; Barteau, M. A. Cation exchange effects on methanol oxidation and dehydration by supported polyoxometalates. *Journal of Catalysis* **2019,** *371*, 357.

(286) Barczuk, P. J.; Lewera, A.; Skorupska, K.; Li, C.; Kulesza, P. J. Enhancement of Activity of PtRu Nanoparticles Towards Oxidation of Ethanol by Supporting on Poly (diallyldimethylammonium)-Functionalized Carbon Nanotubes and Modification with Phosphomolybdate. *Electrocatalysis* **2011,** *2* (1), 52.

(287) Liu, Y.; Zhao, S.-F.; Guo, S.-X.; Bond, A. M.; Zhang, J.; Zhu, G.; Hill, C. L.; Geletii, Y. V. Electrooxidation of ethanol and methanol using the molecular catalyst [{Ru4O4 (OH) 2 (H2O) 4}(γ-SiW10O36) 2] 10–. *Journal of the American Chemical Society* **2016,** *138* (8), 2617.

(288) Lu, J.; Hong, L.; Yang, Y.; Xu, S.; Wang, S.; Yuan, J.; Niu, L. Phosphotungstic acid-assisted preparation of carbon nanotubes-supported uniform Pt and Pt bimetallic nanoparticles, and their enhanced catalytic activity on methanol electro-oxidation. *Journal of nanoparticle research* **2014,** *16* (1), 2162.

(289) Barczuk, P. J.; Lewera, A.; Miecznikowski, K.; Zurowski, A.; Kulesza, P. J. Enhancement of catalytic activity of platinum-based nanoparticles towards electrooxidation of ethanol through interfacial modification with heteropolymolybdates. *Journal of power sources* **2010,** *195* (9), 2507.

(290) Khadempir, S.; Ahmadpour, A.; Mosavian, M. T. H.; Ashraf, N.; Bamoharram, F. F.; Mitchell, S. G.; Jesús, M. A polyoxometalate-assisted approach for synthesis of Pd nanoparticles on graphene nanosheets: synergistic behaviour for enhanced electrocatalytic activity. *RSC Advances* **2015,** *5* (31), 24319.

(291) Li, S.; Yu, X.; Zhang, G.; Ma, Y.; Yao, J.; de Oliveira, P. Green synthesis of a Pt nanoparticle/polyoxometalate/carbon nanotube tri-component hybrid and its activity in the electrocatalysis of methanol oxidation. *Carbon* **2011,** *49* (6), 1906.

(292) Chen, W.; Wei, X.; Zhang, Y. A comparative study of tungsten-modified PtRu electrocatalysts for methanol oxidation. *International Journal of Hydrogen Energy* **2014,** *39* (13), 6995.

(293) Molinari, J. E.; Nakka, L.; Kim, T.; Wachs, I. E. Dynamic Surface Structures and Reactivity of Vanadium-Containing Molybdophosphoric Acid (H3+ x PMo12–x V x O40) Keggin Catalysts during Methanol Oxidation and Dehydration. *ACS Catalysis* **2011,** *1* (11), 1536.

(294) Khadempir, S.; Ahmadpour, A.; Mosavian, M. T. H.; Ashraf, N.; Bamoharram, F. F.; Fernández-Pacheco, R.; Jesús, M.; Mitchell, S. G. Mechanistic insights into the activation process in electrocatalytic ethanol oxidation by phosphomolybdic acid-stabilised palladium (0) nanoparticles (PdNPs@ PMo 12). *RSC advances* **2016,** *6* (7), 5359.

(295) Craig, M. J.; Coulter, G.; Dolan, E.; Soriano-López, J.; Mates-Torres, E.; Schmitt, W.; García-Melchor, M. Universal scaling relations for the rational design of molecular water oxidation catalysts with near-zero overpotential. *Nature communications* **2019,** *10* (1), 1.

(296) Ji, Y.; Huang, L.; Hu, J.; Streb, C.; Song, Y.-F. Polyoxometalate-functionalized nanocarbon materials for energy conversion, energy storage and sensor systems. *Energy & Environmental Science* **2015,** *8* (3), 776.

(297) Khan, R. N. N.; Mahmood, N.; Lv, C.; Sima, G.; Zhang, J.; Hao, J.; Hou, Y.; Wei, Y. Pristine organo-imido polyoxometalates as an anode for lithium ion batteries. *RSC advances* **2014,** *4* (15), 7374.

(298) Huang, L.; Hu, J.; Ji, Y.; Streb, C.; Song, Y. F. Pyrene-Anderson-modified CNTs as anode materials for lithium-ion batteries. *Chemistry–A European Journal* **2015,** *21* (51), 18799.

(299) Ji, Y.; Hu, J.; Huang, L.; Chen, W.; Streb, C.; Song, Y. F. Covalent attachment of Anderson-type polyoxometalates to single-walled carbon nanotubes gives enhanced performance electrodes for lithium ion batteries. *Chemistry–A European Journal* **2015,** *21* (17), 6469.

(300) Hu, J.; Ji, Y.; Chen, W.; Streb, C.; Song, Y.-F. "Wiring" redox-active polyoxometalates to carbon nanotubes using a sonication-driven periodic functionalization strategy. *Energy & Environmental Science* **2016,** *9* (3), 1095.

(301) Meng, X.; Wang, H.-N.; Zou, Y.-H.; Wang, L.-S.; Zhou, Z.-Y. Polyoxometalate-based metallogels as anode materials for lithium ion batteries. *Dalton Transactions* **2019,** *48* (28), 10422.

(302) Xia, S.; Li, F.; Li, X.; Cheng, F.; Sun, C.; Liu, J.-J.; Guo, H. An inorganic–organic hybrid supramolecular framework as a high-performance anode for lithium-ion batteries. *Dalton Transactions* **2018,** *47* (15), 5166.

(303) Eren, T.; Atar, N.; Yola, M. L.; Karimi-Maleh, H.; Çolak, A. T.; Olgun, A. Facile and green fabrication of silver nanoparticles on a polyoxometalate for Li-ion battery. *Ionics* **2015,** *21* (8), 2193.

(304) Sun, P.; Zhang, W.; Hu, X.; Yuan, L.; Huang, Y. Synthesis of hierarchical MoS 2 and its electrochemical performance as an anode material for lithium-ion batteries. *Journal of Materials Chemistry A* **2014,** *2* (10), 3498.

(305) Ihsan, M.; Wang, H.; Majid, S. R.; Yang, J.; Kennedy, S. J.; Guo, Z.; Liu, H. K. MoO2/Mo2C/C spheres as anode materials for lithium ion batteries. *Carbon* **2016,** *96*, 1200.

(306) Wang, X.; Sun, P.; Qin, J.; Wang, J.; Xiao, Y.; Cao, M. A three-dimensional porous MoP@ C hybrid as a high-capacity, long-cycle life anode material for lithium-ion batteries. *Nanoscale* **2016,** *8* (19), 10330.

(307) Xia, G.; Liu, D.; Zheng, F.; Yang, Y.; Su, J.; Chen, Q. Preparation of porous MoO 2@ C nano-octahedrons from a polyoxometalate-based metal–organic framework for highly reversible lithium storage. *Journal of Materials Chemistry A* **2016,** *4* (32), 12434.

(308) Yang, L.; Li, X.; He, S.; Du, G.; Yu, X.; Liu, J.; Gao, Q.; Hu, R.; Zhu, M. Mesoporous Mo 2 C/N-doped carbon heteronanowires as high-rate and long-life anode materials for Li-ion batteries. *Journal of Materials Chemistry A* **2016,** *4* (28), 10842.

(309) Meng, T.; Zheng, L.; Qin, J.; Zhao, D.; Cao, M. A three-dimensional hierarchically porous Mo 2 C architecture: salt-template synthesis of a robust electrocatalyst and anode material towards the hydrogen evolution reaction and lithium storage. *Journal of Materials Chemistry A* **2017,** *5* (38), 20228.

(310) Wang, P.; Tian, J.; Hu, J.; Zhou, X.; Li, C. Supernormal conversion anode consisting of high-density MoS2 bubbles wrapped in thin carbon network by self-sulfuration of polyoxometalate complex. *ACS nano* **2017,** *11* (7), 7390.

(311) Xu, Z.; Wang, T.; Kong, L.; Yao, K.; Fu, H.; Li, K.; Cao, L.; Huang, J.; Zhang, Q. MoO2@ MoS2 Nanoarchitectures for High-Loading Advanced Lithium-Ion Battery Anodes. *Particle & Particle Systems Characterization* **2017,** *34* (3), 1600223.

(312) Chen, X.; Lv, L.-P.; Sun, W.; Hu, Y.; Tao, X.; Wang, Y. Ultrasmall MoC nanoparticles embedded in 3D frameworks of nitrogen-doped porous carbon as anode materials for efficient lithium storage with pseudocapacitance. *Journal of Materials Chemistry A* **2018,** *6* (28), 13705.

(313) Wang, S.; Liu, B.; Zhi, G.; Gong, X.; Gao, Z.; Zhang, J. Relaxing volume stress and promoting active sites in vertically grown 2D layered mesoporous MoS2 (1-x) Se2x/rGO composites with enhanced capability and stability for lithium ion batteries. *Electrochimica Acta* **2018,** *268*, 424.

(314) Zhang, S.; Wang, G.; Jin, J.; Zhang, L.; Wen, Z.; Yang, J. Robust and conductive red MoSe2 for stable and fast lithium storage. *ACS nano* **2018,** *12* (4), 4010.

(315) Khenkin, A. M.; Efremenko, I.; Weiner, L.; Martin, J. M.; Neumann, R. Photochemical Reduction of Carbon Dioxide Catalyzed by a Ruthenium-Substituted Polyoxometalate. *Chemistry–A European Journal* **2010,** *16* (4), 1356.

(316) Haviv, E.; Shimon, L. J.; Neumann, R. Photochemical reduction of CO2 with visible light using a polyoxometalate as photoreductant. *Chemistry–A European Journal* **2017,** *23* (1), 92.

(317) Zhou, J.; Chen, W.; Sun, C.; Han, L.; Qin, C.; Chen, M.; Wang, X.; Wang, E.; Su, Z. Oxidative polyoxometalates modified graphitic carbon nitride for visible-light CO2 reduction. *ACS Applied Materials & Interfaces* **2017,** *9* (13), 11689.

(318) Liu, S. M.; Zhang, Z.; Li, X.; Jia, H.; Ren, M.; Liu, S. Ti-Substituted Keggin-Type Polyoxotungstate as Proton and Electron Reservoir Encaged into Metal–Organic Framework for Carbon Dioxide Photoreduction. *Advanced Materials Interfaces* **2018,** *5* (21), 1801062.

(319) Das, S.; Biswas, S.; Balaraju, T.; Barman, S.; Pochamoni, R.; Roy, S. Photochemical reduction of carbon dioxide coupled with water oxidation using various soft-oxometalate (SOM) based catalytic systems. *Journal of Materials Chemistry A* **2016,** *4* (22), 8875.

(320) Xie, S.-L.; Liu, J.; Dong, L.-Z.; Li, S.-L.; Lan, Y.-Q.; Su, Z.-M. Hetero-metallic active sites coupled with strongly reductive polyoxometalate for selective photocatalytic CO 2-to-CH 4 conversion in water. *Chemical science* **2019,** *10* (1), 185.

(321) Hu, J.; Wu, X.; Zhang, Q.; Gao, M.; Qiu, H.; Huang, K.; Feng, S.; Wang, T.; Yang, Y.; Liu, Z. Highly active PdNi/RGO/polyoxometalate nanocomposite electrocatalyst for alcohol oxidation. *Langmuir* **2018,** *34* (8), 2685.

(322) Gao, S.; Yang, X.; Wei, M.-J.; Liang, S.; Zang, H.-Y.; Tan, H.-Q.; Wang, Y.-H.; Li, Y.-G. One-step synthesis of Pt based electrocatalysts encapsulated by polyoxometalate for methanol oxidation. *New Journal of Chemistry* **2018,** *42* (1), 198.

(323) Ahmadpour, A.; Khadempir, S.; Ashraf, N.; Mitchell, S. G.; Ahangari, M. H. A one-pot route for the synthesis of Au@ Pd/PMo 12/rGO as a dual functional electrocatalyst for ethanol electro-oxidation and hydrogen evolution reaction. *RSC Advances* **2019,** *9* (64), 37537.

(324) Cui, Z.; Xing, W.; Liu, C.; Tian, D.; Zhang, H. Synthesis and characterization of H5PMo10V2O40 deposited Pt/C nanocatalysts for methanol electrooxidation. *Journal of Power Sources* **2010,** *195* (6), 1619.

(325) Sun, G.; Li, Q.; Xu, R.; Gu, J.; Ju, M.; Wang, E. Controllable fabrication of platinum nanospheres with a polyoxometalate-assisted process. *Journal of Solid State Chemistry* **2010,** *183* (11), 2609.

(326) Zoladek, S.; Rutkowska, I. A.; Kulesza, P. J. Enhancement of activity of platinum towards oxidation of ethanol by supporting on titanium dioxide containing phosphomolybdate-modified gold nanoparticles. *Applied surface science* **2011,** *257* (19), 8205.

(327) Hong, L.; Gui, Y.; Lu, J.; Hu, J.; Yuan, J.; Niu, L. High performance of polyoxometalate/PtPd nanoparticles/carbon nanotubes electrocatalysts for the methanol electrooxidation. *International journal of hydrogen energy* **2013,** *38* (25), 11074.

(328) Medetalibeyoğlu, H.; Manap, S.; Yokuş, Ö. A.; Beytur, M.; Kardaş, F.; Akyıldırım, O.; Özkan, V.; Yüksek, H.; Yola, M. L.; Atar, N. Fabrication of Pt/Pd nanoparticles/polyoxometalate/ionic liquid nanohybrid for electrocatalytic oxidation of methanol. *Journal of The Electrochemical Society* **2018,** *165* (5), F338.

(329) Çolak, A. T.; Eren, T.; Yola, M. L.; Beşli, E.; Şahin, O.; Atar, N. 3D polyoxometalate-functionalized graphene quantum dots with mono-metallic and bi-metallic nanoparticles for application in direct methanol fuel cells. *Journal of the Electrochemical Society* **2016,** *163* (10), F1237.

View Article Online
DOI: 10.1039/D0EE03407J

TOC: Polyoxometalates as anionic molecular metal oxides clusters with open frameworks and rich redox chemistry have outstanding versatility in energy conversion and storage research.

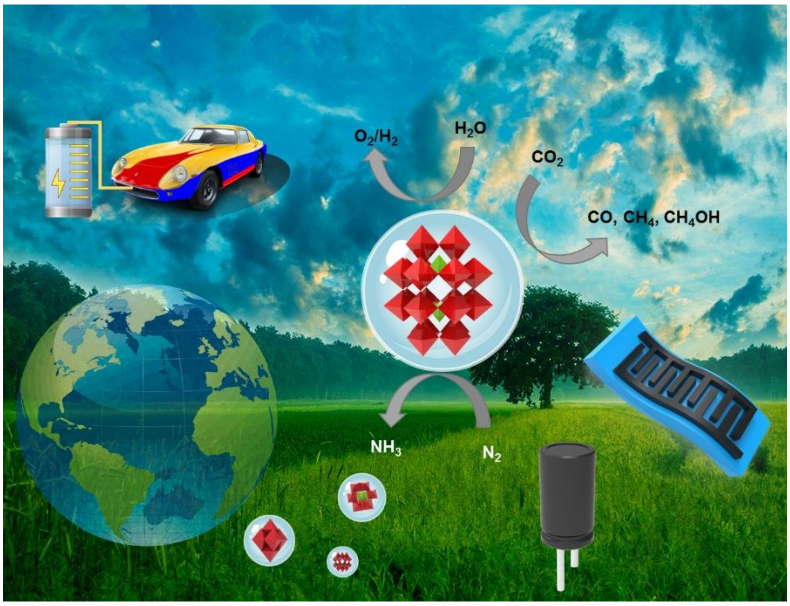

View Article Online
DOI: 10.1039/D0EE03407J

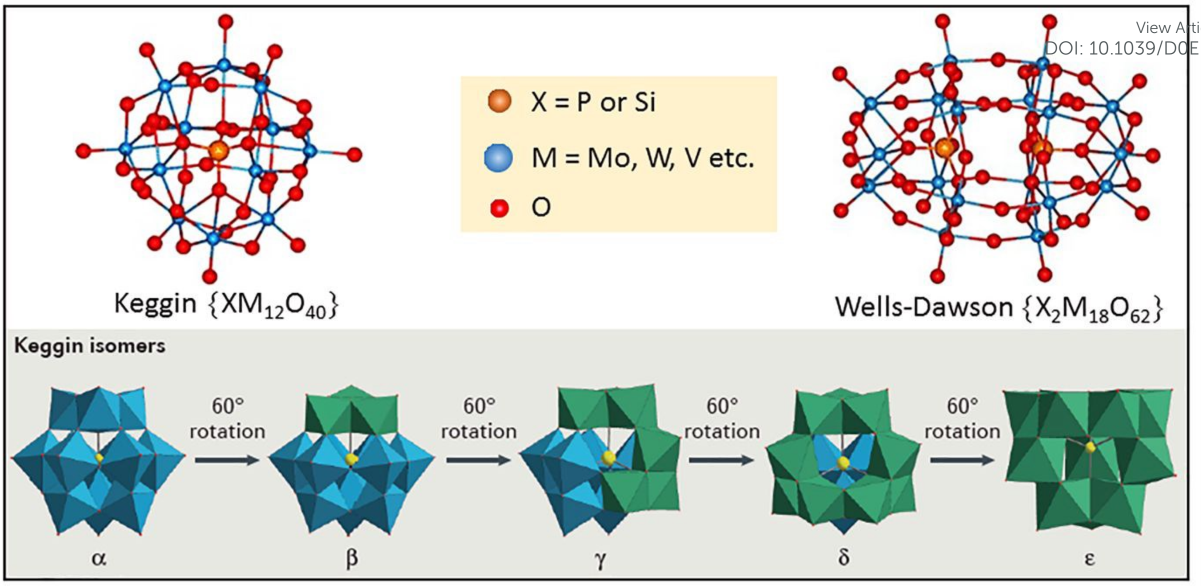

Figure 1 Keggin and Dawson POM structures including the acknowledged Keggin isomeric variations. Adapted with permission from Ref. [15], Copyright 2018, Macmillan Publishers Limited, part of Springer Nature.

View Article Online
DOI: 10.1039/D0EE03407J

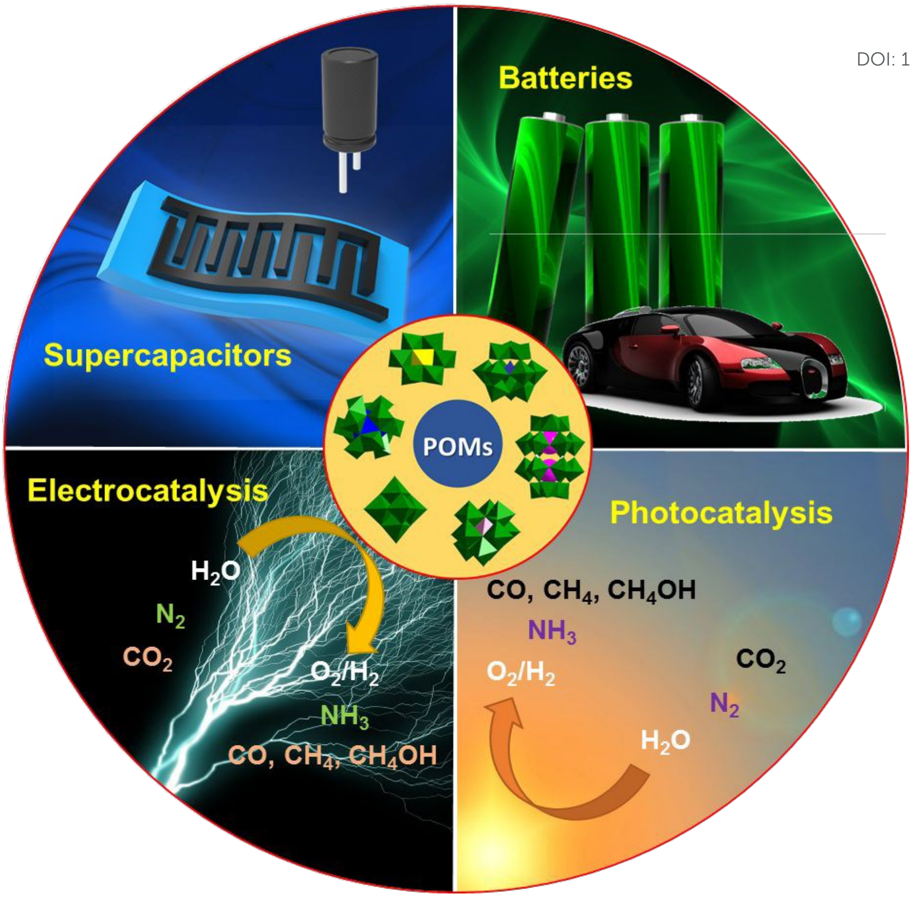

Figure 2. Polyoxometalates molecules and their range of energy related applications for a cleaner environment.

View Article Online
DOI: 10.1039/D0EE03407J

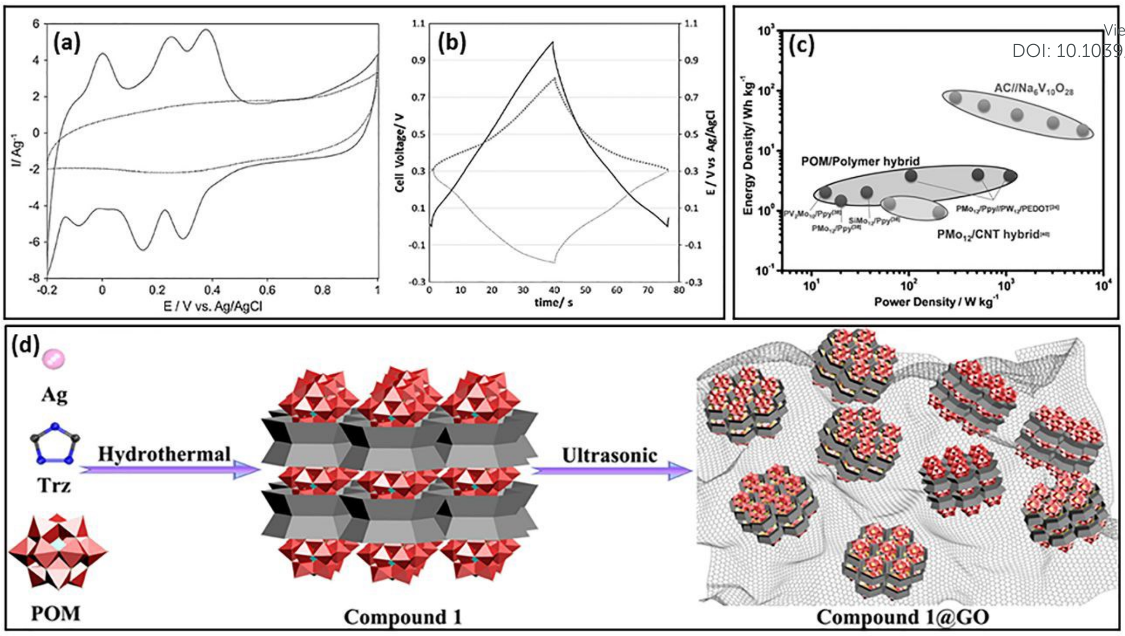

Figure 3. (a, b) Cyclic voltammetry and charge/discharge curves for AC and AC/PMo_{12} hybrid materials. Reprinted with the permission from Ref.[18], copyright 2012, Elsevier. (c) Ragone plot demonstrating the high energy density of vanadium based POMs. Reproduced with the permission from Ref. [36], copyright 2014 WILEY-VCH Verlag GmbH & Co. KGaA, Weinheim. (d) The metallacalixarenes are able to anchor POM clusters inside the pockets of the material. Reprinted with the permission from Ref. [36], copyright 2019, American Chemical Society.

View Article Online
DOI: 10.1039/D0EE03407J

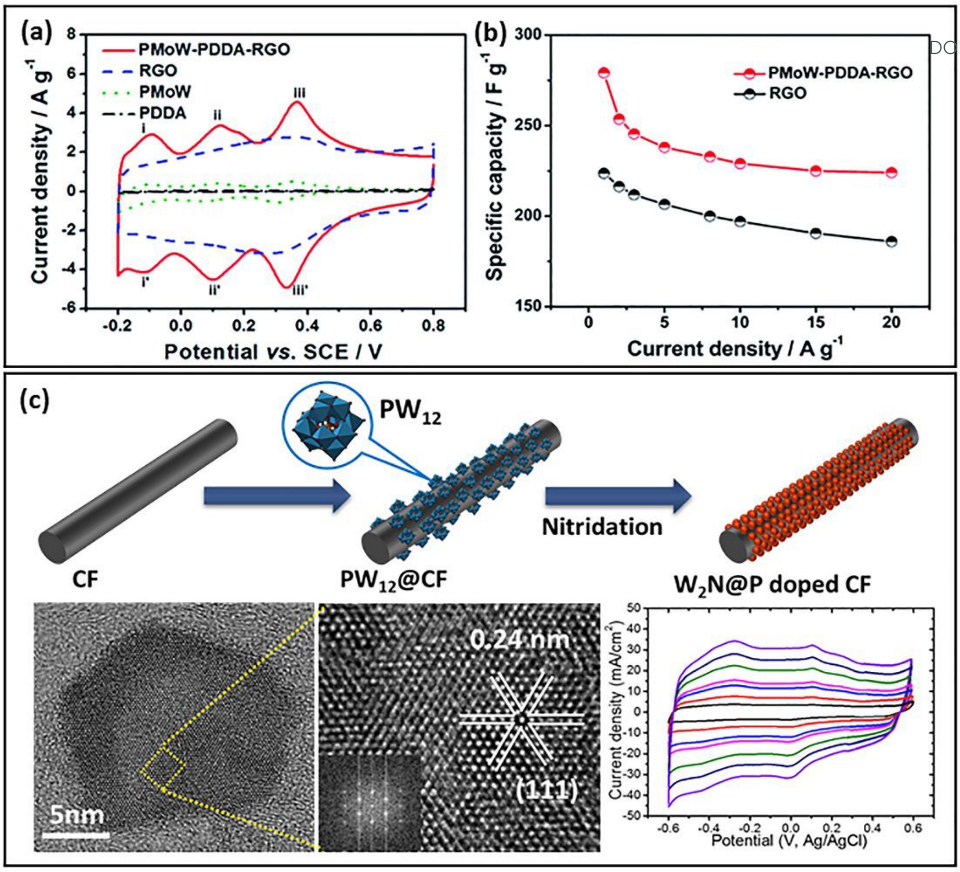

Figure 4. (a, b) CV curves of PDDA, PMoW, RGO and the PMoW-PDDA-RGO composite at 10 mV s^{-1}. (d) Rate performances of RGO and the PMoW-PDDA-RGO composite determined from discharge curves. Reprinted with the permission from Ref.[33], copyright 2016, The Royal Society of Chemistry. (c) Schematic illustration of synthesis of W$_2$N@P doped CF using PW$_{12}$ as precursor with corresponding TEM and electrochemical analysis. Reprinted with the permission from Ref. [62], Copyright 2018, Wiley-VCH Verlag GmbH & Co. KGaA, Weinheim.

View Article Online
DOI: 10.1039/D0EE03407J

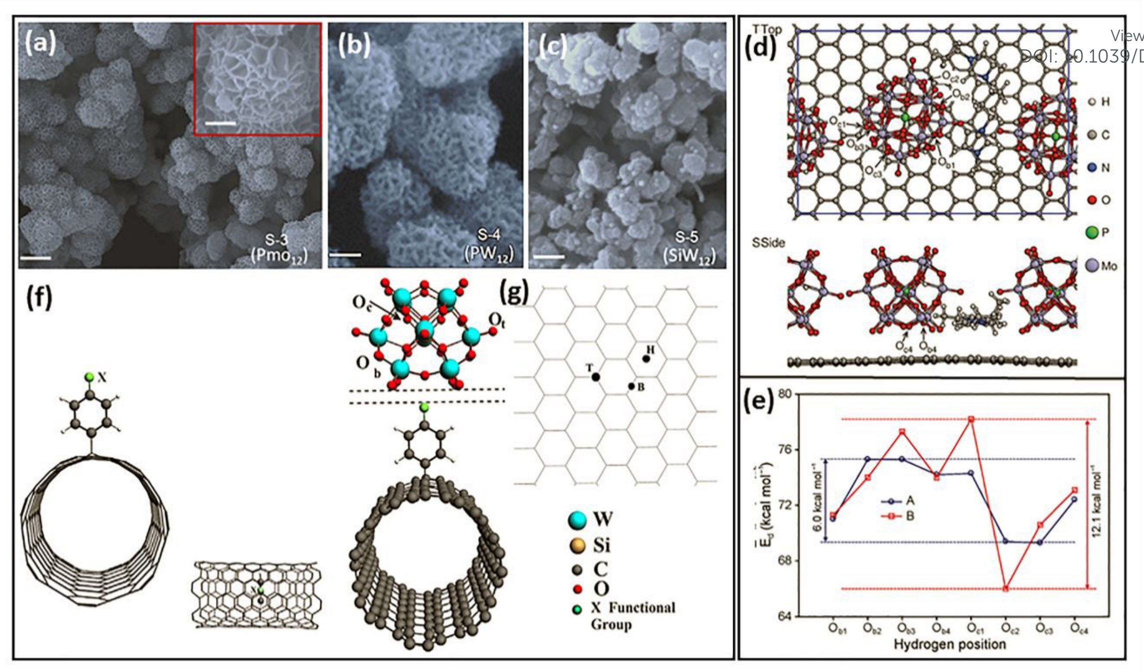

Figure 5 (a-c) SEM images of MnO_2 coated with different POMs such as PMo_{12}, PW_{12} and SiW_{12}, respectively. Reprinted with permission from [61], Copyright 2018, American Chemical Society. (d) POM/PIL/graphene structure, where two POMs and one IL dimer ($2[H_2PMo_{12}O_{40}][C_{14}H_{24}N_4]$), are included in a periodic unit cell. (e) The calculated adsorption energies compared with those obtained for the H adsorptions on the same O sites of an isolated POM ($H_2PMo_{12}O_{40}$) on graphene. Reprinted with the permission from Ref.[45], copyright 2014 WILEY-VCH Verlag GmbH & Co. KGaA, Weinheim. (f, g) Representation of anchoring of SiW_{12}@CNT where X denotes the functional groups -NH_2, -OH, -COH and –COOH, (f) Top(T), Bridge(B) and Hollow(H) points on the carbon network where the central axis of the SiW_{12} cluster is projected. Reprinted with permission from [64], Copyright 2018, Elsevier.

View Article Online
DOI: 10.1039/D0EE03407J

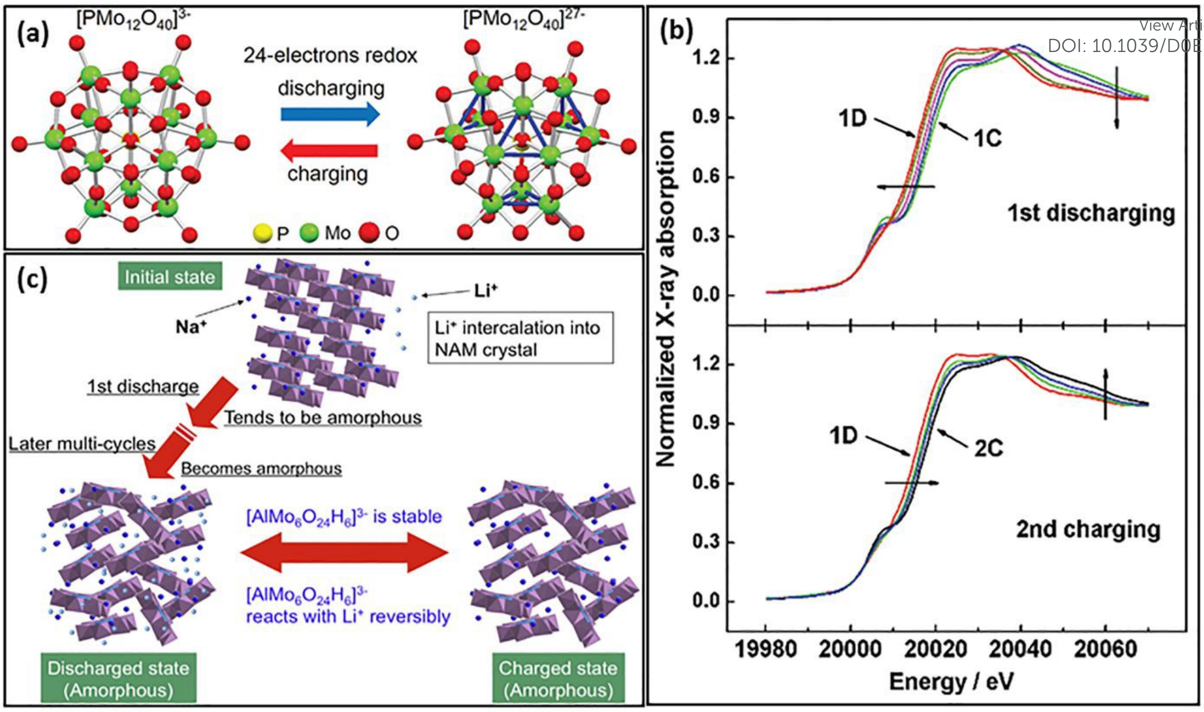

Figure 6 The ability of PMOs to discharge multiple electrons per molecule determines their outstanding ability to control redox processes in energy storage devices. (a) The reduction of all 12 Mo^{6+} to Mo^{4+} in $[PMO_{12}O_{40}]^{3-}$ to form $[PMO_{12}O_{40}]^{27-}$, (b) Mo K-edge XANES spectra for PMo_{12} MCBs in the first discharging and second charging. (c) Schematic illustration of reaction mechanism for NAM during the discharge-charge process. Reproduced with the permission from Ref. [90], Copyright 2012 American Chemical Society and Ref. [91], Copyright 2014, Elsevier.

View Article Online
DOI: 10.1039/D0EE03407J

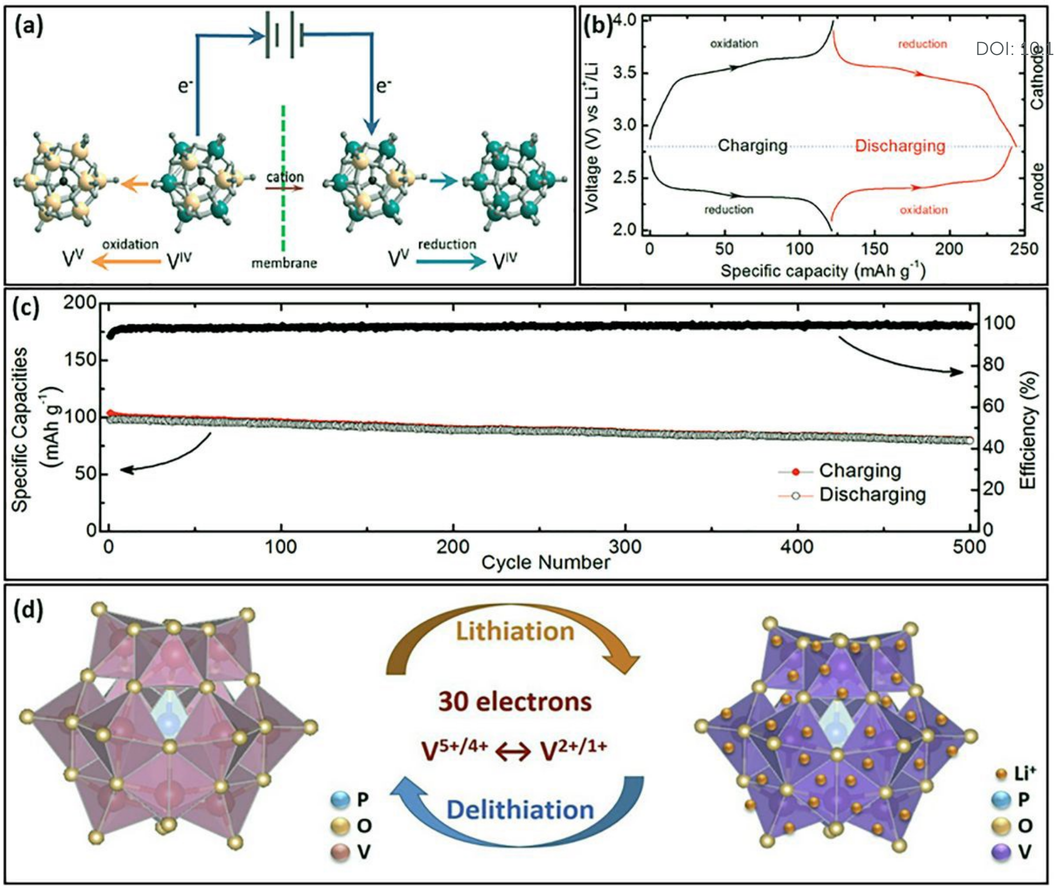

Figure 7 (a) Scheme showing the charging process of [$V_{15}O_{36}(CO_3)$]-based symmetrical LIBs (V^V centers; yellow, V^{IV} centers; teal), (b) Galvanostatic charge and discharge curves of $Li_7[V_{15}O_{36}(CO_3)]$ half-cell in within different voltage ranges at 100 mA.g^{-1} (c) Cyclic stability of symmetric $Li_7[V_{15}O_{36}(CO_3)]$ device (d) the concept of electron/ion sponge in NPV anode. Reprinted with permission from[95], Copyright 2017 Wiley-VCH Verlag GmbH & Co. KGaA, Weinheim and from ref. [96] , Copyright 2019 Elsevier.

View Article Online
DOI: 10.1039/D0EE03407J

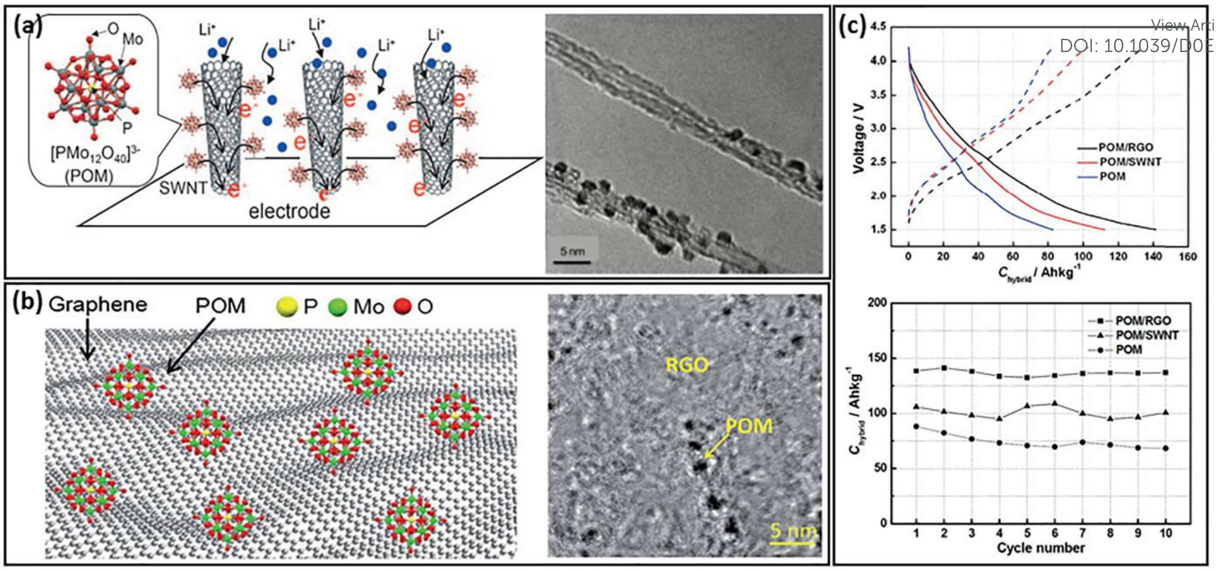

Figure 8 (a) A possible interaction of lithium with POM/SWNT hybrid and TEM image of the POM/SWNT hybrid (b) schematic demonstration and TEM image of $TBA_3[PMo_{12}O_{40}]$/rGO hybrid, (c) electrochemical performance of $TBA_3[PMo_{12}O_{40}]$/rGO in Li-ion battery. Reproduced with the permission from ref. [85], Copyright 2011, Wiley-VCH Verlag GmbH & Co. KGaA, Weinheim and from ref. [103], Copyright 2014, Royal Society of Chemistry.

View Article Online
DOI: 10.1039/D0EE03407J

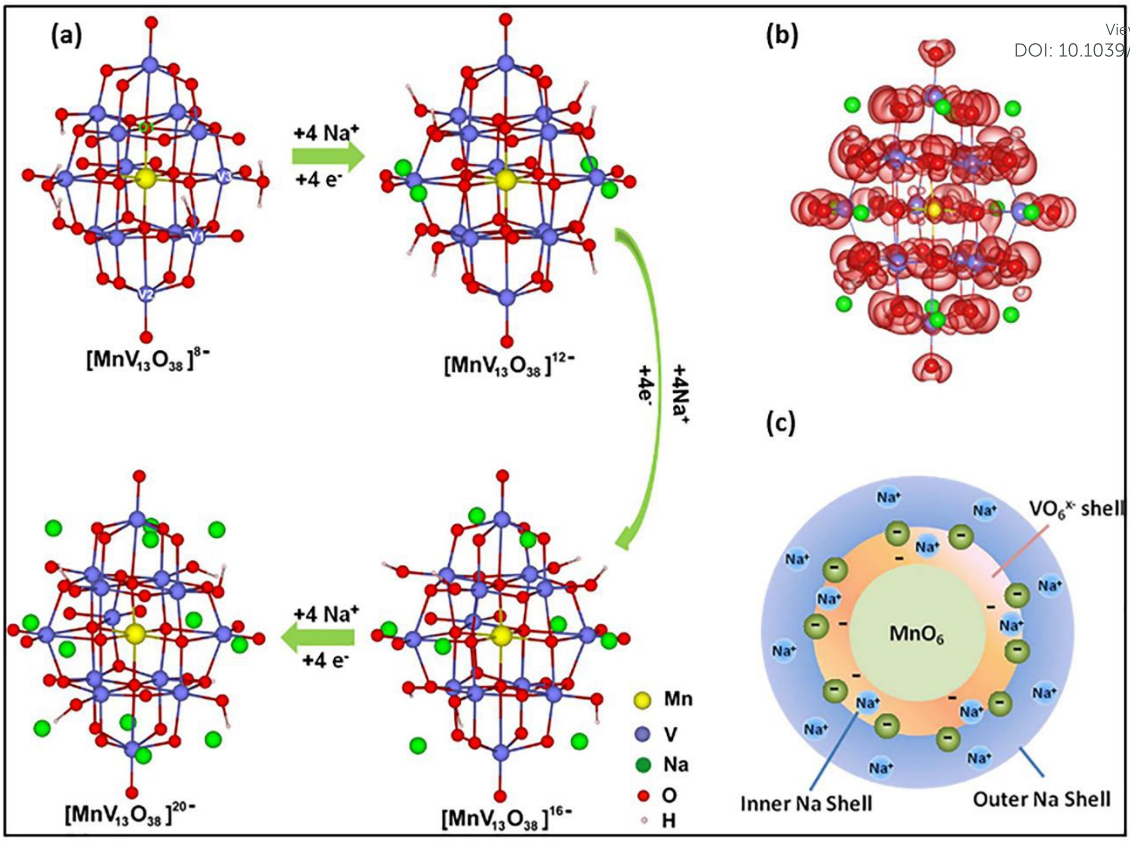

Figure 9 Charge storage mechanism in NMV cathode of (a) the molecular structure of $[MnV_{13}O_{38}]^{8-}$ and $[MnV_{13}O_{38}]^{20-}$ upon the insertion of Na^+, (b) charge redistribution of $[MnV_{13}O_{38}]^{20-}$ analyzed by the charge difference, and (c) electron/Na^+ ion sponge behavior. Reprinted with permission from [113], Copyright, 2017, American Chemical Society.

View Article Online
DOI: 10.1039/D0EE03407J

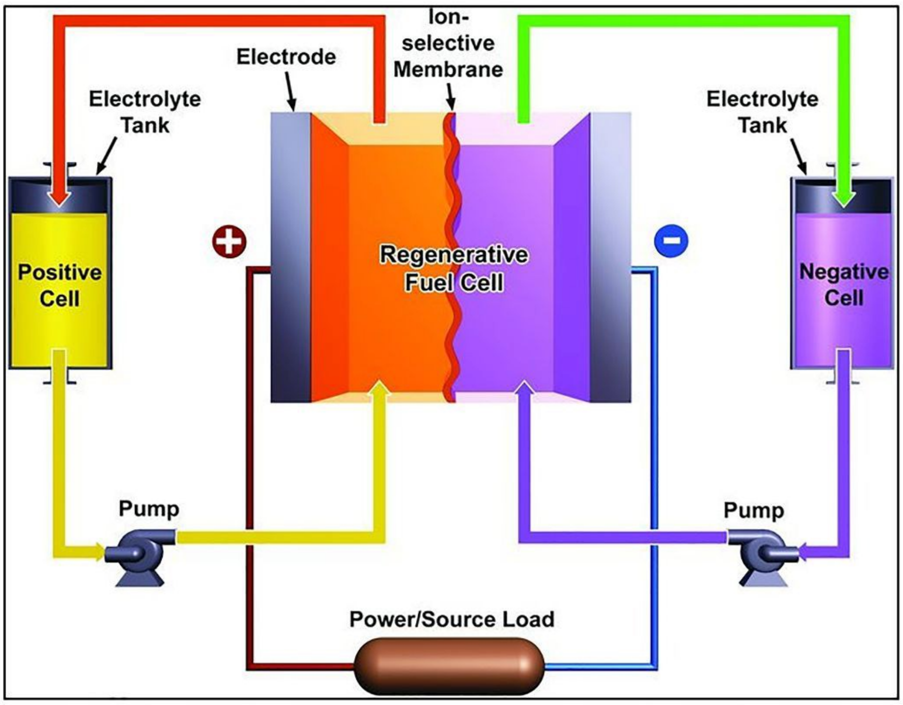

Figure 10 Schematic of the structure of a redox flow battery. Reprinted with permission from [128], Copyright 2011, Wiley-VCH Verlag GmbH & Co. KGaA, Weinheim.

View Article Online
DOI: 10.1039/D0EE03407J

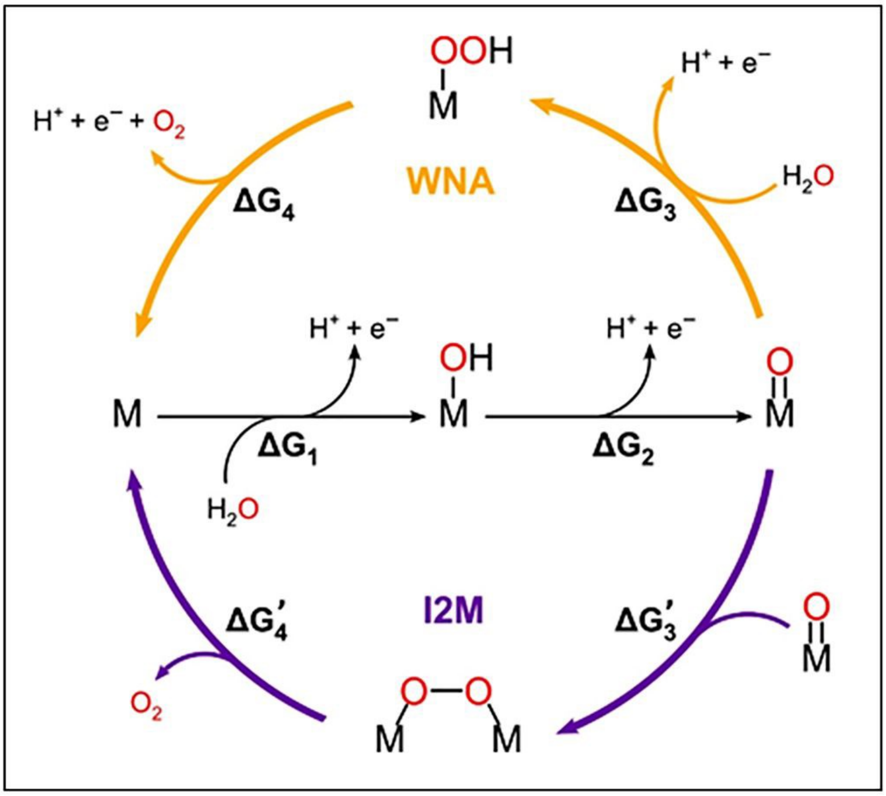

Figure 11 Catalytic cycles for the two primary reaction pathways proposed for the OER. Reproduced with permission from [138].

View Article Online
DOI: 10.1039/D0EE03407J

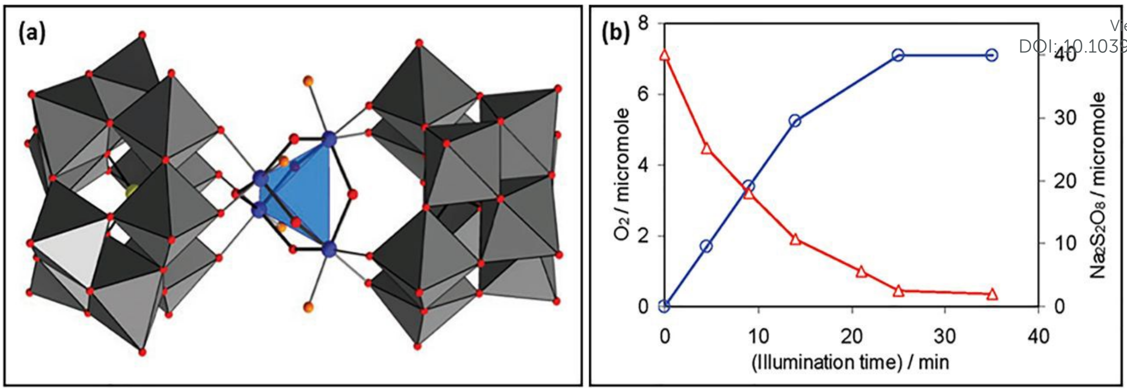

Figure 12 a) Structure of Ru_4Si_2, highlighting the central $[Ru_4(O)_4(OH)_2(H_2O)_4]^{6+}$core (ball-and-stick representation, Ru: blue, O: red, O(H_2): orange. Hydrogen atoms omitted for clarity). The POM fragments are shown as gray polyhedra. Reproduced with permission from [141], Copyright 2008, Wiley-VCH Verlag GmbH & Co. KGaA, Weinheim. b) Kinetics of O_2 formation (blue) and SA consumption (red) during light-induced catalytic water oxidation by Ru_4Si_2 5.0 µM using $Ru(bpy)_3^{2+}$ 1 mM as the PS and $S_2O_8^{2-}$5 mM as SA in sodium phosphate buffer 20 mM (initial pH 7.2). Reproduced with permission from [146]

View Article Online
DOI: 10.1039/D0EE03407J

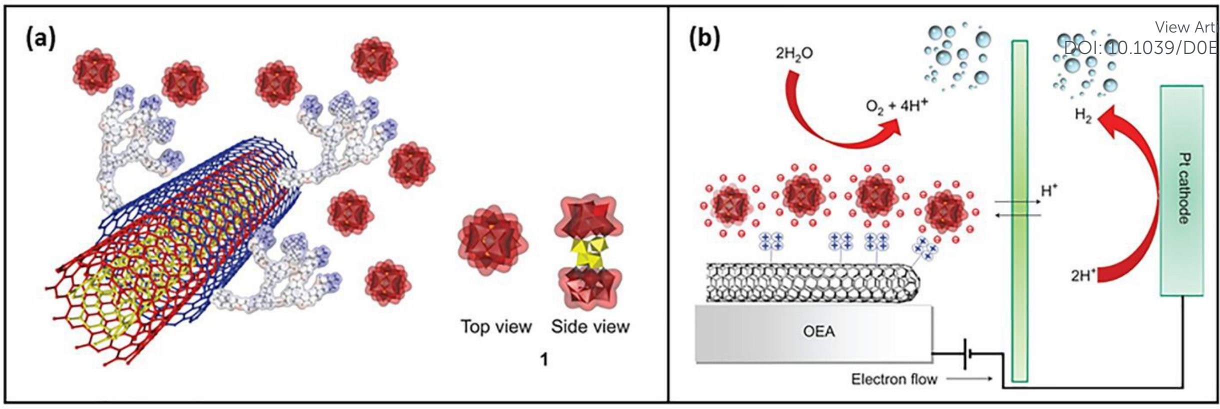

Figure 13 (a) Electrostatic capture of polyanion Ru_4Si_2 (red) by polycationic dendrons on the MWCNT surface (blue) and polyhedric structure showing the side and front view of Ru_4Si_2 with the $[Ru_4O_4]$ core in yellow. (b) General scheme for a water-slitting electrocatalytic cell with the integrated nanostructured O_2-evolving anode. Reprinted with permission from [159], Copyright 2010 Macmillan Publishers Limited.

View Article Online
DOI: 10.1039/D0EE03407J

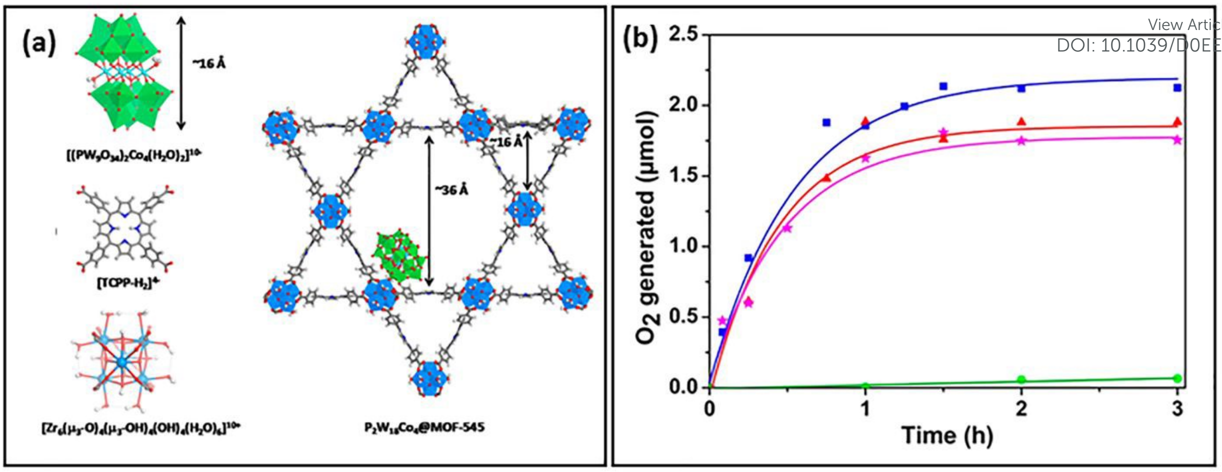

Figure 14 (a) Co_4P_2@MOF-545 components: Co_4P_2 ($[Co_4(H_2O)_2(PW_9O_{34})_2]^{10-}$); tetrakis(4-carboxyphenyl)porphyrin linker (TCCP-H_2); and Zr-based building blocks of the MOF ($[Zr_6(\mu_3\text{-}O)_4(\mu_3\text{-}OH)_4(OH)_2(H_2O)_6]^{10+}$). The position of Co_4P_2 in the MOF channel was obtained from computations. WO_6: green polyhedral, ZrO_8: blue polyhedra or spheres, Co: cyan spheres, O: red spheres, C: gray, H: light gray, N: dark blue. (b) Kinetics of photocatalytic O_2 production over 0.5 mg of Co_4P_2@MOF-545 (blue), Co_4P_2@MOF-545 recycled once (red), twice (pink), and a solution containing PS porphyrin linker 131 μM and Co_4P_2 13 μM (green). Reaction conditions: $S_2O_8^{2-}$ 5 mM as SA in borate buffer 80 mM solution, pH 8, visible light ($\lambda > 420$ nm, 280 W). (b) and (c) reprinted with permission from[183], Copyright 2018, American Chemical Society.

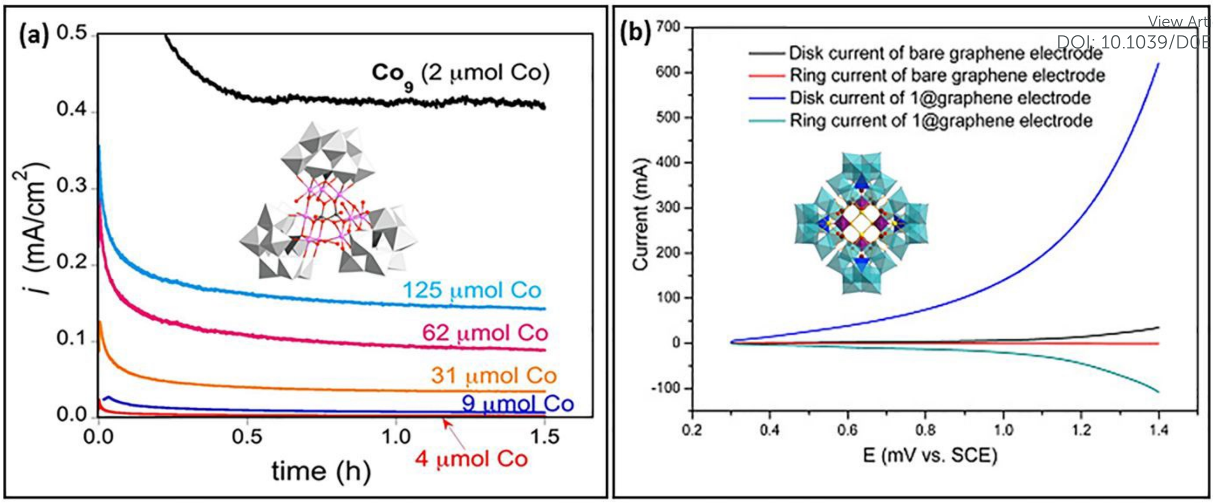

Figure 15 (a) Current density at +1.3 V (vs NHE) with a 44% Co_9-C electrode (black) and with Co_3O_4-C working electrodes at different Co contents (color lines). Labels indicate the total amount of Co in the blends. Reprinted with permission from [197]. Inset: Structure of Co_9, WO_6 (gray), PO_4 (black), Co (pink), P (black), O (red), reproduced with permission from [195]. (b) Linear sweep voltammetry (LSV) of Mn_{16}@graphene modified rotating ring-disk electrode in pH 7.5 phosphate buffer containing 1 M $NaNO_3$. The scan potential was from 0.3 V to 1.4 V at 50 mV/s on the disk electrode (blue line) and a constant potential of -0.35 V was applied to the ring electrode (green line). The bare graphene electrode was used as a reference under the same conditions (black and red lines). Inset: Structure of Mn_{16}, WO_6 (aqua), PO_4 (pink), SiO_4 (blue), Mn^{II} (yellow), Mn^{III} (brown), O (red). Reproduced with permission from [220], Copyright 2016, Royal Society of Chemistry.

View Article Online
DOI: 10.1039/D0EE03407J

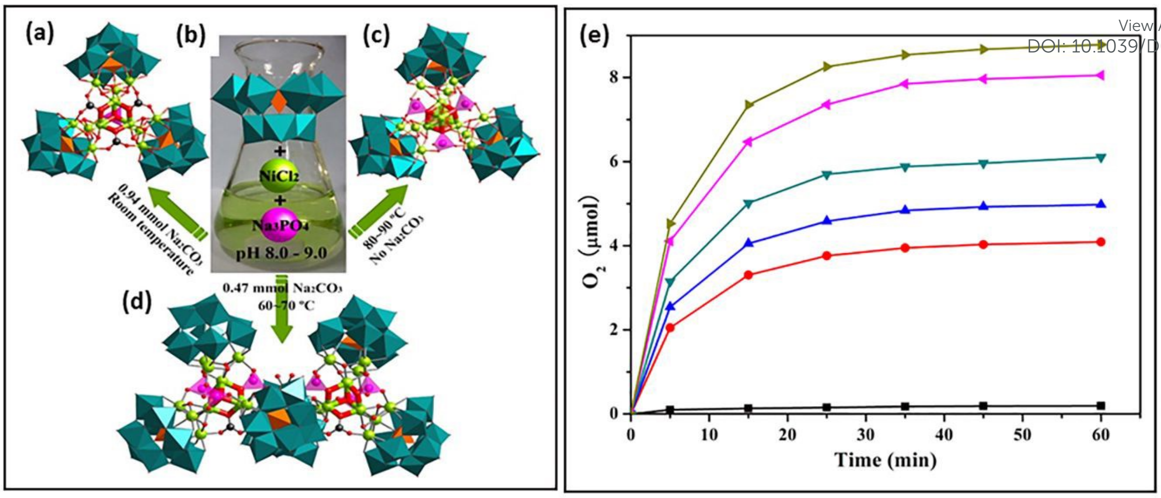

Figure 16. Ball-and-stick and polyhedral representation of the polyoxoanion structures of compounds (a) Ni_{12}, (c) Ni_{13} and (d) Ni_{25} ; (b) Schematic view of the synthetic procedures. WO_6, teal octahedra; PO_4, pink tetrahedra; SiO_4, orange tetrahedra; C, black sphere; O, red sphere; Ni, lime sphere. (e) Kinetics of O_2 evolution in the photocatalytic system at different concentrations of Ni_{25} 3. The symbols used to denote catalyst concentrations are 0 μM (black ■), 1 μM (red ●), 2 μM (royal blue ▲), 3 μM (teal blue ▼), 5 μM (magenta leftpointing triangle), and 10 μM (olive right-pointing triangle). Conditions: 300 W Xe lamp equipped with a long-pass filter (420 nm cutoff); 1.0 mM $[Ru(bpy)_3]Cl_2$, 5.0 mM Na2S2O8, sodium borate buffer pH 9.0 (80 mM); total reaction volume 20 mL; vigorous stirring (1.5 × 10^3 rpm). Reproduced with permission from [224], Copyright 2015, American Chemical Society.

View Article Online
DOI: 10.1039/D0EE03407J

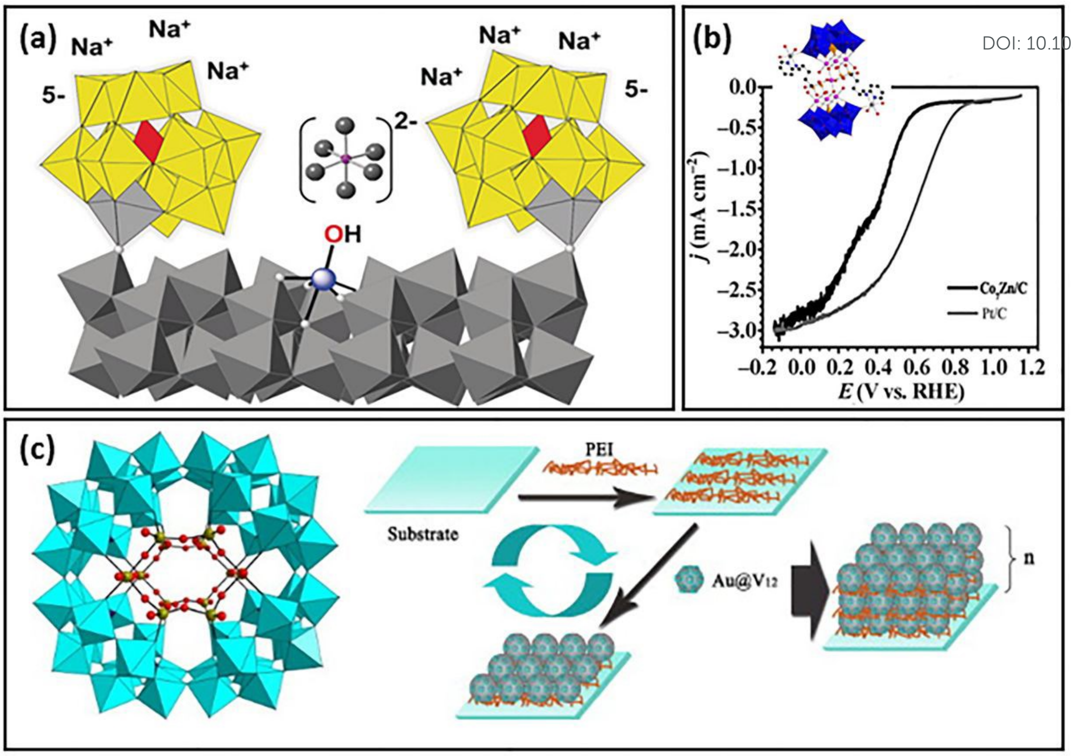

Figure 17 (a) Polyhedral presentation of the hematite surface with one Fe–OH reactive site highlighted in blue (two bound POM ligands and one $[H_3I^{VII}O_6\,]^{2-}$ SA drawn to scale). Reproduced with permission from [239], Copyright 2019, Wiley-VCH Verlag GmbH & Co. KGaA, Weinheim. (b) Linear sweep voltammograms of $Co_7(AlePyZn)_2/C$ and Pt/C in O_2-saturated 0.2 M $NaH_2PO_4/NaOH$ (pH 7.4) and a scan rate of 10 mV/s. Reproduced with permission from ref [253], Inset: Structure of the polyanionic unit in $Co_7(AlePyZn)_2$, WO_6(blue), PO_4 (orange), Co (pink), P (orange), C (black), N (blue), O (red), and Zn (grey). Redrawn from ref [242], Copyright 2015, Wiley-VCH Verlag GmbH & Co. KGaA, Weinheim. (c) Left: Structure of V_{12}, V (dark yellow), O (red), WO_6 (cyan), and PO_4 (blue). Right: Scheme of preparation of $(PEI/\ V_{12}@Au^0)_n$ LbL multilayer films on the ITO-coated electrodes (not scaled). . Reprinted with permission from [253], Copyright 2011, Elsevier.

View Article Online
DOI: 10.1039/D0EE03407J

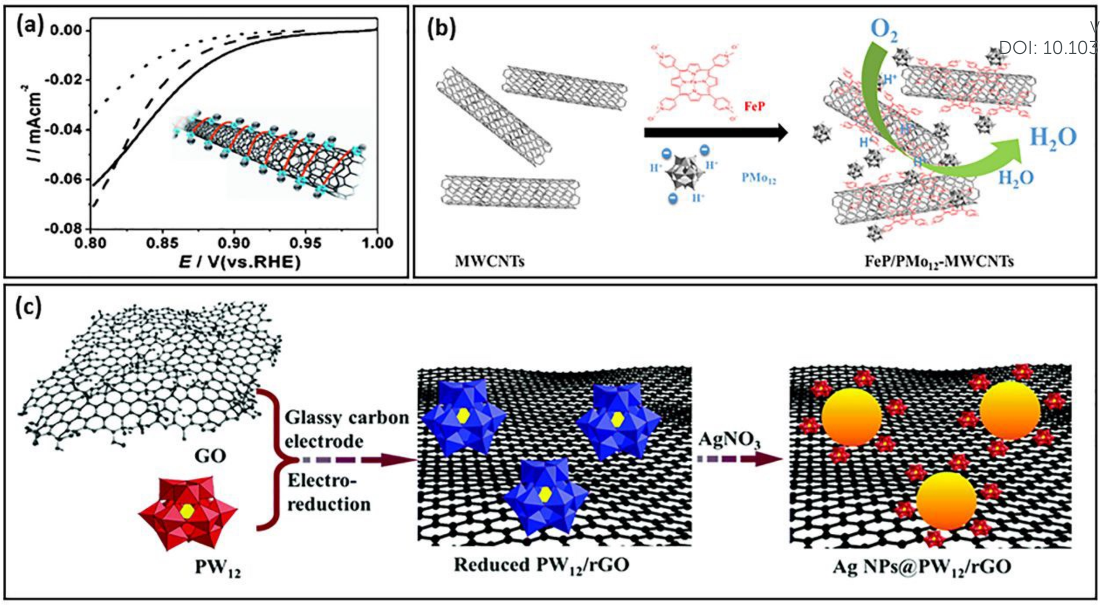

Figure 18 (a) Kinetic current density (I_k) obtained from rotating disk electrode experiments normalized by the electrochemical surface area of the catalysts. Dashed line: Pd/POM-PDDA-MWCNT; solid line: commercial Pt/C catalysts; and dotted line: acid-treated MWCNT-supported Pd. Reproduced with permission from[255]. Inset: Representation of Pd^0/POM-PDDA-MWCNT composite material. Reproduced with permission from [296], Copyright, 2015, Royal Society of Chemistry. (b) Schematic representation of the synthesis of FeP/PMo$_{12}$-MWCNTs electrocatalysts. For simplicity, the axial ligands of FeP were omitted. Reproduced with permission from [264], Copyright 2019, World Scientific Publishing Company (c) Electrochemical-reduction-assisted assembly procedure of the representative ternary Ag^{0}NPs@POM–rGO nanohybrids. Adapted with permission from [260], Copyright 2015, Royal Society of Chemistry. [264 255 254].

View Article Online
DOI: 10.1039/D0EE03407J

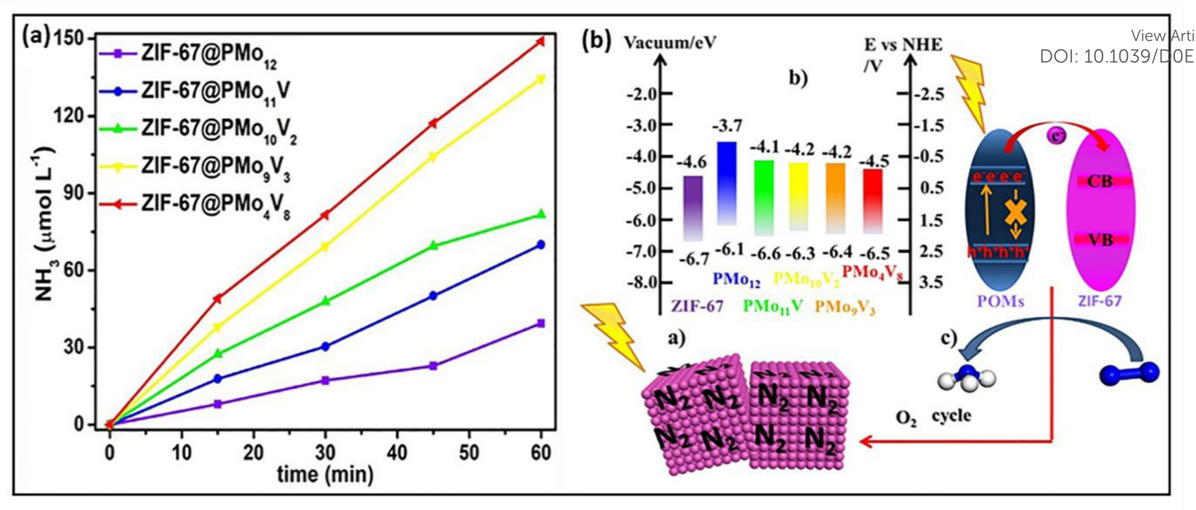

Figure 19 (a) NH_3 yield of various ZIF-67/POMs hybrids. (b) Energy levels and electron-transfer mechanism for ZIF-67 and POMs composite photocatalyst. [274]

View Article Online
DOI: 10.1039/D0EE03407J

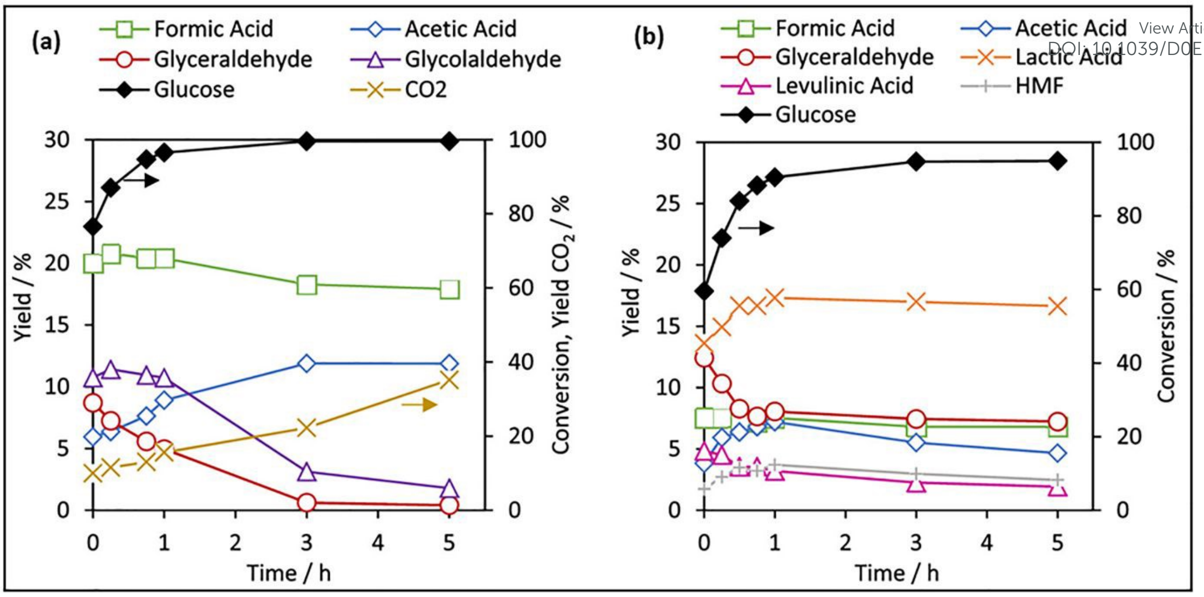

Figure 20 Time-dependent product distribution in the $K_5[V_3W_3O_{19}]$-catalyzed glucose conversion under (a) oxygen and (b) nitrogen atmospheres. Reaction conditions: 2 mmol of glucose, 0.167 mmol of $K_5[V_3W_3O_{19}]$, 10 g of water as solvent, 160 °C reaction temperature, 20 bar pressure, 1000 rpm stirrer speed, 0−5 h reaction time. With permission from [276]

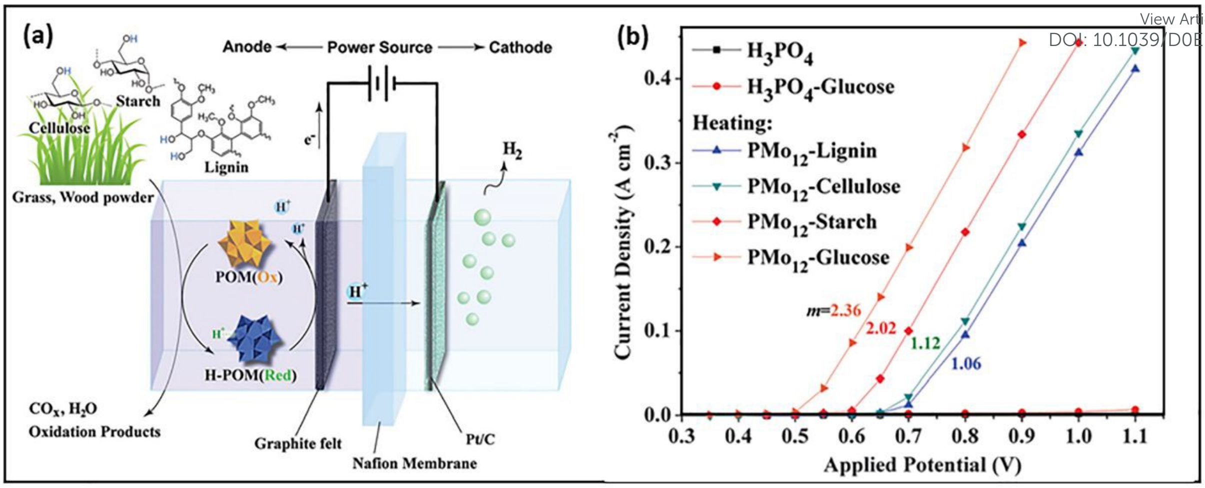

Figure 21 (a) Schematic illustration of the chemical-electric conversion (CEC) process. The anode is a simple graphite-felt electrode; the cathode is a gas-diffusion electrode loaded with the Pt black catalyst (4 mg cm^{-2}). (b) Polarization curves of PMo_{12} (0.3 mol l^{-1}) and biomass solution (fed with the anode side) preheated at 100 °C for 2 hours. The cathode side is pumped with 1 mol l^{-1} H_3PO_4 solution. Figure adapted from [277]

View Article Online
DOI: 10.1039/D0EE03407J

Table 1. POMs-based materials for lithium-ion batteries.

Materials	Electrode	Initial discharge capacity (mAh.g^{-1})	Current /Current density /Rate	Capacity retention (%)	Cycle number	Ref.
$K_3[PMo_{12}O_{40}]$ (KPM)	Cathode	>200	50 µA	37.5	50@100 µA	2,89
$TBA_3[PMo_{12}O_{40}]$	Cathode	260	1 mA	80.7	10	0
$Na_3[AlMo_6O_{24}H_6]$ (NAM)/KB	Cathode	437	0.04 C	91.2	50	91
$(NH_4)_6[NiMo_9O_{32}]$ (ANM) NPs/KB	Cathode	490	17 mA.g^{-1}	87.6	50	84
$(KH)_9[PV_{14}O_{42}]$ (KPV)	Cathode	370	100 µA	95	50	9
$K_7[NiV_{13}O_{38}]$ (KNiV)	Cathode	218.2	17 mA.g^{-1}	~91.6	24	81
$K_7[MnV_{13}O_{38}]$ (KMV)	Cathode	300	17 mA.g^{-1}	97.3	50	83
$(NH_4)_7[MnV_{13}O_{38}]$ (AMV)NPs	Cathode	234	0.5 C	100	100	3
$K_9[PV_{14}O_{42}]$/PP	Cathode	410	167 mA.g^{-1}	90	50	94
$Li_7[V_{15}O_{36}(CO_3)]$	Cathode	174	2 A.g^{-1}	85	100	2
$Na_7H_2[PV_{14}O_{42}]$ (NPV)	Anode	961	100 mA.g^{-1}	~57.2	150	6
$TBA_3[PMo_{12}O_{40}]$/SWNTs	Cathode	~320	1mA	~96	10	85
SWCNTs/ Py-SiW_{11}	Anode	1569.8	0.5 mA.cm^{-2}	37	100	98
CNTs/ SiW11-NH_2	Anode	1189	0.5 mA.cm^{-2}	54.6	100	6
PMO_{12}/PANI/MWNTs	Anode	1572	0.5 mA.cm^{-2}	63.6	100	99
SiW_{12}/rGO	Cathode	275	50 mA.g^{-1}	~99.5	20	00
$TBA_3[PMo_{12}O_{40}]$/rGO	Cathode	140	1 mA	~99	10	03
(EDA-rGO)/Anderson-type $Na_3[AlMo_6O_{24}H_6]$ (NAM)	Anode	1835	100 mA.g^{-1}	~54.4	100	101

View Article Online
DOI: 10.1039/D0EE03407J

3D rGO@PANI/PW_{12}	Cathode	235	200 mA.g^{-1}	87	50	104
Mo_6-SCN	Anode	1678	50 mA.g^{-1}	52.2	100	97
(Py-Anderson) -CNTs	Anode	1898.5	0.5 mA.cm^{-2}	35.1	100	98
Mn-Anderson /SWNT	Anode	3405.4	0.5 mA.cm^{-2}	~27.4	100	99
TBA-PMO11/CNT	Anode	3014.1	0.5 mA.cm^{-2}	28.2	100	00
POMOF-based on (Ni_6PW_9)SBUs	Anode	1421	1.25 C	~24.6	500	10
NNU-11	Anode	1322.3	50 mA.g^{-1}	56.7	200	05
NENU-507	Anode	1008	100 mA.g^{-1}	~63.5	100	07
POMOFs-based $PMo_{10}V_2$/rGO	Anode	2367.8	50 mA.g^{-1}	45.4	100	08
POMs-ILs@MOFs	Anode	1665.5	0.1 A.g^{-1}	~75	100	11
CuPW/SWNTs	Anode	1231.7	100 mA.g^{-1}	71.8	170	106
PMo_{12}@FeBTC	Anode	1542.6	100 mA.g^{-1}	42.6	50	01
Ni-POM	Anode	1325	100 mA.g^{-1}	53.5	50	02
Ag NPs/POMs	Anode	1760	0.1 C	-	-	03
POM-derived metal composites as anode for Li-ion batteries						
Hierarchical MoS_2	Anode	980	100 mA.g^{-1}	97.6	50	04
$MoO_2/Mo_2C/C$ spheres	Anode	1172	100 mA.g^{-1}	~68.2	100	05
3D porous MoP@C hybrid	Anode	1439	100 mA.g^{-1}	71.4	100	06
MoO_2@C nano-octahedrons	Anode	2936.8	100 mA.g^{-1}	~49	50	07
Mo_2C/N–C mesoporous hetero-NWs	Anode	1206.2	0.1 A.g^{-1}	78	50	08
3D hierarchically porous Mo_2C	Anode	1064.8	0.1 A.g^{-1}	87	100	09
MoS_2–C	Anode	1375	1 A.g^{-1}	90.9	200	10

MoO_2@MoS_2 Nanoarchitectures	Anode	1259	100 mA.g^{-1}	80.9	200	11
MoC–N–C	Anode	2479	100 mA.g^{-1}	50.2	300	12
2D layered mesoporous $MoS_{1.12}Se_{0.88}$/rGO	Anode	1238.4	100 mA.g^{-1}	67	150	13
Red $MoSe_2$ nanosheets	Anode	1706.88	1 A.g^{-1}	65.9	500	14

Mo_6-SCN =[(Bu4N)2[Mo6O18-N-Ph-(o-CH3)2-p-SCN], NNU-11= $[PMo_8{}^{v}Mo_4{}^{VI}O_{37}(OH)_3Zn_4][TPT]_5\cdot 2TPT\cdot 2H_2O$ (TPT=tris-(4-pyridyl)triazine), NENU-507= $(TBA)_3[PMo_8{}^{V}Mo_4{}^{VI}$ $O_{38}(OH)_2Zn_4(PBA)_2]\cdot H_2O$ (TBA = tetrabutylammonium ion, H PBA = 4-(pyridin-4-yl) benzoic acid), CuPW= $([Cu_{18}(trz)_{12}$ $Cl_3(H_2O)_2][PW_{12}O_{40}])$, BTC= benzene-1,3,5,-tricar- boxylate, Ni-POM = $[Ni_5(OH)_3(trzS)_3(en)(H_2O)(B\text{-}\alpha\text{-}PW_9O_{34})]$, Ag NPs/POMs =Silver nanoparticles/$[[Ni_{2.5}(Hpen)_4(PW_9O_{34})]\cdot 5H_2O]$

Table 2. Performance summary for POMs applied as ORR catalyst materials.

View Article Online
DOI: 10.1039/D0EE03407J

Catalyst	**Medium**	**On set for ORR**	**Remarks**	**Ref**
$Co_7(AlePyZn)_2$	Neutral and basic	0.710 V (Neutral) and 0.75 V (Basic) vs RHE.	4 electron pathways of reaction.	242
NH_4Co_7/TTF-F (i) Cu_6Ni_7/TTF-F (ii)	Neutral	0.838 V vs RHE (i) 0.854 V vs RHE (ii)	One-step reduction of oxygen	243
Co_4P_2@Carbon (SWCNT, Graphene flakes, N doped CNT)	Neutral	0.90V @N-CNT VS RHE	Out of various carbon support, the nitrogen doped CNT gives best performance.	244
$(PEI/P_5W_{30}–RGO)_{10}$ multilayers	Acidic	0.80V vs Ag/AgCl electrode.	POM played main role in electrocatalysis	245
$PMo_{11}V$@carbon suports (carbon-black, SWCNT and graphene)	Acidic	0.18 V vs. RHE $PMo_{11}V$@graphene (best)	Strong dependency on carbon support.	246
PW_{11}-3DOM	Acidic	0.69 V vs. NHE	H_2O_2 Formation rate 2.4 µmol h^{-1}	247

Table 3. Performance summary for co-catalyst POMs applied as ORR catalyst materials.

View Article Online
DOI: 10.1039/D0EE03407J

Catalyst	**Medium**	**Onset for ORR**	**Remarks**	**Ref**
Pd/PMo_{12}/rGO	Acidic	0.6 V vs. Ag/AgCl	High methanol tolerance	[256]
Ag/PW_{12}/CNT	Basic	-0.4 V vs. SHE	Instability of POM in alkaline medium	[257]
Ag/PW_{12}/rGO	Basic	0.15 V vs. RHE	30% Ag NPs loading has comparable performance as commercial Pt/C catalyst with 20% loading.	[258]
Ag^0NN@$H_7[\beta\text{-}PMo_4^{V}Mo_8^{VI}O_{40}]$–GNS	Basic	+0.924 V vs. RHE	Green, facile and large-scale synthesis of nanohybrids.	[259]
Ag NPs@PW_{12}/rGO	Basic	0.86V vs RHE	20% loading of Ag NPs gives best performance.	[260]
Ag@Pt/MWCNTs-PW_{12}	Acidic	0.85V vs. Ag/AgCl	25% of PW_{12}, 10% each loading of Ag and Pt NPs	[261]

View Article Online
DOI: 10.1039/D0EE03407J

Table 4. Summary of performance of Photocatalytic reduction of CO_2

Catalyst	**Final products yield**			**Remarks**	**Ref**
	CO				
$Ru^{III}(H_2O)SiW_{11}O_{39}]^{5-}$	50µmol			20-hour irradiation, Φ = 2%	315
$H_5PWV_2W_{10}O_{40}$	0.9 µmol			The POM act as co-catalyst to a dirhenium molecular catalyst	316
$Na_{10}[Co_4(H_2O)_2(PW_9O_{34})_2$ @g-C_3N_4	107 µmol g^{-1} h^{-1}			43 wt% Co_4 content. Convenient recovery, steady reuse.	317
Catalyst	**Product yield** µmol g^{-1} h^{-1}			**Remarks**	**Ref**
	CO	**CH_4**	**H_2**		
Au@$[PTi_2W_{10}O_{40}]^{7-}$	12.8	2.1	2.6	Keggin-type POM	318
Au@$[PW_{12}O_{40}]^{3-}$	0.5		0.15		
Au/$K_7(PTi_2W_{10}O_{40})$	2.1	0.35	0.29		
Catalyst	**Final product** µmol		**TON**	**Remarks**	**Ref**
	HCOOH				
$[Mo_{154}]_{1165}$	116.7		778	POM microions, HCHO was also obtained.	319
$[Mn_6P_3W_{24}]_{931}$	40.6		270	No HCHO is produced	
$[Mo_{132}]_{1064}$@rGO	205		1366	HCHO was also obtained.	
Catalyst	**Final product** nmol/g		**TON**	**Remarks**	**Ref**
	CO	**CH_4**			
NENU-605	52	170	135.9	TON of CH_4 alone 104.1. TON here is per 1000	320
NENU-606	68	402	282.2	TON of CH_4 alone 241.4. TON here is per 1000	
NENU-607	47	70	25.4	TON of CH_4 alone 15.2. TON here is per 1000	

(NENU-605)-$H[[Na2K_4Mn_4(PO_4)\ (H_2O)_4]_3[[Mo_6O_{12}(OH)_3(HPO_4)_3(PO_4)]_4[Mn_6(H_2O)_4]]$

(NENU-606)-$H[[Na_6CoMn_3(PO_4)(H_2O)_4]_3[[Mo_6O_{12}(OH)_3(HPO_4)_3(PO_4)]_4[Co_{1.5}Mn_{4.5}]]$

(NENU-607)-Mn $[Mo_6O_{12}(OH)_3(HPO_4)_3(PO_4)]_2$

View Article Online
DOI: 10.1039/D0EE03407J

Table 5 Summary of performance of different POM-MOF catalysts.

Catalyst	**E (V vs. SHE)**	**Onset Potential (V)**	**Current density (mA cm^{-2})**	**Charge transfer resistance (Ω)**	**TOF (h^{-1})**	**Ref.**
Co-PMOF	-0.8	-0.35	18.08	9.83	1656	291
Fe-PMOF	-0.7	-0.53	0.47	10.26	17.45	
Ni-PMOF	-0.8	-0.58	0.27	10.70	8.11	
Zn-PMOF	-0.9	-0.60	0.02	12.17	0.005	

Note: Charge transfer resistance was measured by electrochemical impedance spectroscopy (EIS).

View Article Online
DOI: 10.1039/D0EE03407J

Table 6. The performance of different electro-(photo)-catalyst towards NRR where STA- solar to ammonia.

Sample	NH_3 yield	STA efficiency (%)	TOF (h^{-1})	Faradaic efficiency (%, vs RHE)	Double layer Capacitance (mF cm^{-2})	Ref.
ZIF-67	22.2 µmol/L^{-1} h^{-1}	-	-	-	-	292
PMo_{12}	15.8 µmol/L^{-1} h^{-1}	-			-	
ZIF-67@ PMo_{12}	39.4 µmol/L^{-1} h^{-1}	0.008	24		-	292
$PMo_{11}V$	16 µmol/L^{-1} h^{-1}	-	-		-	
ZIF-67@ $PMo_{11}V$	70 µmol/L^{-1} h^{-1}	0.015	42		-	292
$PMo_{10}V_2$	23 µmol/L^{-1} h^{-1}	-	-		-	
ZIF-67@ $PMo_{10}V_2$	74.8 µmol/L^{-1} h^{-1}	0.016	42		-	
PMo_9V_3	27 µmol/L^{-1} h^{-1}	-	-		-	
ZIF-67@ PMo_9V_3	134.6 µmol/L^{-1} h^{-1}	0.029	76		-	
PMo_4V_8	28.4 µmol/L^{-1} h^{-1}	-	-		-	
ZIF-67@ PMo_4V_8	149 µmol/L^{-1} h^{-1}	0.032	94		-	
$Fe_{1.89}Mo_{4.11}O_7/FeS_2$@C	105.3 µg h^{-1} mgcat^{-1}	-	-	54.7% at -0.4 V	3.5	293
$FeMoO_4/FeS_2$@C	51 µg h^{-1} mgcat^{-1}	-	-	43.9% at -0.5 V	3.4	

View Article Online
DOI: 10.1039/D0EE03407J

Table 7. Yields of the main acids produced from the switchability experiments under oxygen and nitrogen atmosphere. Reaction conditions: 2 mmol of substrate, 0.5 mmol of (vanadium content) $H_6[PV_3Mo_9O_{40}]$ or $K_5[V_3W_3O_{19}]$ catalyst, 10 g of water as solvent, 160 °C reaction temperature, 20 bar oxygen pressure or nitrogen pressure, 1000 rpm stirrer speed, 1 h reaction time.

POM Type	Substrate	Environment	Yield	Ref.
$K_5[V_3W_3O_{19}]$	Glucose	Oxygen	YFA=20%	294
		Nitrogen	YLA=17%	
	Glyceraldehyde	Oxygen	YFA=16%	
		Nitrogen	YLA=17%	
$H_6[PV_3Mo_9O_{40}]$	Glucose	Oxygen	YFA=36%	
		Nitrogen	YLA=10%	
	Glyceraldehyde	Oxygen	YFA=42%	
		Nitrogen	YLA=40%	

View Article Online
DOI: 10.1039/D0EE03407J

Table 8. Literature overview of POM based materials for alcohol oxidation in direct alcohol fuel cells (DAFCs)

POM/composite	Electrolyte solution	Chronoamperometry			Ref.
		Voltage (V)	Intensity plateau/ (mA.mg^{-1})	Time (s)	
Pt/$(epy)_3PMo_{12}O_{40}$/rGO	0.5M CH_3OH + 0.5 M H_2SO_4 N_2-saturated	0.7	118	3600	279
Pt/$H_3PMo_{12}O_{40}$/rGO	0.5M CH_3OH + 0.5 M H_2SO_4 N_2-saturated	0.7	24	3600	279
$Pd_{0.5}Ni_{0.5}$/RGO/HPW$_{-3}$	0.5 M CH_3CH_2OH + 0.5 M KOH	n.a.	~180	4000	321
Pt/$H_3PMo_{12}O_{40}$/GO/ Nickel foam 1	1 M CH_3OH + 0.1 M KOH	0.7	~50	7200	322
Pt/$H_3PMo_{12}O_{40}$/GO/ Nickel foam 2	1 M CH_3OH + 0.1 M KOH	0.7	~0	7200	322
Pt/$H_3PMo_{12}O_{40}$/GO/ Nickel foam 3	1 M CH_3OH + 0.1 M KOH	0.7	~0	7200	322
Pt/$H_3PMo_{12}O_{40}$/GO/ Nickel foam 4	1 M CH_3OH + 0.1 M KOH	0.7	~0	7200	322
Au@Pd/PMo_{12}/RGO	1 M CH_3OH + 1 M NaOH	-0.3	~4 mA.cm^{-2}	1000	323
Activated PdNPs@PMo_{12}	1 M CH_3OH + 1.0 M NaOH	-0.2	~50	800	294
Non-Activated PdNPs@PMo_{12}	1 M CH_3OH + 1.0 M NaOH	-0.2	~0	800	294
$H_5PMo_{10}V_2O_{40}$ adsorbed on Pt	1 M CH_3OH + 0.5 M H_2SO_4		<0.1 mA.cm^{-2}	1800	324
$H_5PMo_{10}V_2O_{40}$	1 M CH_3OH + 0.5 M H_2SO_4	0.3	<0.006 mA	1800	324
$H_3PMo_{12}O_{40}$ Pt-Ru	1 M CH_3OH + 0.5 M H_2SO_4	0.3	<0.04 mA	200	289
$H_3PMo_{12}O_{40}$ Pt-Sn/C	1 M CH_3OH + 0.5 M H_2SO_4	0.3	<0.4 mA	200	289
$H_3PMo_{12}O_{40}$ Pt	1 M CH_3OH + 0.5 M H_2SO_4	0.4	<0.003 mA	200	289
$H_3PMo_{12}O_{40}$ Pt-Ru	1 M CH_3OH + 0.5 M H_2SO_4	0.4	<0.154 mA	200	289
$H_3PMo_{12}O_{40}$ Pt-Sn/C	1 M CH_3OH + 0.5 M H_2SO_4	0.4	~0.4 mA	200	289
$SiW_{12}O_{40}^{4-}$ on Pt/C catalyst	1 M CH_3OH + 0.5 M H_2SO_4	0.7	~1 A.mg^{-1}.cm^{-2}	1200	325
PtRu Nanoparticles with $H_3PMo_{12}O_{40}$	1 M CH_3OH + 0.5 M H_2SO_4	0.4	~0.8	3600	286
$H_3PMo_{12}O_{40}$ PtRu/PDDA/MWCNT	1 M CH_3OH + 0.5 M H_2SO_4	0.4	~1	3600	286
Pt black nanoparticles deposited onto TiO_2-supported Au-PMo_{12}	0.5 M CH_3OH + 0.5 M H_2SO_4	0.1	~0.2 mA.cm^{-2}	200	326
Pt black nanoparticles deposited onto TiO_2-supported Au-PMo_{12}	0.5 M CH_3OH + 0.5 M H_2SO_4	0.2	~0.65 mA.cm^{-2}	200	326

PtIr/PW_{12}/MWCNT	0.5 M CH_3OH + 0.5 M H_2SO_4	0.6	200	3000	326
PtRu/C PW_{12}	0.5 M CH_3OH + 0.5 M H_2SO_4	0.5	~3 mA.cm^{-2}	1500	292
PMo_{12}/Pt_4Pd1/MWCNT	0.5 M CH_3OH + 0.5 M H_2SO_4	0.6	200	3000	327
PdNPs@PMo_{12}-GCE	PBS (pH= 8.5) Phosphate buffer solution	-4.5	-0.5mA	300	290
PdNPs/ PWO_{12}/ILs/GCE	0.5 M CH_3OH + 0.1 M $HClO_4$	0.6	~0.045 mA.cm^{-2}	20000	328
Pt/PdNPs/PWO_{12}/ILs /GCE	0.5 M CH_3OH + 0.1 M $HClO_4$	0.6	~0.050 mA.cm^{-2}	20000	328
Pt-PdNPs/NaPWO/GQD	0.5 M CH_3OH + 0.1 M $HClO_4$	0.6	~0.045 mA.cm^{-2}	20000	329
PtNPs/NaPWO/GQD	0.5 M CH_3OH + 0.1 M $HClO_4$	0.6	~0.035 mA.cm^{-2}	20000	329